COMPUTER GENERATION OF KIKUCHI PROJECTIONS AND CHARACTERIZATION OF GENERAL BICRYSTALS

by

Ching Tsiun Young

Thesis submitted to the Graduate Faculty of the
Virginia Polytechnic Institute and State University
in partial fulfillment of the requirements for the degree of

DOCTOR OF PHILOSOPHY

in

Materials Engineering Science

Approved: _____

Chairman, Dr. Jack L. Lytton

_____ _____

Dr. C. R. Houska Dr. J. H. Steele Jr.

_____ _____

Dr. L. H. Slack Dr. A. L. Fricke

April, 1971

Blacksburg, Virginia

ACKNOWLEDGMENT

The author wishes to express his deep appreciation to Dr. Jack L. Lytton for his constant advice and guidance throughout this investigation. He is grateful to Dr. James H. Steele, Jr. for his valuable suggestions in the early phase of this research. He also would like to thank Mrs. Susan A. Carpenter and Mrs. Shirley Q. Phillips for typing the manuscript, and Mr. L. D. McDonald for his help in making the device for measurement of angles and distances. Finally, appreciation is extended to the National Science Foundation for the support of this work through its Grant Number GK-10972.

TABLE OF CONTENTS

LIST OF TABLES

LIST OF FIGURES

I. INTRODUCTION

In recent years, numerous investigations have been carried out on general bicrystals, such as two adjacent grains or subgrains, twins, or two neighboring phases, in order to study the orientation relationship between the two crystals and the detailed structure of the crystal boundary. In such studies, three parameters, i.e., misorientation angle, misorientation axis, and boundary normal, have been used to characterize the bicrystal.

The high resolving power of the transmission electron microscope enables the investigation of general bicrystals to be carried out on polycrystalline thin specimens. Crystal orientation can be approximated from electron diffraction spot patterns to within 5^{o} in general and to within 1^{o}-2^{o} in certain cases where spot intensity is taken into consideration. The orientation can be determined from Kikuchi patterns, if available, to within $\pm$ 0.1^{o}. Therefore, Kikuchi patterns can be used to relate accurately the orientation relationship between crystals, especially for the study of subgrains where misorientation angles are often less than 1^{o} - 2^{o}.

To determine the axis and angle of misorientation from Kikuchi patterns, standard stereographic procedures are usually employed. Identical low-index poles of the two crystals are plotted on a stereogram by referring to the observed Kikuchi patterns taken from each of the two crystals. The axis and angle of misorientation are then obtained by ordinary stereographic procedures[1]. The inaccuracy in plotting poles and manipulating of stereograms, even in using a stereogram of reasonably large size, e.g., 30 cm. in diameter, can easily lead to an error of more

than 1.0^{o} in the final results. Therefore, this method is not applicable to studies in which high accuracy is required, such as the determination of subgrain misorientations. The other parameter, boundary normal, is usually determined by trace analysis, in which large errors may be involved due to the uncertainty of foil thickness and foil inclination.

Lately, a mathematical analysis using matrix algebra for determining the bicrystal parameters has been developed [2] according to a standard procedure without any particular reference to a structural model for grain boundaries. The analysis was developed for Laue back-reflection studies, where the boundary plane could be aligned optically. Such an analysis, with the aid of computer techniques, can offer an accurate solution for bicrystal parameters.

The usual method of solving a Kikuchi pattern involves indexing of two or more pairs of non-parallel Kikuchi lines by trial and error procedures until the correct Kikuchi pole solutions are obtained. Beam axis is then determined from the three-pole solution of Heimendahl, et al. [3], or the two-pole solution of Otte, et al. [4].

To help solve Kikuchi patterns, composite Kikuchi maps, each covering a portion of the stereographic projection have been obtained for diamond cubic (Si), BCC (Fe-3%Si), and HCP (c/a=1.588) crystals [5,6]. Unknown patterns can then be more easily indexed by comparing them with the standard maps. However, such maps are difficult to prepare, and the contrast effects of the composite maps frequently causes confusion in the comparison of observed patterns with the maps.

Recently, complete stereographic Kikuchi maps have been generated for 500KV by computer plotting of BCC (α-Fe), FCC (Cu), diamond cubic (Si),

and HCP (Mg), as well as for Si at 20KV [7]. Such standard Kikuchi maps offer considerable advantages over the montage composite maps. However, only projections of [001] orientation for cubic crystals and projections of [0001] orientation for HCP crystal could be generated. As is the nature of standard stereographic projection, the distortion of the projection increases as the observed area is shifted away from the projection center. This causes the comparison to become more difficult for observed patterns with beam axes far away from the [001] or [0001] axes. This is especially true for non-cubic crystals.

The purposes of the present study were two-fold. The first was to develop a computer analysis which provided for an accurate determination of the three bicrystal parameters using Kikuchi patterns. The second was to develop computer programs which would provide for computer plotting of standard stereographic projections of Kikuchi patterns of any desired orientation, projection sphere radius, or wave length for FCC, BCC, diamond cubic, and HCP crystals.

II. LITERATURE REVIEW

In the following, some studies in the characterization of general bicrystals are reviewed. The origin of various types of line diffraction patterns and the applications of the patterns are mentioned.

A. Characterization of General Bicrystals

Recently a model for high angle grain boundaries based on an extension and combination of the coincidence lattice model of Kronberg and Wilson [8] and the dislocation model of Read and Shockley [9] has been developed. In this new model, two grains are related by particular misorientation angle and axis pairs which result in a high density coincidence site lattice, and the deviations from the particular orientation relationships are accommodated by the introduction of a dislocation subboundary. A general grain boundary takes a stepped structure so that more local areas of the boundary follow the most densely packed planes in the coincident lattice. Field-ion microscope observations of grain boundary structures have been reported to be well correlated with this grain boundary model [10,11,12].

Since the image in a field-ion microscope is a good approximation to a stereographic projection of the spherical tip of specimen, ordinary standard stereographic procedures are employed in the determination of misorientation angle-axis pairs, and the boundary normals are obtained either by assuming that the traces of boundaries on micrographs become small circles when plotted on a stereogram, or by analysis of a series of micrographs taken after a series of evaporations. The axis and angle of

misorientation can be determined with an accuracy of about $\pm 2^{o}$, but the plane of the boundary is not easy to determine accurately [12].

The fine structure of (001) twist boundaries in gold bicrystals with the boundary plane parallel to the thin foil has been systematically studied using transmission electron microscopy by Schober and Balluffi [13]. Orthogonal grids of grain boundary misfit screw dislocations were found in the vicinities of critical angles producing various high density coincidence site boundaries. The misfit angles were measured from electron diffraction spot patterns. The size of the diffraction spots were minimized by defocusing the illumination and using long exposure time. The total possible error was estimated to 0.75^{o} in the twist angle measurement.

The effect of grain boundary structure and misorientation on grain boundary precipitation in Al-Zn-Mg and Al-Mg alloys has been investigated by Unwin and Nicholson [14] using transmission electron microscopy. Kikuchi patterns and ordinary stereographic procedures were employed to determine the misorientation angle and axis. Boundary normals were determined by tilting the specimen so that the boundary planes become parallel to the electron beam. It was shown that electron microscopy could be used to study the bicrystal parameters even though the atomic configuration at the boundary could not be seen with this technique.

A quantitative method for the study of orientation relationships between subgrains by dark-field transmission electron microscopy has been demonstrated by Koo [15]. The tilting stage was calibrated to a precision of 0.05^{o} by use of Kikuchi patterns taken from an aluminum foil. The specimen was tilted in dark field with a selected $\bar{g}$ vector,

and the constrast reversal which occurred between neighboring subgrains was used as a criterion to deduce the misorientation angles and the type of boundaries. The precision of this tilting method was limited by experimental errors and was reported to be $\pm$ 0.1 - 0.2^{o} depending upon experimental conditions and the order of reflection used.

Lange [2] has developed a mathematical analysis using matrix algebra for the determination of the five variables for characterizing a bicrystal according to a standard manner without reference to a grain boundary structure model. Among these five variables, two are associated with misorientation axis, one is related to misfit angle, and the other two define the boundary normal. The analysis was developed for Laue back-reflection studies of a general bicrystal, where the boundary normal could be aligned optically.

B. Line Diffraction Patterns and Their Application

Line diffraction patterns of transmission or back-reflection type have been observed in studies of single crystal diffraction when a divergent or convergent incident beam is used, or when divergent radiation is generated inside the crystal. Examples are Kikuchi patterns taken from transmission electron microscopy, Coates patterns obtained from scanning electron microscopy, and Kossel patterns or pseudo-Kossel patterns observed in x-ray photographic studies.

In transmission electron microscopy (TEM), inelastic scattering of a nearly parallel incident beam generates a divergent electron beam inside the crystal. Subsequent diffraction of this beam from crystal planes gives rise to Kikuchi patterns [16], which basically consist of pairs of

black and white Kikuchi lines forming a pattern related to the crystal structure and electron wave length. Similar patterns which essentially consist of bands, and have the same geometrical construction to that of Kikuchi patterns have been obtained when a convergent incident electron beam is applied [17]. These patterns, sometimes referred to as channeling patterns, have been observed to superimpose on the bright field electron micrographs and expand in scale together with the bright field images as magnification is increased.

In scanning electron microscopy (SEM), line patterns similar to the channeling patterns in TEM have been observed to superimpose upon the normal topographical electron images and these also expand in scale as magnification is increased. These patterns have been called channeling patterns or Coates patterns since they were first observed by Coates [18]. Coates patterns are built up point by point from back scattered electrons or specimen-current signals as the nearly parallel incident beam scans over the surface of specimen, and the patterns are superimposed on the topographical images. Coates patterns alone can be obtained by having a stationary beam and by rocking the specimen in two orthogonal directions in synchronism with the raster of the display tube [18]. They can also be generated from either the double deflection rocking beam technique or the deflection focusing beam technique described by Van Essen et al. [19] Transmission channeling patterns have been obtained from thin foils using high-voltage SEM [20].

In x-ray studies, transmission or back-reflection Kossel patterns have been obtained either by using flourescent radiation originated inside the crystal or using radiation generated from a fine electron beam target

placed in front of the crystal to produce a divergent x-ray beam. Kossel patterns obtained by applying the external target as the x-ray source are frequently referred to pseudo-Kossel patterns. Standard Laue x-ray techniques and capillary x-ray tubes have been used to obtain back-reflected and transmitted Kossel patterns. More recently, however, the electron probe microanalyzer with attached Kossel camera has dominantly been employed to obtain transmission Kossel patterns.

Kikuchi patterns, Coates patterns, and Kossel patterns are all sensitive with respect to crystal orientation and lattice parameters. The application of Kikuchi patterns in TEM for exact crystal orientation determination, phase identification, Burgers vector determination, as well as other crystallographic analyses have been described in many publications [3,21,22]. Composite Kikuchi maps of [001], [011], and [111] orientations for diamond cubic (Si) [5], the [001] orientation for BCC (Fe-3%Si), and the [0001] orientation for HCP (Ag_2Al) [6], each covering a portion of the stereographic projection, have been obtained to assist in identification of unknown diffraction patterns. Recently, complete [001] and [0001] stereographic projections have been generated by computer plotting for diamond cubic (Si), BCC (α-Fe), FCC (Cu), and HCP (Mg) at 500KV, as well as diamond cubic (Si) at 20KV [7].

Kossel techniques have been used in precision lattice parameter measurement [23,24,25], strain measurement [26], precision orientation determination [27], and lattice defect and crystal deformation studies [28]. Lonsdale [29] first demonstrated a convenient way to index Kossel patterns for cubic systems by using a stereographic projection method. In this technique, a standard [001] stereographic projection of Kossel patterns

was manually constructed and indexed. Observed patterns were compared with the projection and the indices of each Kossel line could then be easily determined. A detailed description of the mathematical operations for obtaining information from Kossel patterns and generating computer plots of stereographic projections of Kossel patterns have been given by Morris[23]. Computer generation of Kossel projections has also been described by Frazer and Arrhenius [30], and Bomback and Thomas [7].

Generation of Coates patterns provides the unique method for obtaining crystallographic information from bulk crystals in SEM. Computer simulation of Coates patterns has been performed by Bomback and Thomas [7], but only for the [001] orientation.

Computer generation of some other types of patterns can also be found in the literature, e.g., the computer simulation of electron diffraction patterns for two-phase cubic crystals [31] and the computer simulation of field-ion images for hexagonal structure and superlattices [32].

III. ANALYTICAL PROCEDURES

In the following sections, the matrix operations employed in the present study are briefly described. The analytical procedures for the determination of misorientation and rotation matrices, together with several different methods used to obtain boundary normals are given. Finally, the computer generation of various line diffraction projections, mainly the Kikuchi projection, are described.

A. Matrix Formulation

Matrix operations related to the problems of rigid body rotation can be found in many text books. A comprehensive introduction of the application of matrix algebra to crystallographic transformations has been given by Wayman [33]. Unfortunately, there is no uniformity in the literature about the formulation of matrices and different conventions are employed. Therefore, it is necessary to present some of the matrix formulations here, based on a convention which is found to be convenient for the present study.

1. Coordinate Transformation and Rotation Matrix

In crystallographic studies where crystal rotation is involved, it is often required to define a vector based on different coordinate systems, or bases. It is also frequently desired to define a vector before and after rotation based on a fixed coordinate system. In this respect, a matrix which relates the bases in question is usually used to perform the desired transformations.

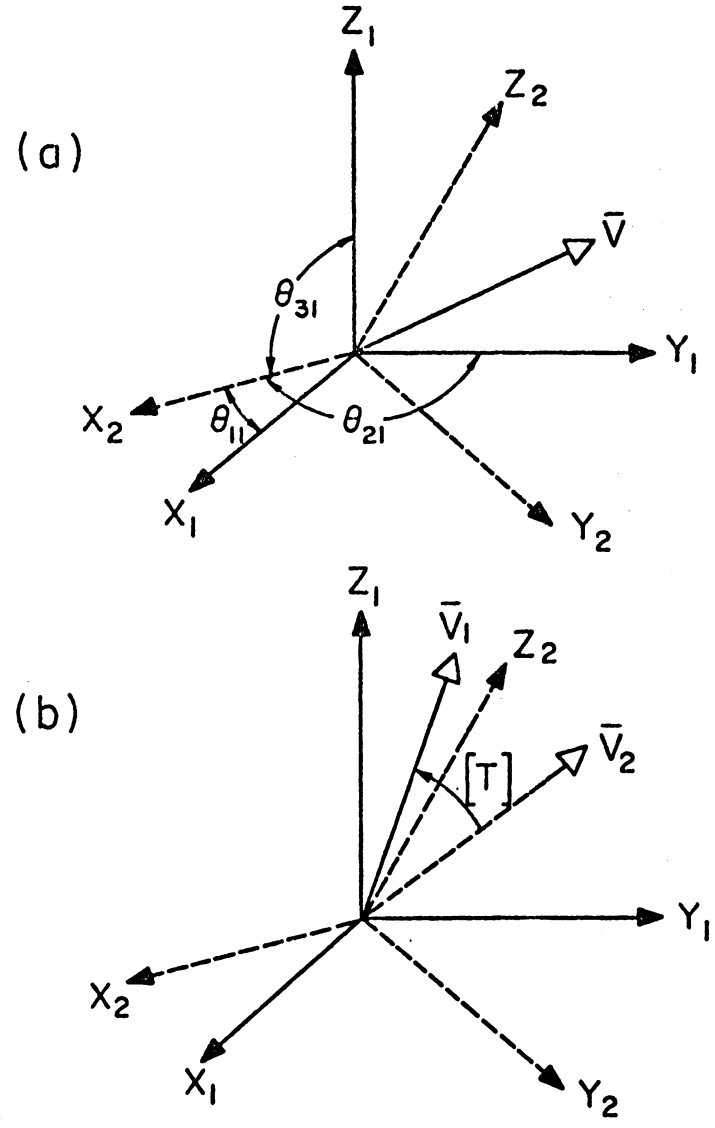

Fig. 1. (a) Rotation of coordinate basis with respect to a fixed vector.
(b) Rotation of vector with respect to a fixed coordinate basis.

Figure 1(a) shows two orthonormal bases, basis 1 and basis 2, and a vector $\bar{V}$ fixed in space.* For convenience, B1 and B2 will be used to designate basis 1 and basis 2, respectively. Figure 1(b) shows the same two bases and two vectors, $\bar{V}_1$ and $\bar{V}_2$ both having the same coordinates when referred to B1 and B2, respectively. The orientation relationship between the two bases can be represented by a 3x3 orthogonal matrix [T] consisting of an array of direction cosines, i.e.,

$$[T] = \begin{bmatrix} \cos\theta_{11} & \cos\theta_{12} & \cos\theta_{13} \\ \cos\theta_{21} & \cos\theta_{22} & \cos\theta_{23} \\ \cos\theta_{31} & \cos\theta_{32} & \cos\theta_{33} \end{bmatrix} \tag{1}$$

where θ_{ij} is the angle between the ith axis of B1 and the jth axis of B2. Here, X, Y, and Z axes are taken as the 1st, 2nd, and 3rd axes, respectively. It is seen that the jth column of [T] defines the coordinates of the jth axis in B2 with respect to B1. If the vectors $\bar{V}$, $\bar{V}_1$, and $\bar{V}_2$ are labeled as column matrices $[\bar{V}]_{Bi}$, $[\bar{V}_1]_{Bi}$, and $[\bar{V}_2]_{Bi}$ when all are referred to Bi, i=1,2, the desired transformations between the two bases, given in matrix notations, are

$$[\bar{V}]_{B1} = [T]\,[\bar{V}]_{B2} \tag{2}$$

$$[\bar{V}_2]_{Bi} = [T]\,[\bar{V}_1]_{Bi} \quad , \; i=1,2 \tag{3}$$

$$[\bar{V}]_{B2} = [T]^{-1}\,[\bar{V}]_{B1} \tag{4}$$

$$[\bar{V}_1]_{Bi} = [T]^{-1}\,[\bar{V}_2]_{Bi} \quad , \; i=1,2 \tag{5}$$

where $[T]^{-1}$ is the inverse matrix of [T]. For an orthogonal matrix such as [T], the inverse matrix of [T] is simply the transpose matrix of [T].

*Hereafter, all vectors will be denoted using a bar over the vector.

It is important at this stage to note the physical meanings imposed by [T]. In equation (2), [T] transfers a fixed vector from B2 to B1. Therefore, from a fixed-vector point of view, [T] can be used as a rotation matrix representing the rotation of B2 to B1. On the other hand, in equation (3), [T] transfers a vector from $\bar{V}_1$ to $\bar{V}_2$ based on either B1 or B2. Consequently, from a fixed-basis point of view, [T] is a rotation matrix which rotates $\bar{V}_1$ to $\bar{V}_2$ based on fixed B1 or fixed B2. The short notations representing these transformations and rotations performed by [T] are given in the following:

[T] = a matrix which defines B2/B1

[T] = a matrix which transfers $\bar{V}$/(B2→B1)

[T] = a matrix which rotates B2→B1

[T] = a matrix which rotates ($\bar{V}1 \rightarrow \bar{V}2$)/B1 or B2.

The inverse matrix of [T], $[T]^{-1}$, performs the operations inverse to those performed by [T]. It should be mentioned that in the present study, Bi/Bj always means that Bi is defined "column-wise" with respect to Bj.

An important example is considered here. Let the coordinate axes of B1 be [100], [010], and [001], and those of B2 be parallel to $[h_1k_1\ell_1]_{B1}$, $[h_2k_2\ell_2]_{B1}$, and $[h_3k_3\ell_3]_{B1}$. The matrix which rotates B1 to B2, or transfers a fixed vector from B1 to B2 is $[T]^{-1}$, and is given by

$$[T]^{-1} = \begin{bmatrix} h_1/\sqrt{S_1} & k_1/\sqrt{S_1} & \ell_1/\sqrt{S_1} \\ h_2/\sqrt{S_2} & k_2/\sqrt{S_2} & \ell_2/\sqrt{S_2} \\ h_3/\sqrt{S_3} & k_3/\sqrt{S_3} & \ell_3/\sqrt{S_3} \end{bmatrix} \tag{6}$$

where $S_i = h_i^2 + k_i^2 + \ell_i^2$. This matrix will be used in the characterization of bicrystals and plotting of line diffraction projections.

In a study which involves crystal rotation, it is also often necessary to perform transformation or rotation of a vector based on different coordinate systems. Let the two vectors $\bar{V}_1$ and $\bar{V}_2$ in Figure 1(b) be two arbitrary vectors labeled by $\bar{p}$ and $\bar{q}$, respectively. A matrix [T] which defines B2 with respect to B1 will operate the following transformations:

$$[\bar{p}]_{B1} = [T][\bar{p}]_{B2} \tag{7}$$

$$[\bar{q}]_{B1} = [T][\bar{q}]_{B2}. \tag{8}$$

Another matrix [R] can be written to perform the rotation of $\bar{p}$ to $\bar{q}$ based on B1, i.e.,

$$[\bar{q}]_{B1} = [R][\bar{p}]_{B1}. \tag{9}$$

By substituting equation (7) and (8) into (9), one gets

$$[T][\bar{q}]_{B2} = [R][T][\bar{p}]_{B2}$$

$$[\bar{q}]_{B2} = [T]^{-1}[R][T][\bar{p}]_{B2} = [S][\bar{p}]_{B2} \tag{10}$$

where $[S] = [T]^{-1}[R][T]$. By comparing equation (9) and (10), it is seen that [R] performs the rotation of $\bar{p}$ to $\bar{q}$ based on B1, while [S] performs the similar rotation based on B2. [S] is then called the similarity rotation matrix of [R]. Similarity rotation matrices will be used later in the determination of boundary normals.

2. Rotation Matrix Expressed in Terms of Eulerian Angles

Although a rotation matrix has nine elements, it has only three independent variables, for example, three Eulerian angles. The rotation of a coordinate system can be performed by means of three successive rotations, each about any of the three coordinate axes in a specific sequence. The Eulerian angles are then defined as the three successive angles of rotation. Each of the three rotations can be described by a rotation matrix expressed in terms of the corresponding Eulerian angle. The resultant rotation is then defined by the product of the three matrices multiplying in proper sequence.

Figure 2(a) shows a sequence of rotation which results in a rotation of coordinate system from basis 1 to basis 4. The sequence of rotation and the corresponding rotation matrices are

(1) B1 → B2 about X_1 by angle α, represented by [A],

(2) B2 → B3 about Y_2 by angle β, represented by [B],

(3) B3 → B4 about Z_3 by angle γ, represented by [C],

where [A], [B], and [C] are rotation matrices, each specifying a rotation about a "new" axis after previous rotation. The resultant rotation matrix [R] is calculated by

$$[R] = [C][B][A] \tag{11}$$

where, according to equation (4),

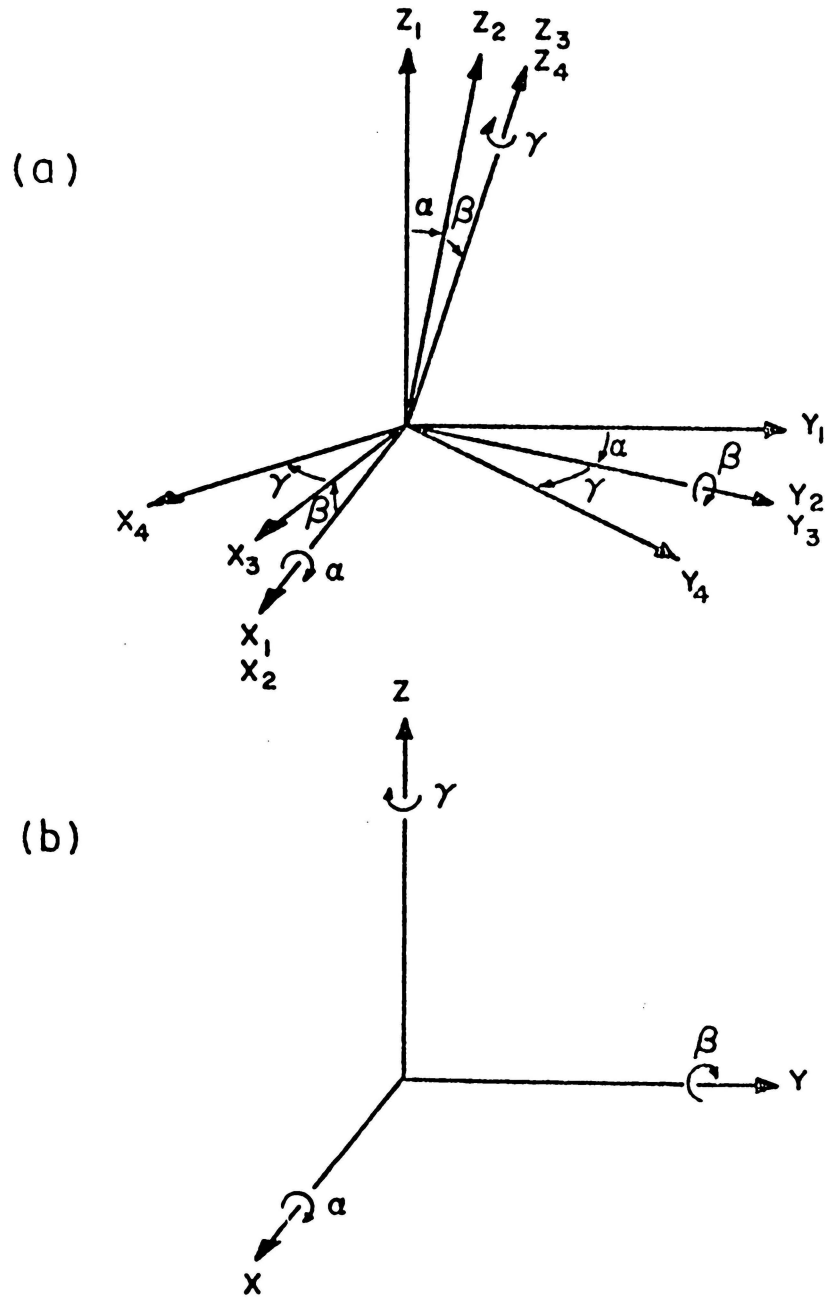

Fig. 2. Sequential rotations of a coordinate system. α, β, and γ are Eulerian angles. (a) Each rotation is performed about the "new" axis. (b) Each rotation is performed about the "old" axis.

$$A = \begin{bmatrix} 1 & 0 & 0 \\ 0 & \cos\alpha & -\sin\alpha \\ 0 & \sin\alpha & \cos\alpha \end{bmatrix} \tag{11a}$$

$$B = \begin{bmatrix} \cos\beta & 0 & \sin\beta \\ 0 & 1 & 0 \\ -\sin\beta & 0 & \cos\beta \end{bmatrix} \tag{11b}$$

$$C = \begin{bmatrix} \cos\gamma & -\sin\gamma & 0 \\ \sin\gamma & \cos\gamma & 0 \\ 0 & 0 & 1 \end{bmatrix}. \tag{11c}$$

It should be mentioned that a convention which takes an angle of clockwise rotation as a positive angle and an angle of counter-clockwise rotation as a negative angle is used in the present study. In other words, [A], [B], or [C] each represent a right hand rotation about X, Y, or Z axes, if the corresponding Eulerian angle has a positive value. It should also be noted that the matrix representing the first rotation is placed at the last along the matrix multiplication sequence. The resultant matrix [R] is a matrix which defined B1 with respect to B4, and therefore represents the rotation of B1 to B4.

On the other hand, if the sequential rotations are performed about "old" axes, as is seen in Figure 2(b), the sequence becomes

(1) B1 → B2 about X_1 by angle α, represented by [A],

(2) B2 → B3 about Y_1 by angle β, represented by [B],

(3) B3 → B4 about Z_1 by angle γ, represented by [C].

Of course, the positions of B2, B3, and B4 will differ from those shown in Figure 2(a). The resultant rotation matrix [R'] specifying the rotation of B1 to B4 is given by

$$[R'] = [A][B][C] \tag{12}$$

where [A], [B], and [C] have the forms given in equations (11a), (11b), and (11c). This equation can be derived by making use of the similarity transformations

$$[R'] = ([A][B][C][B]^{-1}[A]^{-1}) ([A][B][A]^{-1})[A] \tag{13}$$

where the group in the first parenthesis is a rotation about the old Z_1 axis, and the group in the second parenthesis is a rotation about the old Y_1 axis. Upon cancellation, equation (12) is obtained. It is to be noted that the sequence of matrix multiplication in equation (12) is inverse to that in equation (11). If the angles α, β, and γ in equation (11) are respectively equal to those in equation (12), [R] will be equal to $[R']^{-1}$. Therefore, the inverse sequence of rotations about the old axes will lead to the same final position performed by the normal sequence of rotations about the new axes.

3. Axis and Angle of Rotation

A given rotation of coordinate system can be accomplished by a single rotation about a certain axis, as is seen in Figure 3 in which basis 1 is rotated into basis 2. The axis of rotation $[\bar{E}]$ and angle of rotation φ can be determined from a matrix [R] which represents the rotation.

The axis of rotation is obtained by making use of an eigenvalue equation

$$\lambda\,[\bar{E}] = [R]\,[\bar{E}] \tag{14}$$

where λ is a constant specifying the eigenvalues of [R]. According to Euler's theorem, the real orthogonal matrix specifying the physical motion of a rigid body with one point fixed always has an eigenvalue equal to +1. With $\lambda = 1$, it is seen that $[\bar{E}]$ is an invariant vector upon rotation, and is therefore the axis of rotation. The coordinates of $[\bar{E}]$ are then solved from the rearranged and expanded form of equation (14)

$$\begin{aligned}
(r_{11}-1)\,X_E + r_{12}\,Y_E + r_{13}\,Z_E &= 0 \\
r_{21}\,X_E + (r_{22}-1)\,Y_E + r_{23}\,Z_E &= 0 \\
r_{31}\,X_E + r_{32}\,Y_E + (r_{33}-1)\,Z_E &= 0
\end{aligned} \tag{15}$$

where r_{ij} are elements of [R], and X_E, Y_E, and Z_E are the coordinates of $[\bar{E}]$.

The angle of rotation is obtained by means of similarity transformations, such as:

$$[R] = [T]^{-1}\,[S]\,[T]$$

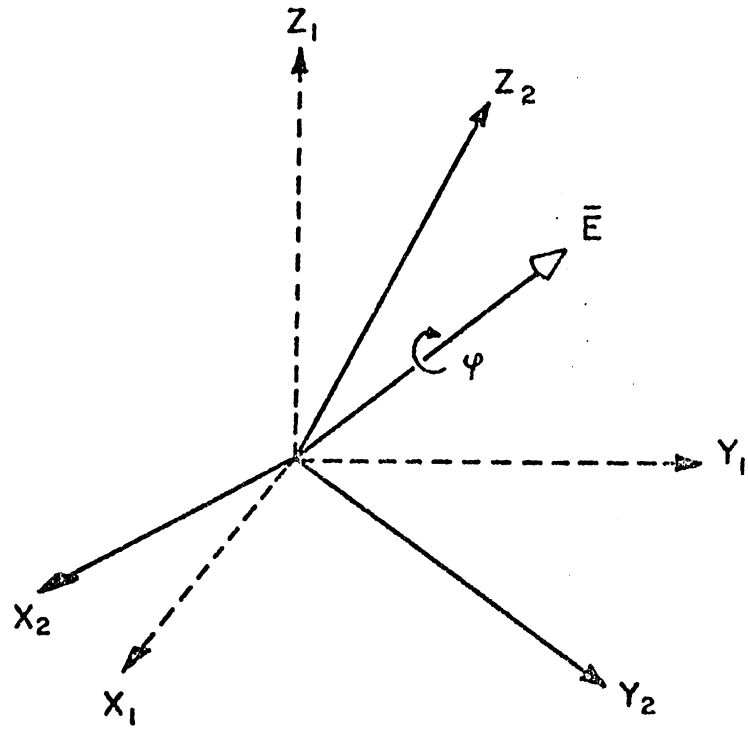

Fig. 3. Rotation of coordinate accomplished by a single rotation about the axis of rotation $\bar{E}$ by an angle φ.

where [T] is a matrix which transfers B1 to a system with the Z axis lying along the axis of rotation [$\bar{E}$]. Therefore the similarity transformation matrix [S] has the form

$$[S] = \begin{bmatrix} \cos\varphi & -\sin\varphi & 0 \\ \sin\varphi & \cos\varphi & 0 \\ 0 & 0 & 1 \end{bmatrix} \tag{16}$$

and the trace $\sum_{i=1}^{3} s_{ii} = 1 + 2\cos\varphi$. The angle φ can be solved in terms of the matrix elements.

4. Lattice Transformation Matrix

Coordinate transformation is easier to perform on an orthogonal basis. Therefore, in the study of crystals other than cubic systems, lattice transformation to a cubic system is often desired. Figure 4 shows an orthonormal basis and a most general lattice basis, triclinic system, both sharing the same origin and the same direction for $\bar{a}$ axes. The lattice transformation matrix [L] which defines the triclinic axes with respect to the cubic basis has been given by Morris[23], and is

$$[L] = [\ell_{ij}] \tag{17}$$

where $\ell_{11} = a$

$\ell_{21} = 0$

$\ell_{31} = 0$

$\ell_{12} = b \cos\gamma$

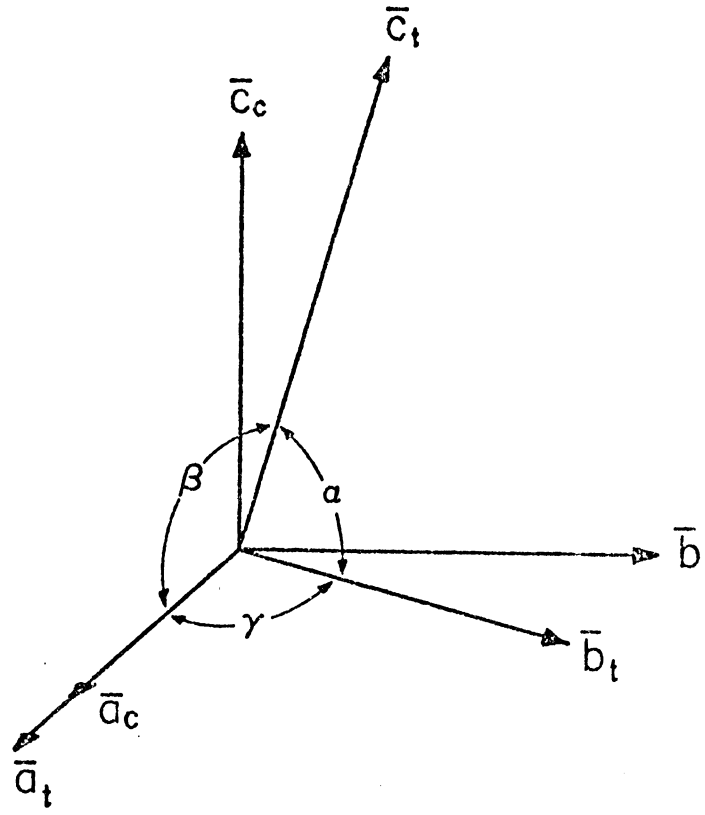

Fig. 4. Relation between a normalized cubic basis and a triclinic coordinate basis. Both systems share the same origin and the same direction for $\bar{a}$ axes.

$$\ell_{22} = b \sin \gamma$$

$$\ell_{32} = 0$$

$$\ell_{13} = c \cos \beta$$

$$\ell_{23} = c \, (\cos \alpha - \cos \beta \cos \gamma)$$

$$\ell_{33} = c \, \{1 + \cos\alpha \cos\beta \cos\gamma - [\cos^2\alpha + \cos^2\beta \, (1 + \cos^2\gamma)]\}^{\frac{1}{2}}.$$

Here, a, b, c, α, β, and γ are lattice parameters and angles for the triclinic system. Transformations of a vector or zone axis $\bar{V}$ between triclinic, $[\bar{V}]_t$, and cubic systems, $[\bar{V}]_c$, are performed by

$$[\bar{V}]_c = [L] \, [\bar{V}]_t \tag{18}$$

$$[\bar{V}]_t = [L]^{-1} \, [\bar{V}]_c \, . \tag{19}$$

For the case of hexagonal crystals the transformation matrices are

$$[HC] = [L] = a \begin{bmatrix} 1 & -1/2 & 0 \\ 0 & \sqrt{3}/2 & 0 \\ 0 & 0 & c/a \end{bmatrix} \tag{20a}$$

$$[CH] = [L]^{-1} = \frac{1}{a} \begin{bmatrix} 1 & 1/\sqrt{3} & 0 \\ 0 & 2/\sqrt{3} & 0 \\ 0 & 0 & a/c \end{bmatrix} \tag{20b}$$

where [HC] is a hexagonal-to-cubic transformation matrix, and [CH] is a cubic-to-hexagonal transformation matrix.

For crystals other than cubic systems, the zone axis [hkℓ] and the normal of the (hkℓ) plane are in general not the same vector. The

transformation of a plane normal from non-cubic to a cubic system can be performed by making use of the definition of reciprocal lattice. Here again the two systems shown in Figure 4 are taken as an example. The transformation matrix is given by

$$[Q] = [q_{ij}] = \begin{bmatrix} a_1^* & b_1^* & c_1^* \\ a_2^* & b_2^* & c_2^* \\ a_3^* & b_3^* & c_3^* \end{bmatrix}_c \tag{21}$$

where a_i^*, b_i^*, and c_i^*, $i = 1,2,3$, are respectively the coordinates of $[\bar{a}_t^*]_c$, $[\bar{b}_t^*]_c$, and $[\bar{c}_t^*]_c$, i.e., the translation vectors of the reciprocal lattice of the triclinic system referenced to the cubic basis. The elements of each column of [Q] are obtained by

$$q_{i1} = [\bar{a}_t^*]_c = \frac{[\bar{b}_t]_c \times [\bar{c}_t]_c}{V} \tag{22a}$$

$$q_{i2} = [\bar{b}_t^*]_c = \frac{[\bar{c}_t]_c \times [\bar{a}_t]_c}{V} \tag{22b}$$

$$q_{i3} = [\bar{c}_t^*]_c = \frac{[\bar{a}_t]_c \times [\bar{b}_t]_c}{V} \tag{22c}$$

where $[\bar{a}_t]_c$, $[\bar{b}_t]_c$, and $[\bar{c}_t]_c$ are respectively the coordinates of the lattice translation vectors of the triclinic system referenced to the cubic basis, and V is the volume of the triclinic unit cell, which

is equal to $[\bar{a}_t] \times [\bar{b}_t] \cdot [\bar{c}_t]$. The coordinates of $[\bar{a}_t]_c$, $[\bar{b}_t]_c$, and $[\bar{c}_t]_c$, i.e., a_i, b_i, and c_i, $i = 1,2,3$, are obtained from

$$\begin{bmatrix} a_1 & b_1 & c_1 \\ a_2 & b_2 & c_2 \\ a_3 & b_3 & c_3 \end{bmatrix} = [L] \begin{bmatrix} 1 & 0 & 0 \\ 0 & 1 & 0 \\ 0 & 0 & 1 \end{bmatrix} \tag{22d}$$

where [L] is lattice transformation matrix previously defined in equation (17). Therefore, the Miller indices (hkℓ) of a crystallographic plane in the triclinic system, i.e., the [hkℓ] vector in the reciprocal triclinic lattice, can be transferred to the cubic basis by the equation

$$\begin{bmatrix} h' \\ k' \\ \ell' \end{bmatrix}_c = [Q] \begin{bmatrix} h \\ k \\ \ell \end{bmatrix}_t \tag{23}$$

where h', k', and ℓ' are the coordinates of the plane normal referenced to the cubic basis.

B. Determination of Bicrystal Parameters

Three parameters, i.e., misorientation angle, misorientation axis, and boundary normal, have been used in the present study to characterize a general bicrystal, such as two adjacent grains or subgrains, a twin, or two neighboring phases. The bulk calculation for determining these bicrystal parameters was carried out by a computer program written in FORTRAN language.

To establish the orientation relationship of a general bicrystal from two Kikuchi patterns, three orthonormal coordinate frames, i.e., the crystal frame, pattern frame, and reference frame, are commonly involved. The three coordinate frames all follow the right hand convention and share a common origin, the center beam spot. The crystal frame, CF, is chosen from crystal lattice space. For the cubic crystal system, it is most convenient to use the three orthogonal translation vectors of the crystal lattice as the crystal frame. The pattern frame, PF, is selected from each of the two observed Kikuchi patterns. The reference frame, RF, which is common to both Kikuchi patterns is selected by consideration of convenience. Through the use of PF, a rotation matrix representing the rotation of CF to RF can be formulated for each of the patterns; and through the use of RF, a misorientation matrix specifying the CF of one crystal with respect to that of the other crystal can be obtained from the two Kikuchi patterns. The axis and angle of misorientation are then calculated using the misorientation matrix.

The boundary normal of a general bicrystal can sometimes be determined

by bringing the boundary plane parallel to the incident electron beam by means of specimen tilt. However, this condition is not always possible. An analysis has been developed in the present study to determine the boundary normal for the most general case. It requires no knowledge of foil thickness and foil inclination, but does require a moderate tilt of the specimen inside the microscope. Boundary images at the same magnification and Kikuchi patterns of the same crystal are taken before and after tilting. A rotation matrix representing the actual specimen tilt can be formulated from the Kikuchi patterns. This rotation matrix, together with the change of projected boundary images, such as the change of vectors lying on the boundary plane, the change of boundary width, or the change of boundary trace direction, are used to calculate the boundary normal.

In the following, the analytical procedures for formulating various matrices and determining boundary normals are given for cubic crystals. The analysis can be applied to crystals of other systems by minor modifications.

1. Matrix Formulation from a Kikuchi Pattern

A matrix [CR] which specifies the rotation of CF to RF can be formulated from each observed Kikuchi pattern. Figure 5 is a pattern taken from an aged Al - 0.5 at.% Ag alloy. The beam stop is introduced into the figure to serve as a reference line to establish RF. The use of the beam stop will be discussed later. The crystal frame is not shown on the pattern. The reference frame is selected such that the Z_R axis is parallel to the incident beam and is directed out of the paper. The X_R is chosen

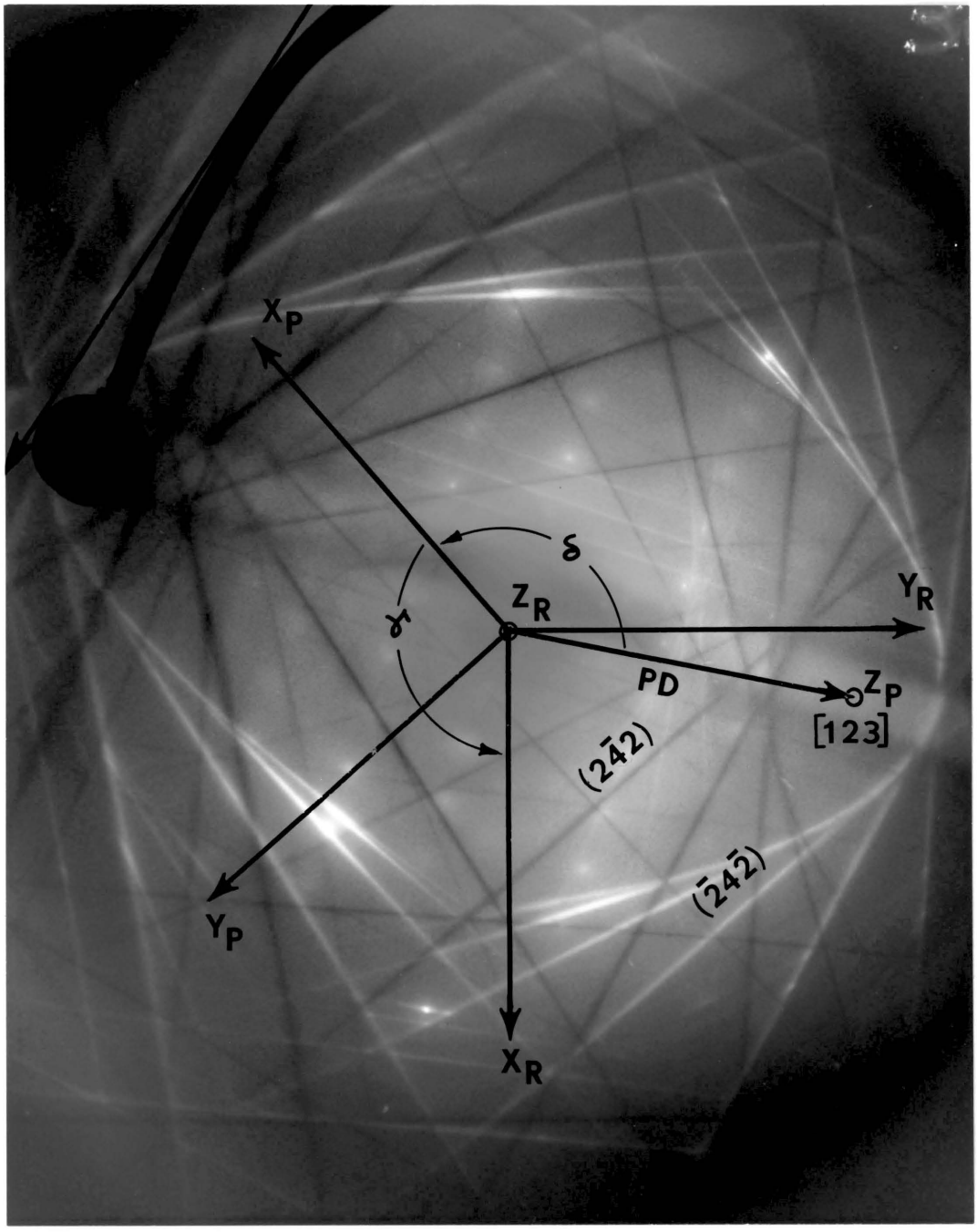

Fig. 5. Kikuchi pattern showing the selection of coordinate frames and the angles to be measured for the formulation of matrix [CR]. The pattern frame and reference frame are represented by $(X, Y, Z)_P$ and $(X, Y, Z)_R$, respectively.

by convenience. In this case, it was selected as the direction 32.5° counter-clockwise from the arrow shown tangent to the beam stop. There are two ways to select a pattern frame from each pattern. The first uses a Kikuchi pole, as is seen in Figure 5. The second, which requires the solution of the beam axis will be described later.

In Figure 5, the pattern frame is selected so that the Z_P axis is parallel to the [123] pole and is pointed out of the paper. The X_P axis, upon arbitrary selection, is perpendicular to the $(2\bar{4}2)$ plane, and is therefore drawn to be perpendicular to the $(2\bar{4}2)$ Kikuchi line. The coordinates of Z_P and X_P axes, when referred to CF, are defined as $[123]/\sqrt{14}$ and $[2\bar{4}2]/\sqrt{24}$, respectively. The Y_P axis is simply the cross product of Z_P and X_P. It should be noted that if the X_P axis is drawn in a direction opposite to that shown on the pattern, the X_P axis will then be defined as $[\bar{2}4\bar{2}]/\sqrt{24}$. A rotation matrix [CP] representing the rotation of CF to PF, according to equation (6), is

$$[CP] = \begin{bmatrix} 2/\sqrt{24} & -4/\sqrt{24} & 2/\sqrt{24} \\ 4/\sqrt{21} & 1/\sqrt{21} & -2/\sqrt{21} \\ 1/\sqrt{14} & 2/\sqrt{14} & 3/\sqrt{14} \end{bmatrix}.$$

The matrix [PR] specifying the rotation of PF to RF is determined next. The angle between the [123] pole and the transmitted electron beam axis, designated by PA, is calculated from the equation:

$$PA = \tan^{-1}(PD/CL) \qquad (24)$$

where PD is the distance on the photograph between the [123] pole center and the center beam spot, and CL is the effective camera length. By using equations (11) and (12), it can be proved that

$$[PR] = [C]\,[B]\,[A] \tag{25}$$

where [A], [B], and [C] are matrices representing the sequential rotations about the "new" X_P, Y_P, and Z_P axes of the pattern frame, and have corresponding Eulerian angles α, β, and γ, respectively. The angle α and β are computed by

$$\alpha = PA\ (\sin\delta) \tag{26a}$$

$$\beta = PA\ (\cos\delta) \tag{26b}$$

where δ is the projected angle measured from Z_P to X_P. The angle γ is measured from X_P to X_R. A negative sign should be given to δ and γ if the measurement is made in the counter-clockwise direction.

A rotation matrix [CR] which represents the rotation of CF to RF is then given by

$$[CR] = [PR]\,[CP]. \tag{27}$$

This matrix and its inverse matrix will be used in transferring vectors between CF and RF. A given vector based on RF of the observed pattern is readily transferred to CF by

$$\begin{bmatrix} X \\ Y \\ Z \end{bmatrix}_{CF} = [CR]^{-1} \begin{bmatrix} X \\ Y \\ Z \end{bmatrix}_{RF}. \tag{28}$$

The beam axis of a Kikuchi pattern may be solved using the matrix [CR]. The coordinates of the beam axis based on CF, designated by X_B, Y_B, and Z_B, according to equation (28), are

$$\begin{bmatrix} X_B \\ Y_B \\ Z_B \end{bmatrix} = [CR]^{-1} \begin{bmatrix} 0 \\ 0 \\ 1 \end{bmatrix}. \qquad (29)$$

Since [CR] is formulated by using only one Kikuchi pole, equation (29) appears to be a one-pole matrix solution of the beam axis. Such a solution, however, is based upon correct indexing of the Kikuchi lines around the Kikuchi pole. Frequently, on a pattern taken using pole piece no. 3 or no. 4, only one Kikuchi pole may be recognized. By careful inspection or comparison with Kikuchi maps, the single pole can usually be indexed unambiguously.

As mentioned previously, there is a second way to select PF from each Kikuchi pattern. In this second approach, the beam axis is first solved either by the three-pole solution, two-pole solution, or some other solution. The normalized coordinates of the beam axis are then used to define the Z_P axis. Thus the Z_P axis becomes parallel to the Z_R axis. The Y_P axis can be chosen parallel to any of the Kikuchi lines. If, for example, in Figure 5 the Y_P axis is chosen to be parallel to the $(2\bar{4}2)$ Kikuchi line, its coordinates are specified by the cross product of Z_P and $[2\bar{4}2]/\sqrt{24}$. The X_P axis is the cross product of Y_P and Z_P. Once PF is defined, the matrix [CP] is readily obtained from equation (6). The rotation of PF to RF is then performed by a single rotation about Z_P or Z_R. Therefore, according to equation (25), when [A] and [B] become identity matrices, [PR] = [C].

The matrix [CR] has the same form as that given in equation (27).

In the present study, the first approach which does not require the solution of the beam axis is employed, since it is more generally applicable.

2. Misorientation Matrix for a High-Angle Bicrystal

To determine the orientation relationship between two crystals of a high-angle bicrystal, two separate Kikuchi patterns are required, each taken from one of the two crystals. Since the edges of photographic plates stacked inside the camera chamber are not perfectly parallel to each other, an invariant reference line must be introduced into each of the photographic plates. In the present study, this was done by setting the beam stop at one corner of each of the plates. The reference frame is then selected by reference to the beam stop.

Figure 6 shows how two crystals, crystal 1 and crystal 2, are related through the use of two pattern frames and a common reference frame. Matrices representing the various stages of rotation are also given. The directions of various rotations are indicated by the arrows. From this figure it is seen that

$$[CR1] = [PR1]\ [CP1] \tag{30a}$$

$$[CR2] = [PR2]\ [CP2] \tag{30b}$$

$$[M12] = [CR2]^{-1}\ [CR1] = [CP2]^{-1}[PR2]^{-1}[PR1][CP1]. \tag{31}$$

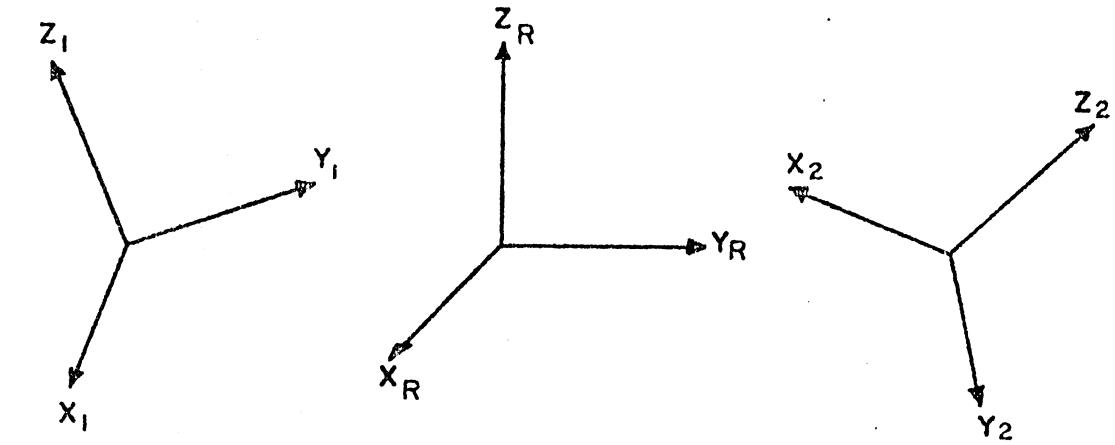

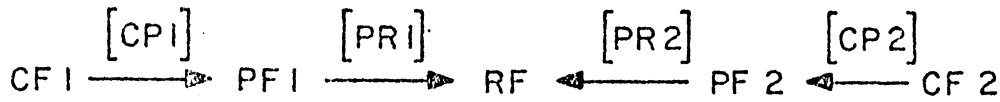

$$[M12] = [CR2]^{-1}\,[CR1] = [CP2]^{-1}\,[PR2]^{-1}\,[PR1]\,[CP1]$$

Fig. 6. Schematic representation of the relation between two crystal coordinate frames, CF1 and CF2, and a reference coordinate frame, RF. Various stages of rotation are indicated by the arrows and the corresponding rotation matrices. [M12] is a matrix specifying the rotation of CF1 to CF2.

The definitions are:

[CR1] = a matrix defining CF1 with respect to RF,

[CR2] = a matrix defining CF2 with respect to RF,

[M12] = a misorientation matrix specifying CF1 with respect to CF2.

The axis and angle of misorientation are calculated from [M12], or $[M12]^{-1}$, by making use of equations (15) and (16).

Because of crystal symmetry, [M12] is not unique for crystals other than the triclinic system; e.g., there are 24 degrees of freedom for cubic systems. This means that there are 24 ways to index a Kikuchi pattern taken from a cubic crystal. Consequently, a total of 24 misorientation matrices can be obtained. Each of them correctly defines the orientation relationship of the bicrystal. Once a misorientation matrix is obtained, the other 23 degeneracy matrices are calculated by

$$[M12]_i = [D]_i [M12] \qquad i = 2,3,\ldots,24. \tag{32a}$$

Here $[D]_i$ is a matrix for the ith symmetry operation. It has the form of equation (11), i.e.,

$$[D]_i = [C]_i [B]_i [A]_i \tag{32b}$$

in which each of the Eulerian angles has a value of either $0, \pi/2$ or π.

3. Misorientation Matrix for a Low-Angle Bicrystal

On a pattern taken from an area across a high-angle boundary two completely different Kikuchi patterns will be found superimposed onto each other, and the indexing of patterns will be difficult. On the other hand, on a pattern taken from an area across the boundary of a low-angle bicrystal the Kikuchi pattern is always found to split into two sets, and the splitting of the pattern introduces no problems in indexing. Figure 7 shows such a pattern taken from a pure aluminum specimen. The selection of coordinate frames is depicted in a schematic pattern given in Figure 8 in which the twist angle γ_1 about the beam axis is exaggerated. Two identical pattern frames, PF1 and PF2, which differ only in orientation are selected in a manner similar to those chosen for the case of a high-angle bicrystal. A reference frame is still required. It is chosen so that the Z_R axis is parallel to the transmitted electron beam and is pointing out of the paper. The X_R axis is parallel to the projection of the X_{P2} axis, i.e., the X axis of PF2.

The matrices defining the rotation of PF1 to RF and the rotation of PF2 to RF are obtained from equation (25). The corresponding Eulerian angles α_1, β_1, α_2, and β_2 are calculated using equation (26). Since X_R is parallel to the projection of X_{P2}, the angle γ_2 is equal to zero. The angle γ_1 is the twist angle between two split identical Kikuchi lines about the transmitted beam. This angle is not magnified by the microscope, and therefore must be measured with great care. On an 8" x 10" magnified pattern with fairly sharp Kikuchi lines, a measurement to an accuracy of $\pm 0.05^{\circ}$ can be achieved. The error involved in this measurement is the

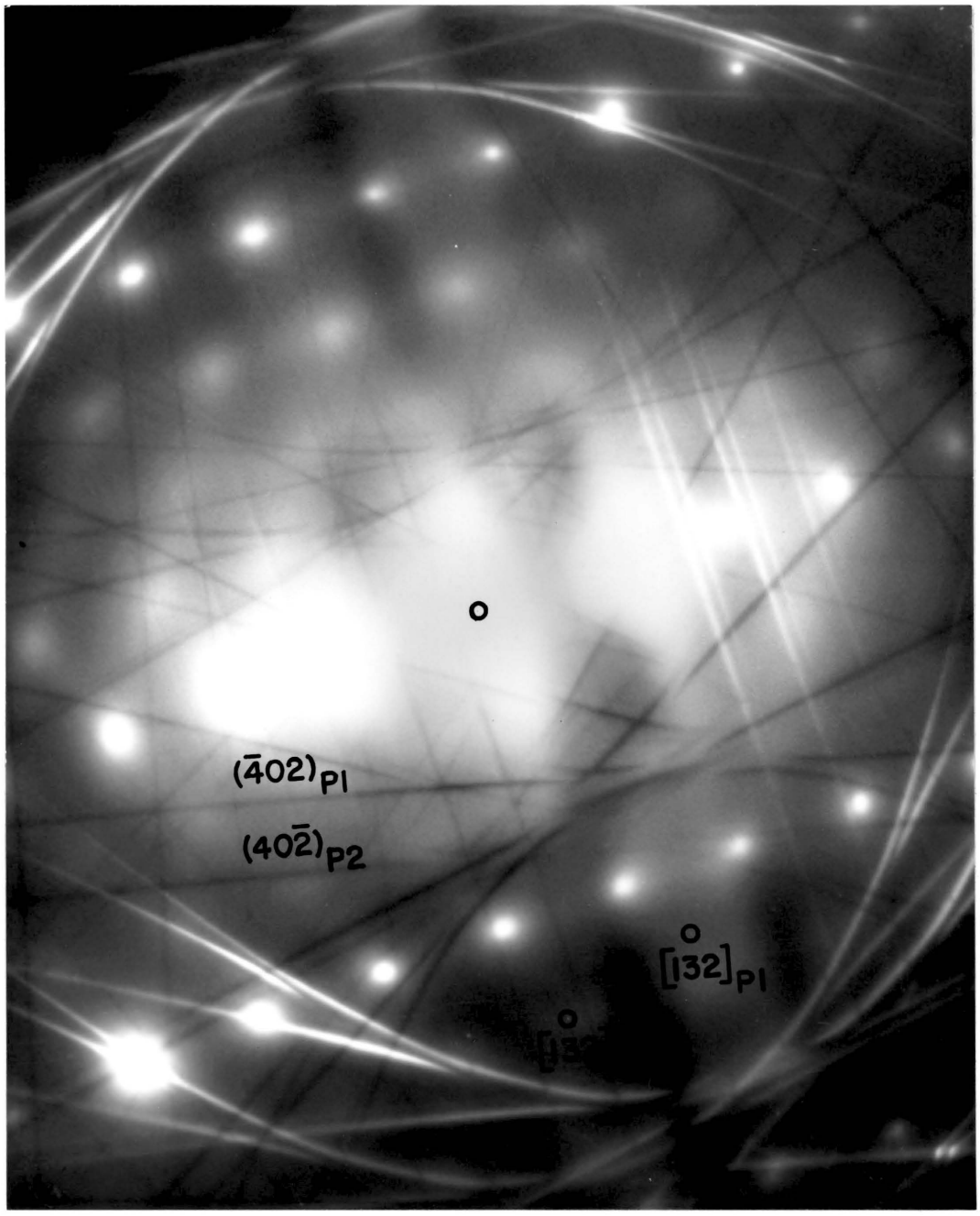

Fig. 7. A Kikuchi pattern taken from an area across a subgrain boundary of aluminum crystal. The pattern is seen to split into two sets.

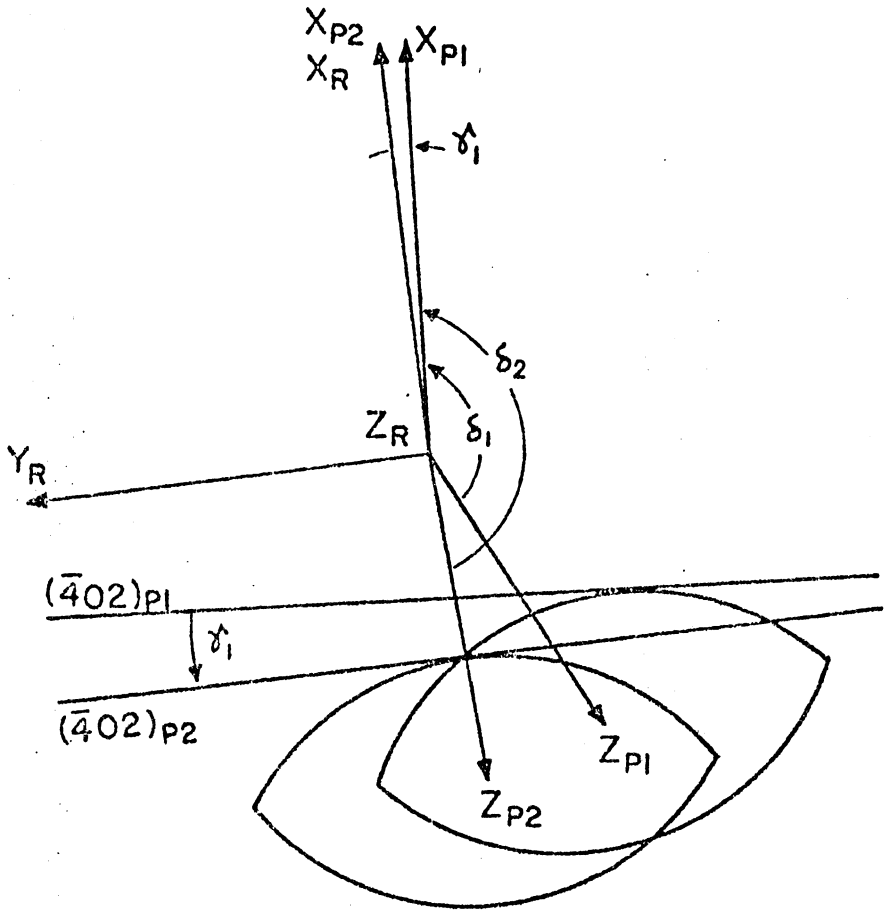

Fig. 8. Schematic representation of the split Kikuchi pattern shown in Figure 7, showing the selection of coordinate frames and the angles to be measured for the formulation of matrix [M12] for a low-angle bicrystal.

major source of error in this analysis.

A chart indicating the various stages of rotation becomes

$$CF1 \xrightarrow{[CP]} PF1 \xrightarrow{[PR1]} RF \xleftarrow{[PR2]} PF2 \xleftarrow{[CP]} CF2$$

where [CP] = [CP1] = [CP2]. The misorientation matrix is given by

$$[M12] = [CP]^{-1} [PR2]^{-1} [PR1] [CP]. \tag{33}$$

The axis and angle of misorientation are calculated from this matrix using equations (15) and (16).

4. Rotation Matrix Representing Specimen Tilt

The procedures for determining a boundary normal require two steps. First, a rotation matrix which represents the actual specimen tilt in the microscope is obtained from two Kikuchi patterns taken from the same crystal before and after tilting. Second, two vectors both lying on the same boundary plane are selected on each of the two micrographs taken before and after tilt. The X-Y coordinates of each vector are measured based on a reference frame selected on each micrograph. The reference frames on the two patterns and the two micrographs must be selected in exactly the same manner. The Z component of each vector is calculated using the rotation matrix. The boundary normal is then obtained by taking the cross product of the two vectors. It can be seen that the rotation matrix needed here is a matrix specifying the actual rotation of a vector as a result of specimen tilting based on the invariant reference frame chosen from the micrographs.

There are 24 ways to index a Kikuchi pattern taken from a cubic crystal. Consequently, there are a total of 24 degeneracy rotation matrices, and each correctly relates the specimen orientation before and after tilting. However, there is only one unique matrix representing the "actual" tilt. This means that once a pattern in indexed, the other pattern can only be indexed in a unique way. In this respect, Kikuchi maps each covering a wide angular range for different orientations are very helpful in providing the proper indexing of patterns. An example will be seen later.

The determination of a rotation matrix is schematically depicted in Figure 9. The unique rotation matrix defining the crystal frame after tilting, CF2, with respect to the crystal frame before tilting, CF1, is

$$[R21] = [CR1]^{-1} [CR2] . \tag{34}$$

Here, the definitions are:

[R21] = a matrix which rotates vectors, V_1 to V_2, based on CF1 or CF2.

[CRi] = a matrix which transfers a fixed vector from CFi to RF.

The similarity rotation matrix based on the reference frame is given by

$$[R] = [CR1] [R21] [CR1]^{-1} = [CR2] [CR1]^{-1}. \tag{35}$$

The similarity rotation based on the reference frame is performed by the equation

$$[\bar{V}_2]_{RF} = [R] [\bar{V}_1]_{RF} . \tag{36}$$

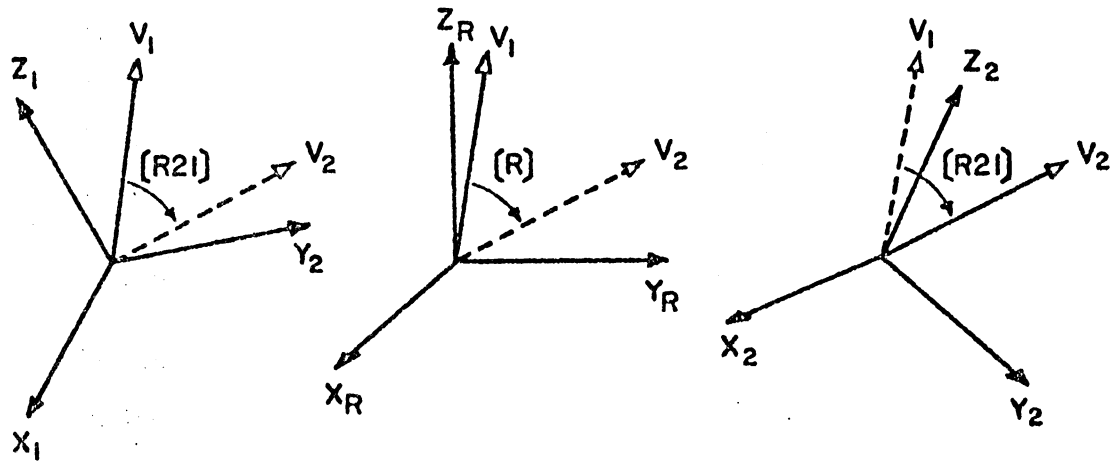

FIRST CRYSTAL FRAME (CF1) | REFERENCE FRAME (RF) | SECOND CRYSTAL FRAME (CF 2)

$$CF1 \xrightarrow{[CR1]} RF \xleftarrow{[CR2]} CF2$$

$$[R21] = [CR1]^{-1}\,[CR2]$$

$$[R] = [CR1]\,[R21]\,[CR1]^{-1} = [CR2]\,[CR1]^{-1}$$

Fig. 9 Schematic diagram showing the relations between the crystal frames before specimen tilt, (CF1), after tilt, (CF2), and the reference frame, (RF). The matrix [R] transfers a vector before tilt to a vector after tilt based on the reference frame.

This equation will be used to calculate the Z component of each boundary vector.

Equation (36) can be derived from another simple approach. Since $\bar{V}_1$ and $\bar{V}_2$ are the same vector $\bar{V}$ in crystal lattice space, the following equation can be established, i.e.,

$$[CR1]^{-1} [\bar{V}_1]_{RF} = [\bar{V}]_{CF} = [CR2]^{-1} [\bar{V}_2]_{RF} \tag{37}$$

$$[CR2] [CR1]^{-1} [\bar{V}_1]_{RF} = [\bar{V}_2]_{RF} . \tag{38}$$

The latter is an equation identical to that given in equation (36).

The reference coordinate frames on both patterns and micrographs are selected by referring to the invariant beam stop in the manner previously described. However, a relative rotation of images with respect to the diffraction pattern occurs which varies with magnification. This relative rotation has to be accounted for in the formulation of [CR1] and [CR2]. According to equation (27),

$$[CR] = [PR] [CP] = [C] [B] [A] [CP]$$

where [C] is a rotation of PF about the Z_P or Z_R axis, with its Eulerian angle γ measured on the pattern. The correction is done by subtracting the angle of relative image-pattern rotation from the measured γ. The accuracy of this correction will be discussed in Section V-C-3

5. Determination of Boundary Normals

As mentioned previously, two boundary vectors have to be selected in the determination of a boundary normal. Either of the two vectors could be: (1) a defined vector observed or drawn on the boundary plane, (2) a boundary width vector, or (3) a boundary trace direction. Results of higher accuracy can be obtained when the two vectors change their projected images most strongly with specimen tilt. Therefore, defined vectors, especially those joining the top and bottom surfaces of a thin foil, are preferred for this analysis. The boundary width vector is the second choice. A boundary trace direction is the last choice if none other is available. Also, two vectors with their angle of intersection being near 90^{o} is one of the best conditions for higher accuracy. This arises from the fact that in taking the cross product from two vectors with a small angle of intersection, a slight shifting of either one of the two vectors will lead to a large change in the product.

The X and Y components of each of the two boundary vectors are measured from micrographs by referring to a reference frame. The Z component is calculated by using the rotation matrix. The procedure in determining the Z component varies for different types of vectors selected. In the following, the method employed for each of the three different boundary vectors are given.

a. Determination of the Coordinates of a Defined Vector

A triple grain junction is used here as an example. Figure 10 shows the projected images of a triple grain junction before and after specimen

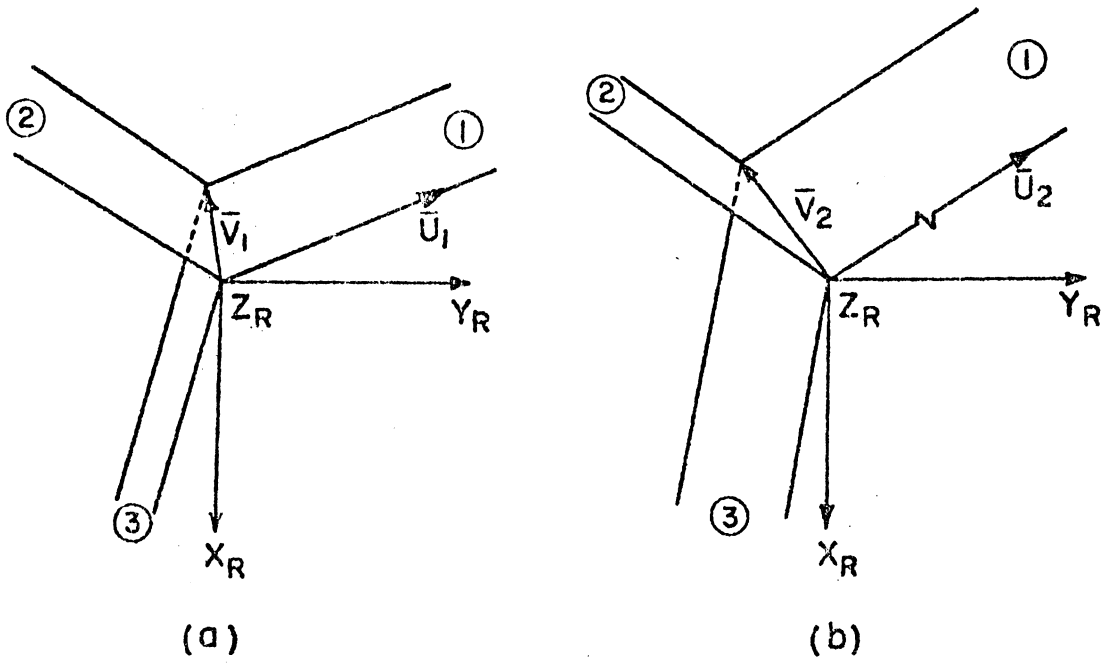

Fig. 10. Triple grain junction (a) before tilting, and (b) after tilting, together with the invariant reference frame.

tilt. The grain edge is a defined vector designated by $\bar{V}_1$ before tilt and $\bar{V}_2$ after tilt. The X and Y components of $\bar{V}_1$ and $\bar{V}_2$, labeled as X_{V1}, Y_{V1}, and X_{V2}, Y_{V2}, respectively, are measured from micrographs. The Z components are calculated using equation (36) which after expansion becomes

$$r_{11}X_{V1} + r_{12}Y_{V1} + r_{13}Z_{V1} = X_{V2} \tag{39a}$$

$$r_{21}X_{V1} + r_{22}Y_{V1} + r_{23}Z_{V1} = Y_{V2} \tag{39b}$$

$$r_{31}X_{V1} + r_{32}Y_{V1} + r_{33}Z_{V1} = Z_{V2} \tag{39c}$$

The two unknowns, Z_{V1} and Z_{V2}, are obtained by solving the three simultaneous equations. Z_{V2} can be computed using either equation (39a) or (39b), and the average value of the two is used in the present analysis.

b. Determination of the Direction of a Boundary Trace

In Figure 10 no distinguishable surface marks along traces of boundary 1 are shown. However, a trace vector $\bar{U}_1$ with definite length can be specified before rotation. After specimen tilt, the trace vector $\bar{U}_2$ becomes undefined in length. However, the ratio of the X and Y components of $\bar{U}_2$ is known. The coordinates of $\bar{U}_1$ and $\bar{U}_2$ can then be calculated from the equations

$$r_{11}X_{U1} + r_{12}Y_{U1} + r_{13}Z_{U1} = X_{U2} \tag{40a}$$

$$r_{21}X_{U1} + r_{22}Y_{U1} + r_{23}Z_{U1} = Y_{U2} \tag{40b}$$

$$r_{31}X_{U1} + r_{32}Y_{U1} + r_{33}Z_{U1} = Z_{U2} \tag{40c}$$

$$X_{U2}/Y_{U2} = C \tag{40d}$$

where X_{U1}, X_{U2}, Y_{U2}, and Z_{U2} are the unknowns to be solved.

c. Determination of the Coordinates of A Boundary Width Vector

In the present study, the boundary width vector is defined as a vector lying in a direction perpendicular to a projected boundary trace, and defining the true boundary width in that direction. Figure 11(a) and 11(b) represent the projected images of a boundary before and after specimen tilt, with the corresponding boundary width vectors labeled by $\overline{W}_1$ and $\overline{W}_2$ respectively. It should be noted that in general $\overline{W}_1$ and $\overline{W}_2$ are not the same vector. A boundary frame, BF1, is selected from Figure 11(a) so that the X_{B1} axis is parallel to a projected boundary trace and the Z_{B1} axis coincides with the Z_R axis of the reference frame. The boundary frame after specimen tilt is shown in Figure 11(b). One important point to be noted is that Z_{B2}, X_{B2}, and the boundary trace T_2 are coplanar.

In the following, the coordinates of $\overline{W}_1$ are to be determined. The X, Y components are measured from micrograph. In order to determine the Z component, the angular component of rotation about X_{B1} as a result of

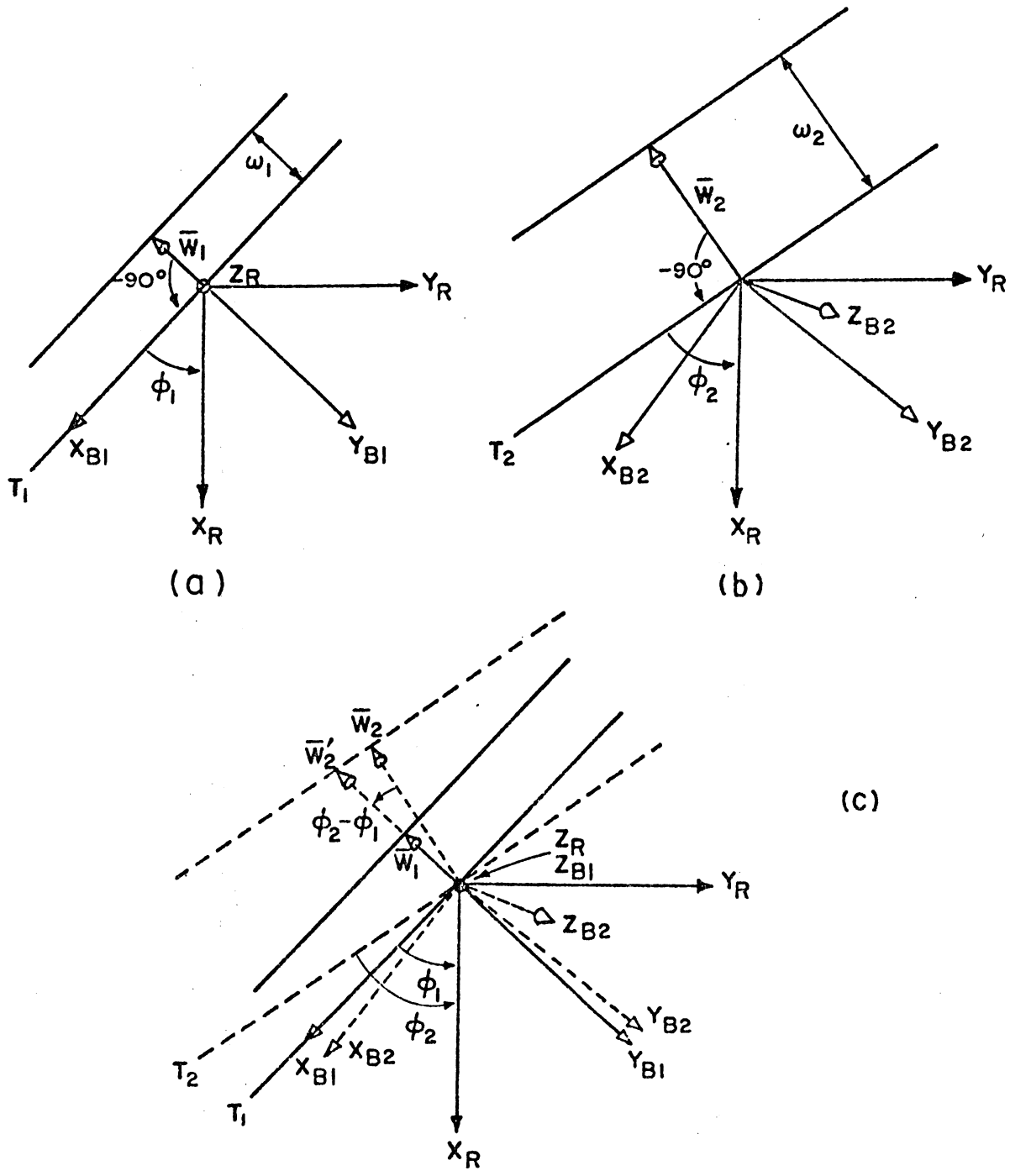

Fig. 11. Crystal boundary (a) before tilting, (b) after tilting, and (c) superposition of (a) with (b). A boundary frame is represented by $(X,Y,Z)_{B1}$ before tilting, and $(X,Y,Z)_{B2}$ after tilting. An invariant reference frame is indicated by $(X,Y,Z)_{R}$.

specimen tilt has to be calculated. With this angular component, $\Delta\theta$, and the projected lengths of $\bar{W}_1$ and $\bar{W}_2$, the Z component of $\bar{W}_1$ can be obtained. Figure 11(c) is a superposition of Figure 11(a) and 11(b) in which the image of (b) is shown by dashed lines. On boundary 2, a boundary width vector which is perpendicular to T_1 is drawn, and is designated by $\bar{W}_2'$. With the help of Figure 11(c) it is seen that a rotation about X_{B1}, which brings the projection of Z_{B2} parallel to T_1, will bring $\bar{W}_2'$ to coincide with $\bar{W}_1$. By knowing the coordinates of Z_{B2} based on BF1, the angle of this rotation, $\Delta\theta$, can be calculated. The coordinates of Z_{B2} referred to BF1 are computed by

$$\begin{bmatrix} X_{ZB2} \\ Y_{ZB2} \\ Z_{ZB2} \end{bmatrix}_{BF1} = [BR1]^{-1}\,[R]\,[BR1] \begin{bmatrix} 0 \\ 0 \\ 1 \end{bmatrix}_{BF1} \tag{41}$$

where [R]= a rotation matrix based on RF, i.e., equation (35),

[BR1] = a matrix defines BF1/RF.

The angle $\Delta\theta$ is calculated by

$$\Delta\theta = \tan^{-1}\,(Y_{ZB2}/Z_{ZB2}) \tag{42}$$

The angle of inclination of $\bar{W}_1$ and $\bar{W}_2'$, i.e., θ_1 and θ_2', are solved by

$$w_1 \cdot \mathrm{Cos}\,(\varphi_2 - \varphi_1) \,/\, w_2 = \mathrm{Cos}\,\theta_1 \,/\, \mathrm{Cos}\,\theta'_2 \tag{43a}$$

and

$$\Delta\theta = \theta'_2 - \theta_1 \tag{43b}$$

where w_1 and w_2 are the projected widths of $\bar{W}_1$ and $\bar{W}_2$. Here, the signs

of w_1 and w_2 are important. In this study, when $\bar{W}_i$ is pointing in a direction opposite to the direction of Y_{Bi}, w_i has been given a negative sign. Once θ_1 is known, the Z component of $\bar{W}_1$ can be determined. It is seen that the measured parameters needed for this calculation are w_1, w_2, θ_1, and θ_2. These parameters are readily obtained from the micrographs. The Z component of $\bar{W}_2$, if desired, can be determined following the same procedures in obtaining $\bar{W}_1$.

C. Computer Generation of Kikuchi Projections

Two FORTRAN programs have been written to generate computer plotting of standard stereographic projection of Kikuchi patterns. The first is for cubic crystals, including FCC, BCC, and diamond cubic, and the second is for hexagonal crystals. The programs provide for Kikuchi projections of any desired orientation and any desired projection sphere radius. They are applicable to a wide range of wave length. Coates projections and Kossel projections can be obtained from the same programs by using appropriate wave lengths. Kikuchi projections of small projection sphere radii which cover a wide angular range of Kikuchi space are sometimes referred to as Kikuchi maps.

In the following, the geometry involved in producing stereographic Kikuchi projections and the procedures for automatic indexing of the projections are described. The steps of program execution are also outlined.

1. Standard Stereographic Projection of Kikuchi Patterns

The geometry for the standard stereographic projection of a Kikuchi pair is shown in Figure 12, in which part (b) is the projection of part (a) with the observer looking from 0 toward S. In Figure 12(a), $\overline{DO}$ is the projection sphere radius; $\overline{DP}$ is the normal to the diffracting plane (hkℓ); θ is the Bragg angle for the (hkℓ) plane; A'DB' and $\bar{A}'\overline{DB}'$ are diffraction conics of (hkℓ) and ($\bar{h}\bar{k}\bar{\ell}$) planes, respectively; and P, A, and $\bar{A}$ are the projections of P', A', and $\bar{A}'$, respectively. In Figure 12 (b), the full circle is the basic circle with radius $\overline{OR}$ equal to twice the radius $\overline{DO}$. The (hkℓ) and ($\bar{h}$ $\bar{k}$ $\bar{\ell}$) Kikuchi lines are projections of the intersections between diffraction conics and the projection sphere, and therefore appear as small circles on the projection plane. Determination of the centers and the radii of these Kikuchi circles will be seen later. Since the Bragg angles for high energy electron diffraction are usually small, $<2^{o}$, the projected Kikuchi lines usually appear nearly straight and in pairs. The number of Kikuchi lines to be drawn on the projection is limited by using a cut-off parameter. For cubic crystals, a maximum S value (MS), where $S = h^2 + k^2 + \ell^2$, is used as a cut-off point. Kikuchi lines for crystallographic planes whose S value is greater than MS will not be plotted. For HCP crystals, a maximum squared value of reciprocal d-spacing (RD), i.e., $1/d^2$, is used as the limiting parameter. Kikuchi lines of those planes with their $1/d^2$ value greater than RD will not be drawn on the plot. The best selection of MS or RD depends on the projection sphere radius. Details for selecting MS and RD are given in the Appendix A.

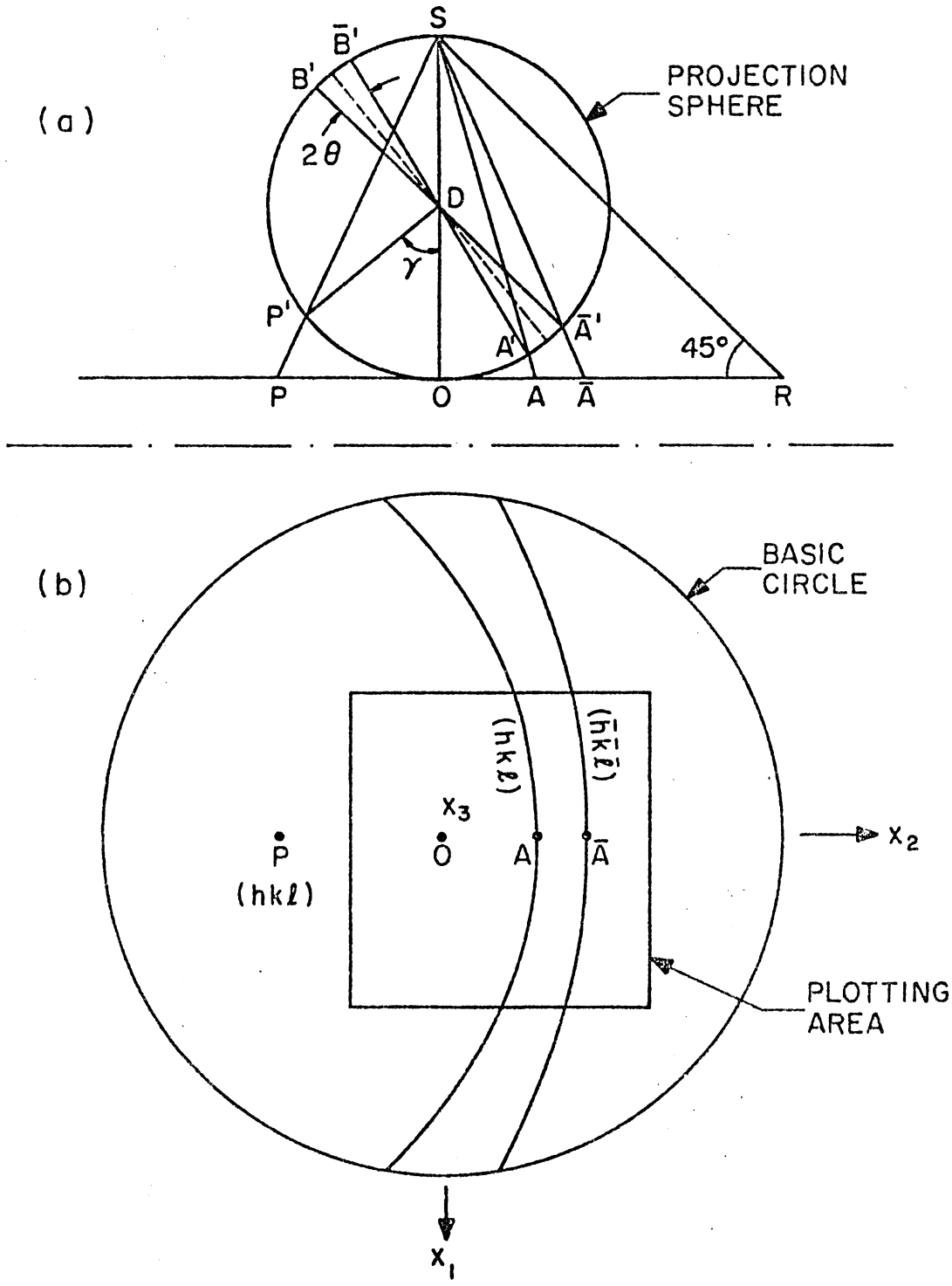

Fig. 12. Geometry for standard stereographic projection of the (hkℓ) Kikuchi pair. Part (b) is the projection of part (a). X_1, X_2, and X_3 are the describing orientations of stereographic projections.

For each Kikuchi projection a rectangular plotting area is specified, as is seen in Figure 12(b). The CALCOMP plotter used in this study could provide a plotting area of 11" maximum width and essentially unlimited length. The origin of projection, O, can be located at any position inside the rectangular area. If a projection of full circle is to be made, the specified area must be large enough to cover the whole basic circle, or the basic circle should be small enough to be contained entirely inside the plotting area.

In Figure 12(b) an orthonormal set of reference axes, called the standard basis, with its origin set at the origin of projection is also shown. In the standard basis, the X_1 and X_2 axes lie on the projection plane and are parallel to the edges of the rectangular plotting area. The X_3 axis is perpendicular to the projection plane and is directed out of the paper. By specification of the X_1 and X_3 axes, Kikuchi projections of any desired orientation can be produced.

According to Figure 12, the coordinates PX and PY of a projected Kikuchi pole (P), referenced to the projected standard basis (X_1 and X_2), can be calculated using the following equations:

$$PX = 2\overline{DO} \cdot \tan(\gamma/2) \cdot (PX'/\sqrt{PX'^2 + PY'^2}) \tag{44a}$$

$$PY = 2\overline{DO} \cdot \tan(\gamma/2) \cdot (PY'/\sqrt{PX'^2 + PY'^2}) \tag{44b}$$

$$\gamma = \mathrm{Cos}^{-1} (PZ'/\sqrt{PX'^2 + PY'^2 + PZ'^2}) \tag{45}$$

where PX', PY', and PZ' are the coordinates of the Kikuchi pole (P') referenced to the standard basis, and γ is the angle between the pole and the X_3 axis of the standard basis.

Coates projections, Kossel projections, and psuedo-Kossel projections may be generated following exactly the same construction mechanism for Kikuchi projections. Examples of Coates and psuedo-Kossel patterns are shown later in Figures 33 and 34, respectively.

2. Automatic Indexing of Kikuchi Projections

A zone axis projection associated with each Kikuchi projection is generated to perform an automatic indexing of Kikuchi poles. In a zone projection, the location together with the directional indices of some selected zone axes corresponding to the existing Kikuchi poles on the projection are plotted. Option is made available to plot the zone projection either on a separate sheet or on the corresponding Kikuchi projection, depending on the projection sphere radius.

Not all the Kikuchi poles appearing on the projection are indexed. They are selected by specifying the minimum number of diffracting zone planes associated with a pole. Only those poles having their number of first-order diffraction zone planes greater than the specified number are indexed. A maximum number for directional indices of zone axes is also specified, and the indices are permuted. The program described herein fixes this maximum number at nine for all zone axis indices. The number of diffraction zone planes associated with each generated zone axis is checked by taking the dot product with all the existing first-order Kikuchi pairs. Only those zone axes which have their number of zone planes greater than or equal to the specified minimum number are printed on the zone projection. The same procedures are employed in plotting zone axis projections for Coates patterns.

For x-ray diffraction the Bragg angles are large compared to those of electron diffraction. The diffraction lines on Kossel projections or pseudo-Kossel projections generally appear as segments of circles or full circles. In this case it has been found advantageous to plot Miller indices of diffracting planes on the zone axis projection.

For zone axis projections with smaller projection sphere radii, overlapping of printed indices will occur in many circumstances. When indices of two poles will overlap if printed, the pole with less diffraction zone planes is rejected. If both overlapping poles have the same number of diffraction zone planes, the one with the larger value of S, $S = h^2 + k^2 + \ell^2$, is rejected.

A print-out associated with each Kikuchi projection is also generated to provide for the indexing of individual Kikuchi lines. In this print-out, several parameters are listed: (1) the distance between the origin and the Kikuchi line, (2) the angle between the X_1 axis and the vector drawn from the origin perpendicular to the Kikuchi line, and (3) the line separation of a Kikuchi pair. From these listed parameters most of the existing Kikuchi lines can be easily indexed. For a cubic crystal, identification of individual Kikuchi lines can be done simply by taking the cross product of two Kikuchi poles. However, this is not applicable to crystals of other systems. Therefore, the printed list is especially useful in the study of non-cubic crystal systems.

3. Program Input Data

The input data to the computer are the following.

a. Direction of X_3 and X_1 axes of the standard basis for the desired stereographic projection.

b. Crystal structure and associated lattice parameters.

c. Projection sphere radius and electron wave length.

d. Maximum S value (MS) for cubic crystals or maximum squared value of reciprocal d-spacing (RD) for HCP crystals, and minimum number of diffraction zone planes (MDZP).

e. Index numbers indicating the option in plotting zone projection.

f. Size of the rectangular plotting area and the location of origin.

g. Titles for each plot.

4. Steps of Program Execution

The programs are executed in the following steps.

a. Formulation of transformation matrices:

(1) For the HCP case, the hexagonal-cubic transformation matrices, [HC] and [CH], are given.

(2) The matrix, [CP], defining the cubic basis with respect to the standard basis of the desired orientation is determined using equation (6).

b. Selection of diffraction planes:

(1) For both cubic and hexagonal cases, Miller indices of crystal planes are generated in three nested DO loops.

(2) Diffraction planes are selected among the generated planes using the selection rules based on structure factor considerations. Two cut-off parameters, the input MS or RD and the size of plotting area, are used to limit the

number of diffraction planes to be registered in storage.

(3) For the case of HCP crystals, Miller indices for plane normals are changed to the coordinates of a zone axis specifying the plane normals. The coordinates are then transferred to the cubic basis by using [HC].

(4) The coordinates of plane normals in the cubic basis are transferred to the standard basis of the desired orientation using matrix [CP]. The coordinates of plane normals on the projection plane are calculated using equation (44), and are registered as PX, PY arrays.

(5) The order of each registered diffraction plane is determined.

c. Selection of zone axes:

(1) Again, for both cubic and hexagonal cases, integer coordinates of zone axes, each ranging from -9 to +9, are generated in another three nested DO loops.

(2) The number of existing first-order diffraction zone planes associated with each generated zone axis is calculated. The axes having their numbers of zone planes greater than or equal to MDZP are registered in storage.

(3) For the HCP case, coordinates of registered zone axes are transferred to the cubic basis using [HC].

(4) Coordinates of zone axes in the cubic basis are transferred to the standard basis of the desired orientation. The X-Y coordinates of zone axes on the projection plane are calculated and stored as ZX, ZY arrays. These two arrays, together with the original integer coordinates, are the input

data to the plotter for the zone axis projection.

(5) Parameters for indexing of Kikuchi lines are calculated.

(6) Overlapping labels are rejected.

d. Plotting of Kikuchi and zone projections:

(1) Input data to plotter for a Kikuchi line, registered as X and Y arrays, are calculated using the equation of a circle. However, when the radius of the circle is larger than 3,000 inches, the equation of a straight line is used. Calculation of X and Y arrays are described below.

(2) Complete Kikuchi projection is generated in a DO loop.

(3) Zone projection is completed in another DO loop.

(4) Titles are added to each plot.

The input data to the plotter for plotting of a Kikuchi line are X and Y arrays. Each X-Y pair element represents the X-Y coordinates of a point on the Kikuchi circle with respect to the projected standard basis on the projection plane. To calculate X and Y arrays representing the Kikuchi circle, the radius and the center of the Kikuchi circle must first be determined. The geometry of the standard projection of a Kikuchi line diffracted from plane (hkℓ) is shown in Figure 13 with definitions consistent with those of Figure 12. The center of the Kikuchi circle is C, and CX and CY are the coordinates of C based on the projected standard basis. It can be proved that

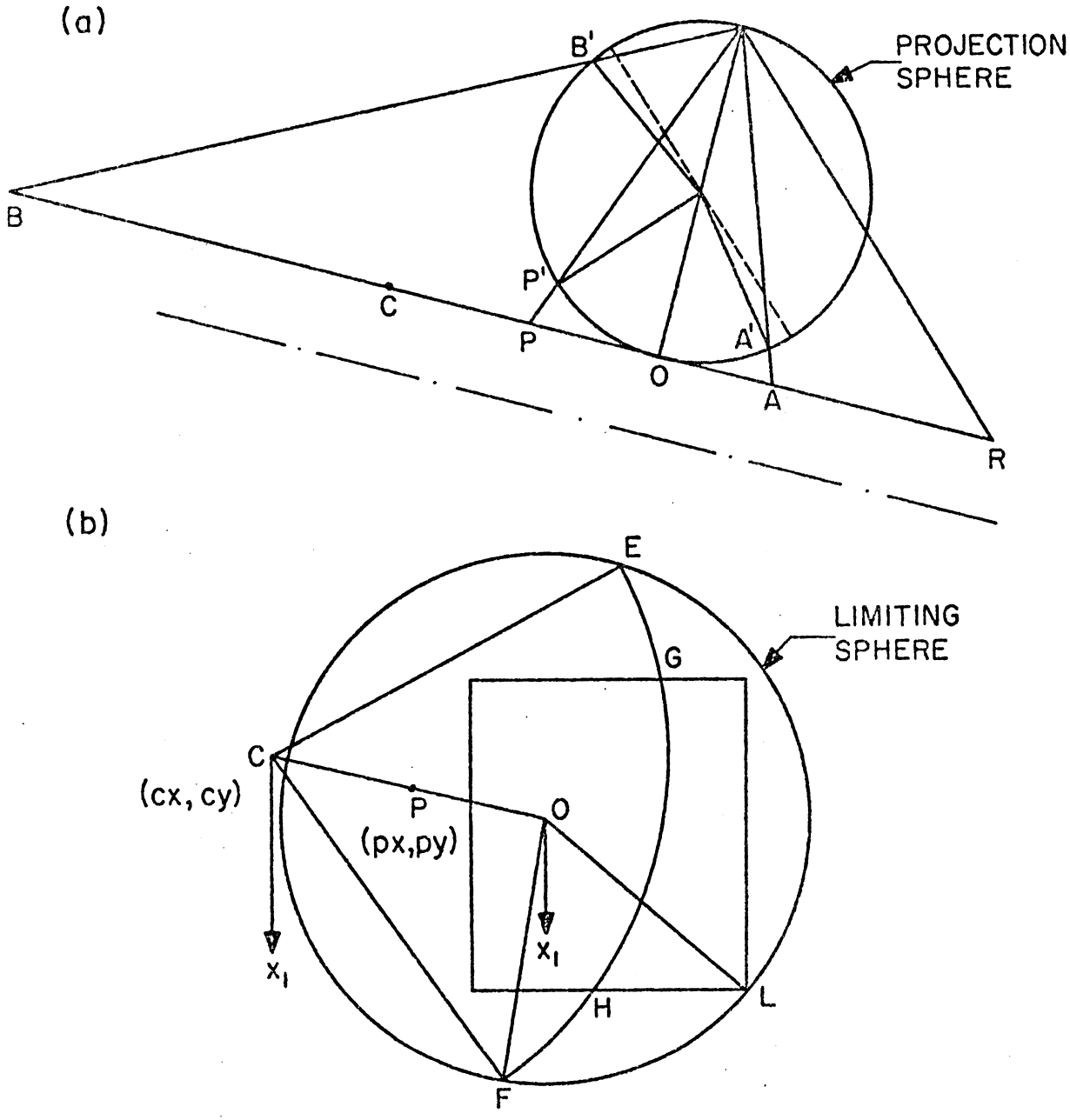

Fig. 13. Geometry for (a) determining the radius and the center of a Kikuchi circle, and (b) determining the starting and the finishing angles of the segment of Kikuchi circle to be considered for plotting. Part (b) is the projection of part (a).

$$\overline{CA} = (\overline{AO} + \overline{BO})/2 \tag{46}$$

$$\overline{CO} = \text{absolute value of } (\overline{AO} - \overline{BO})/2 \tag{47}$$

$$CX = PX\ (\overline{CO}/\overline{PO}) \tag{48a}$$

$$CY = PY\ (\overline{CO}/\overline{PO}) \tag{48b}$$

where $\overline{CA}$ is the radius of Kikuchi circle, $\overline{CO}$ is the distance between origin O and center C, and PX and PY are the X and Y coordinates of the projection of the (hkℓ) plane normal.

In Figure 13(b), the full circle passing through points E, L, and F is a limiting circle. Its radius is equal to $\overline{OR}$ or $\overline{OL}$ whichever is smaller, while $\overline{OL}$ is the distance between the origin and the furtherest corner of the rectangular area. Only the section of Kikuchi circle falling within the limiting circle is to be considered, and only the section confined by the rectangular area is to be plotted. By knowing the location of P on the projection plane, the angle OCX_1 can be determined. The angle OCF, and hence angle OCE, is readily calculated since the three edges of the triangle OCF are all known. Angle FCX_1 and angle ECX_1 are then obtained. Using angle FCX_1 and angle ECX_1 as starting and finishing angles, the X-Y coordinates of a set of points lying along the circular section between E and F are computed. A check is made, and only those points falling inside the plotting area are registered as X, Y arrays and used as inputs to the plotter.

IV. EXPERIMENTAL PROCEDURES

Thin foils of Al - 0.5 at.% Ag alloy were used for transmission electron microscopy examination. The specimens, originally 0.040 inch in thickness, were solution treated at 400°C in an air furnace for 10 hours and then water quenched to room temperature. An aging treatment was then conducted in a silicone oil bath at 160°C for 3000 hours in order to bring out large γ platelets in the crystal. Since the habit planes of these platelets were known to be {111} planes, the platelets were used to test the accuracy of the analysis in determining bicrystal boundary normals.

To prepare thin foils, the specimens were electropolished in a solution of 20% perchloric acid and 80% methyl alcohol, measured by volume. The combined dipping-stirring technique previously used for thinning pure aluminum[34] was employed, except that the solution was kept at much lower temperatures by putting the solution container in a cooling bath containing methyl alcohol and maintained at low temperature by dropping dry ice chips into the bath. The solution temperature was kept at -15°C to -5°C during the initial stages of thinning and was kept at -45°C to -35°C during the final stage of thinning. By keeping the final temperature very low, large uniformly thin areas could be more frequently obtained. To prevent chemical attack by the thinning solution, the specimen was immediately washed and rinsed in water or methanol when it was removed from the thinning solution.

The thin foils were examined on a Siemens Elmiskop 1A electron microscope operated at 100 KV. A Swann biaxial tilting stage with a tilting range of $\pm$ 20° was used. Pole piece no. 2 was used so that more than one

Kikuchi pole could usually be obtained in a pattern. As previously described, the beam stop was introduced at the upper-left corner of each photographic plate to serve as a reference line for both patterns and bright field images. For a pattern where no diffraction spots were observed, it was necessary, before the pattern was taken, to move the specimen to a nearby thin area where spots occurred to make sure that the transmitted beam was located at the center of the final screen. If not obtained previously, a picture was then taken which would allow the center spot to be located in reference to the beam stop. Patterns with sharper Kikuchi lines could be obtained by defocusing the electron beam and using longer exposure time. Sharp and well-defined bright field images were also required, and they were obtained by avoiding strong low-order operating $\bar{g}$ vectors. This minimizes fringe contrast effects which tend to confuse boundary details. The relative rotation between images and pattern was calibrated to an accuracy of $\pm$ 0.5° by means of diffraction from MoO_3 crystals.

Measurement of distances and angles was done using the apparatus shown in Figure 14. Photographs are placed on the central circle under the cross-hairs and taped down. Angles and distances are read using a combination of rotation of the circle and motion of the cross-hairs along the slide. Both the length and angle scales are equipped with verniers. With this apparatus, measurement of lengths can be made to $\pm$ 0.1 mm and angles can be measured to $\pm$ 0.1°.

Bulk calculations were carried out on an IBM 360 computer. Kikuchi line diffraction maps were plotted on a CALCOMP plotter with a maximum paper width of 11 inches.

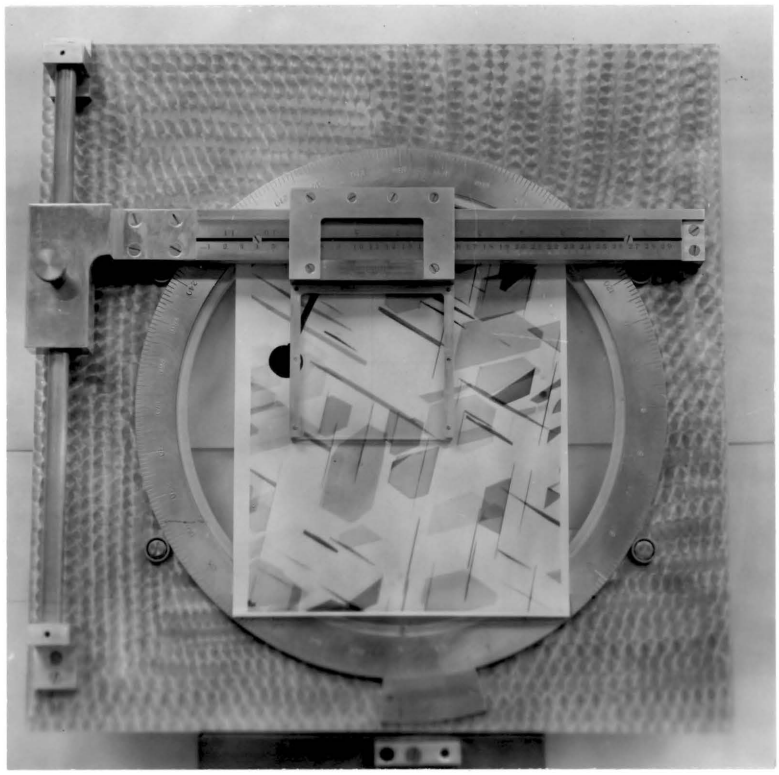

Fig. 14. Apparatus for measurement of distances and angles.

V. RESULTS AND DISCUSSION

In the study of bicrystal characterization, it was found that changes of specimen position during specimen tilting could result in significant errors in certain input parameters used in the calculation of bicrystal variables. The effect of specimen position on magnification, camera length, and angle of image-pattern rotation, was therefore investigated. Also, since the bicrystal parameters were determined using Kikuchi patterns, the inherent accuracy of beam-axis solutions obtained from Kikuchi patterns was analyzed. The inherent accuracy associated with each of the three bicrystal parameters obtained by the analysis developed in the present study were then determined.

In the following, the results of those topics mentioned above are given, and some computer generated line diffraction projections, mainly the Kikuchi projections, are demonstrated.

A. Effect of Specimen Position on Magnification and Diffraction Constants

In transmission electron microscopy, the magnification of images is determined by reading a calibrated magnification indicator which is controlled by varying the intermediate lens current. In analyzing diffraction patterns, camera length is usually assumed to be approximately constant for each pole piece. However, in the present study, it was found that the change in specimen position along the electron-optical axis as a result of specimen tilt, followed by refocusing of the image using the objective lens , could result in a significant error in both magnification and camera length. The error in magnification must be corrected if accurate determination of boundary normals is desired.

Figure 15 shows the effect of specimen position on the setting of the objective lens controllers and on the magnification and camera length for pole piece no. 2 in the Siemens Elmiskop 1A electron microscope. Note that, with this instrument, the coarse objective lens controller may be positioned in terms of "clicks." The number of clicks shown are counted clockwise from zero, the zero position being located at full counter-clockwise rotation. To obtain these diagrams the specimen was put in a fixed specimen stage and was set at the lowest position in the objective focusing range by inserting metal rings and grids above the specimen. The specimen was raised step by step in known intervals. The amount of specimen rise was determined by rotational calibration of the specimen insertion knob with a micrometer. As the specimen was raised from its lowest position, corresponding to the maximum clockwise position of objective controllers, a counter-clockwise rotation of objective controllers was made in order to refocus the image. By setting a constant intermediate lens current, the total amount of specimen rise that could be covered within the entire range of objective focusing was found to be approximately 1.20 mm. This is seen in Figure 15(a), where 16 clicks of the coarse controller plus 50 clicks of the medium controller represents the maximum clockwise rotation of objective controllers. The curve in the figure represents the position of objective controllers when images are brought into best focus. This curve is reproducible and is applicable to all other settings of the intermediate lens, and all the pole pieces. Although the curve of Figure 15(a) is shifted slightly to the left when magnification increases, this shift is insignificant. For example, when meter reading increases from 10,000X to 20,000X the curve

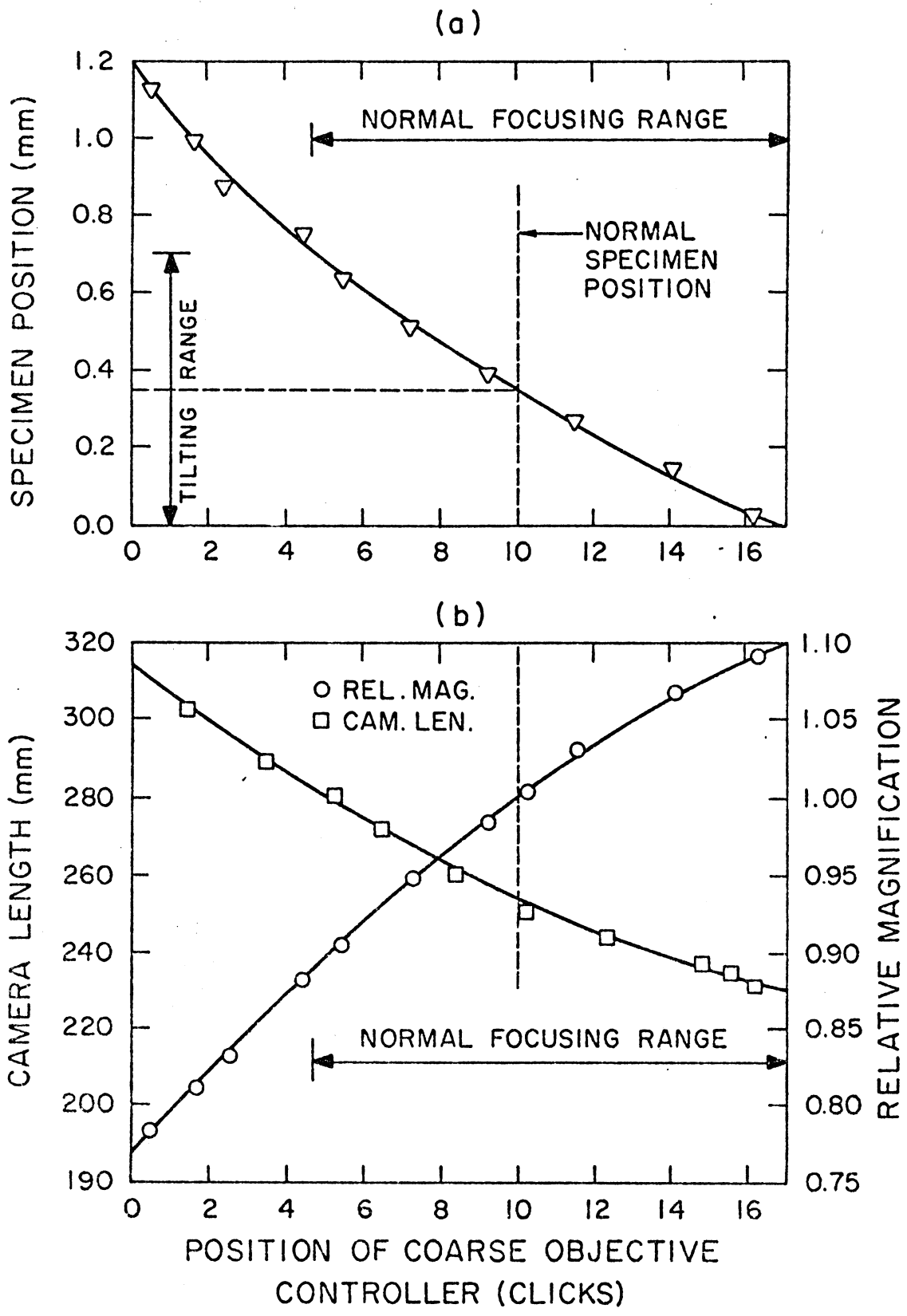

Fig. 15. Relation of (a) specimen position, and (b) camera length and magnification to objective controller position.

is shifted toward the left by only one-fifth of one coarse click. Therefore, the position of the specimen in the objective field can be read with reasonable accuracy from the position of the objective lens controllers once this calibration procedure has been accomplished.

In Figure 15(b) the variation of relative magnification with specimen position is shown. It was obtained using a carbon grating replica which was raised step by step from the lowest position in the objective focusing range. The image was photographed at each step after careful refocusing of the objective lens while the intermediate lens controllers were kept at a meter reading of 6.0. The positions of the objective controllers, both coarse and medium, were recorded for each exposure. Magnifications were calculated and the relative magnifications were determined taking the relative magnification as 1.0 with the specimen at the normal position. It is seen that a total of 30% reduction in magnification results as the specimen is raised by a distance of 1.20 mm while the intermediate lens current is kept constant. This calibration curve can be applied to other intermediate lens settings. Therefore, by noting the positions of the objective controllers for each exposure, a correction for magnification due to specimen tilt can be made. This relative magnification curve is therefore useful in obtaining more accurate magnification for individual micrographs.

In Figure 15(b) the change in camera length resulting from changes of specimen position is also shown. It was obtained from a thin foil of Al-0.5%Ag alloy which was put in a fixed specimen stage and gradually raised as previously described. At each position a Kikuchi pattern was taken following the standard procedures, and the position of the objective

controllers was recorded for each exposure. Bright field images were also taken for some positions. The rotation of the patterns and images with respect to the invariant beam stop introduced at one corner of each photographic plate were measured for other purposes which will be described shortly. The camera lengths shown were calculated from the Kikuchi patterns, assuming that the lattice parameter was not significantly altered in this dilute alloy. It is seen that an increase of camera length from 230 mm to 310 mm, an increase of 35%, results as the specimen is raised by a distance of 1.20 mm. This is in agreement with the observation of Hirsh. et. al., [21] that there is normally a change of about 30%/mm of specimen shift for modern short focus objective lenses, since the diffraction constant λL (λ=wave length, L=camera length) is directly proportional to the focal length of the objective lens for a focused specimen image. They also observed that for the Siemens Elmiskop 1, the value of the diffraction constant decreases by approximately 4%/mm rise in the specimen, provided no lens currents are changed.

It is the change of specimen position during tilting that accounts for the large variation observed in the camera length in diffraction analysis. This shift in specimen position can also cause a significant error in magnification for quantitative analysis. For the Swann biaxial tilting stage used in this study the normal specimen position was found at about the position corresponding to ten coarse clicks, as indicated in the figure, if both the specimen and the supporting grids are unbent. This corresponds to a specimen position of 0.35 mm above the lowest focusing position used in this study. With copper grids 2.3 mm in diameter and a biaxial tilting range of $\pm 20^{o}$, the maximum shift of specimen

position as a result of specimen tilt is calculated to be $\pm$0.35 mm. This results in a normal focusing range starting from the fifth coarse click and continuing to the maximum clockwise position. It is seen from Figure 15(b) that an error of about $\pm$10% in magnification and a variation of camera length from 230 mm to 280 mm can result from micrographs and diffraction patterns taken from the same specimen using various specimen tilts. With the calibration curve, these errors may be corrected if the positions of the objective controllers are recorded for each exposure. If Kikuchi patterns are obtained, the camera length can be accurately calculated without referring the calibration curve.

As mentioned previously, in obtaining the correction curve for camera length the rotations of images and patterns with respect to the invariant beam stop were measured. It was found that both images and patterns rotated identically in the counter-clockwise direction as the specimen was raised. This is shown in Figure 16. A total counter-clockwise rotation of 24^{o} is observed as the specimen is raised through focusing range. The important point here is that the results for image rotation are identical to those for pattern rotation. Consequently, the calibration curve for relative image-pattern rotation is not effected by the change of specimen position.

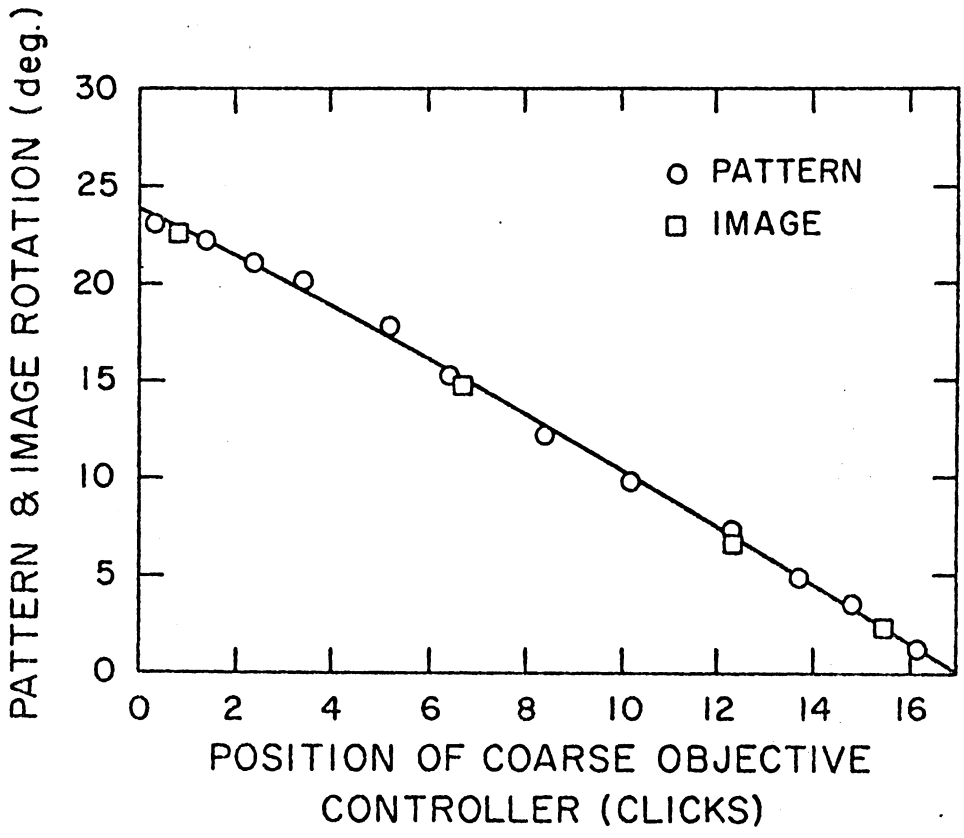

Fig. 16. Relation between the position of the coarse objective controller and the image and pattern rotations. Both image and pattern rotate counter-clockwise as the objective controller is rotated clockwise.

B. Beam Axis Solution From Kikuchi Patterns

The three-pole solution [3] of Kikuchi patterns has been the most generally used technique in the determination of precise crystal orientation in transmission electron microscopy. In some cases, the two-pole solution of Otte et al. [4] has also been employed. In the present study, some other alternate solutions were investigated. The inherent accuracy associated with each solution was determined.

When three or more Kikuchi poles are recognizable or can be inferred from a diffraction pattern, the crystal orientation, i.e., the direction of the transmitted electron beam based on the crystal coordinate axes, may be determined from a three-pole solution (3-P). A schematic example is given in Figure 17(a). Three Kikuchi poles (K-poles) $[h_i k_i \ell_i]$, i = 1,2,3, are indexed and three simultaneous equations, each involving a cosine function, are formulated. The three pole equations are

$$\bar{P}_i \cdot \bar{B} = \cos \theta_i, \qquad i = 1,2,3$$

or

$$h_i h + k_i k + \ell_i \ell = L/\sqrt{L^2 + d_i^2}, \qquad i = 1,2,3 \qquad (49)$$

where $\bar{P}_i = [h_i k_i \ell_i]$ = a unit vector along the ith pole axis,

$\bar{B} = [hk\ell]$ = a unit vector along the transmitted beam axis,

θ_i = angle between $\bar{P}_i$ and $\bar{B}$, generally less than 10^o,

d_i = distance between the transmitted spot and the center of ith pole, and

L = effective camera length, i.e., the camera length which

results if the photograph is assumed to be the final screen of the microscope.

In the present study it was found that the beam axis can also be solved by a "three-normal" solution (3-N), provided that three independent Kikuchi pairs which do not share the same Kikuchi pole are observed on the pattern. Kikuchi lines must first be indexed unambiguously and three simultaneous equations, each involving a sine function, are formulated. As is seen from Figure 17(a) and (b), the three normal equations for the 3-N solution are

$$\bar{N}_i \cdot \bar{B} = \cos(90^o - \phi_i) = \sin \phi_i , \qquad i = 1,2,3 \qquad (50a)$$

or

$$H_i h + K_i k + L_i \ell = t_i \Big/ \sqrt{L^2 + t_i^2} , \qquad i = 1,2,3 \qquad (50b)$$

where $\bar{B}$ and L are as previously defined, and

$\bar{N}_i$ = $[H_i K_i L_i]$ = a unit vector along the normal of $(H_i K_i L_i)$ plane,

ϕ_i = angle between $\bar{N}_i$ and $\bar{B}$, and

t_i = the perpendicular distance between the transmitted spot and the trace of the $(H_i K_i L_i)$ plane.

Only positive values of the square roots in both equations (49b) and (50b) are used in calculations. It is to be noted that for each of the three normal equations, the indices of the Kikuchi line (K-line) which is closer to the transmitted spot, i.e., the dark line of the pair, is used to establish the equation. For the case where the trace line passes through the transmitted spot, indices of either K-line of the pair can be used.

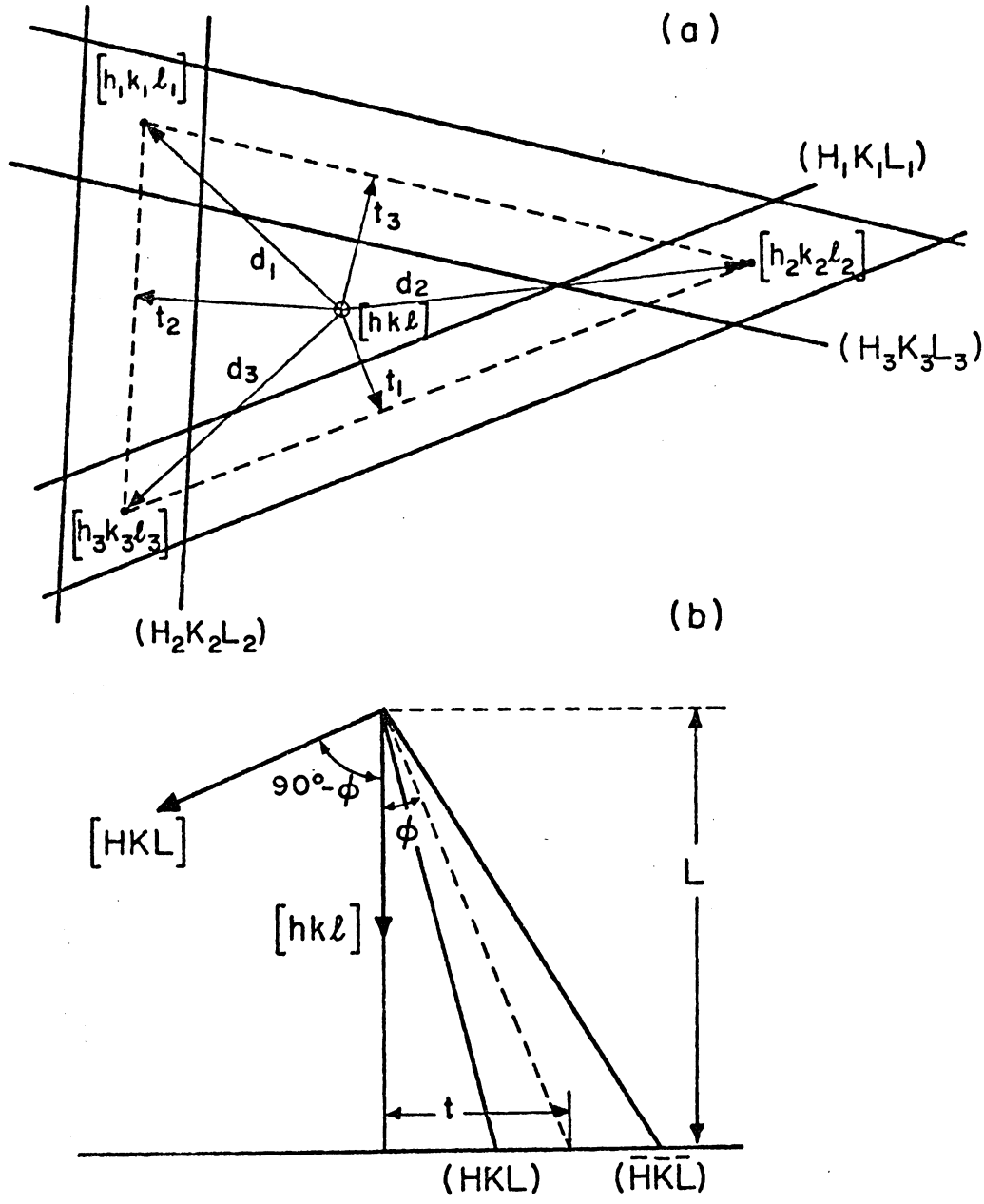

Fig. 17. (a) Schematic Kikuchi pattern showing the parameters to be measured for beam axis solution. (b) Diagram illustrating the formulation of normal equations using the trace distance t.

If this is done, the angles $(90^{o} - \phi_i)$ are always less than or equal to 90^{o} so that negative dot products can be rejected. It should also be pointed out that two possible beam axis solutions will be obtained from a set of three equations formulated from three K-pairs which share the same K-pole, since one of the three equations is a dependent equation. This arises from the fact that the three normal vectors $[H_1K_1L_1]$, $[H_2K_2L_2]$ and $[H_3K_3L_3]$ are co-planar. This can also be understood from the result that the determinant of the coefficients of the three equations from equation (50b) is always equal to zero when the three vectors are co-planar.

To determine the three unknowns h, k, and ℓ from 3-P or 3-N solutions, the effective camera length, L, must first be known. It can be determined either from the distance of Kikuchi pole separation, or from the separation of Kikuchi pairs. By having L determined, the coordinates of the unit vector $[hk\ell]$ can be solved. However, if the input L is not the correct effective camera length, the length of the resultant vector $|[hk\ell]|$, i.e., the S value ($S = h^2 + k^2 + \ell^2$), will not be equal to unity, and significant error may occur in the solution. Therefore, the true L can be calculated graphically or iteratively by changing L until S reaches the value of unity.

The beam axis may also be solved from three equations consisting of either (1) two pole equations and one normal equation (2-P/1-N) or (2) one pole equation and two normal equation (1-P/2-N). For example, the 2-P/1-N solution can be used when two or more K-poles are recognizable on the pattern, and the 1-P/2-N solution may be employed when only one K-pole is

observed. The latter approach is essentially the solution given by Otte et al. [4], in which it is assumed that the K-pairs, not individual K-lines, are indexed. Since two sets of indices, (HKL) and $(\bar{H}\bar{K}\bar{L})$, can be assigned to a K-pair, the ambiguity leads to two possible solutions. Consequently, two K-poles are required if the determination is to be unique. Also by concluding that the third equation, the pole equation, was dependent and gave no further information, Otte et al. followed a complicated procedure to calculate the two possible solutions from two normal equations and used the third one to check the accuracy of the solutions. Careful analysis reveals that the three equations are all independent since the two normals and the pole axis are not co-planar. Hence the two possible solutions may be obtained in a straight forward manner by changing signs of the indices of a K-pair. If individual K-lines which construct the single K-pole are indexed unambiguously and proper K-lines are used to formulate equations, a unique solution can be obtained from the three equations. In fact, for those K-poles with their multiplicity factors being greater than the number of the degree of crystal symmetry, e.g., ⟨123⟩ poles in cubic crystals, the pattern can be indexed uniquely even when only one pole is observed. For those poles with their multiplicity factor being equal or smaller than the number of the degree of crystal symmetry, K-lines are required other than those sharing the K-pole in order to index the pattern properly. These extra lines are usually observed together with the single pole. With the help of properly indexed Kikuchi projections, indexing of the pattern can usually be carried out without difficulty.

In addition, the beam axis can also be obtained from the one pole matrix solution (1-P/matrix) given in equation (29). Again, if the pattern can be indexed unambiguously, a unique transformation matrix and hence a unique solution may be determined. The advantage of this matrix solution is that all the vectors, not only the transmitted beam, based on a reference coordinate frame selected from the pattern can be transferred to the crystal basis. Therefore it is this transformation matrix that completely describes the crystal orientation based on the observed pattern.

Thus far, five methods of beam axis solution have been mentioned. They are the 3-P solution, the 3-N solution, the 2-P/1-N solution, the 1-P/2-N solution, and the 1-P/matrix solution. It has been reported that the beam axis can be determined from the Kikuchi pattern to a possible accuracy of $\pm$ 0.1^{o} under optimum conditions [4,21]. The fact that the observed patterns are somewhat distorted and that the assumed camera length may not be the true value can add some additional uncertainty to the solution. The pattern distortion mainly comes from EM lens distortion, foil bending, and distortion of print paper.

One way to check the inherent accuracy of the various methods of beam axis solution is to compare for the same pattern the solutions of the same method obtained from different input data, including the use of various effective camera lengths. Figure 18 is a magnified print of a typical diffraction pattern taken from an aged Al-0.5 at.% Ag crystal using pole piece no. 2. To perform the analysis of inherent accuracy, nine K-poles were selected, as is seen in the figure. They were readily indexed with

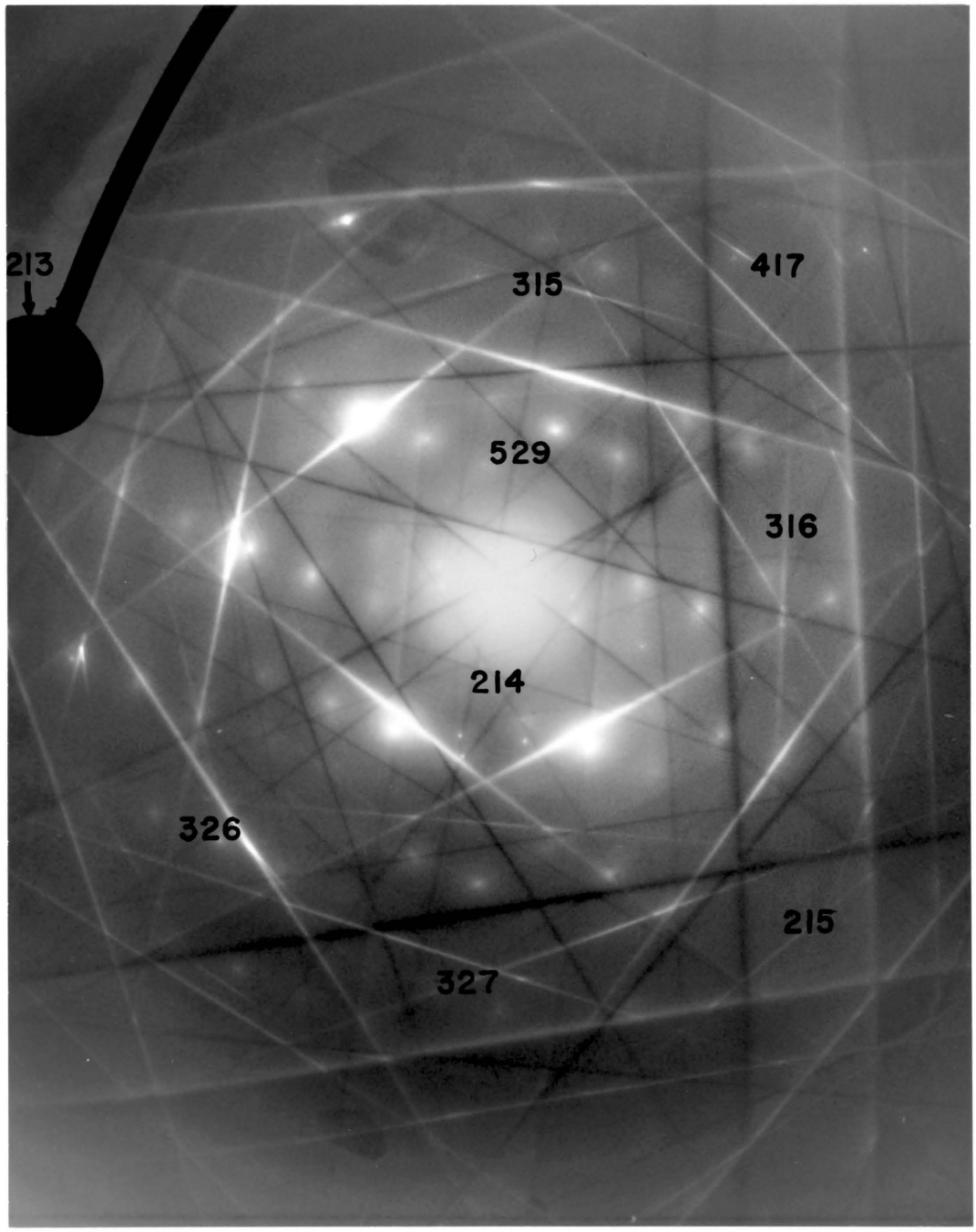

Fig. 18. Kikuchi pattern taken from aged Al-0.5 at .% Ag crystal. Nine indexed Kikuchi poles shown on this pattern were used to calculate the beam axis.

the help of Kikuchi projections. K-lines were indexed by taking cross products between poles. From these nine K-poles and various K-lines, ten 3-P solutions, twelve 3-N solutions, thirteen 1-P/2-N solutions, and twelve 1-P/matrix solutions were obtained for each input effective camera length. For each approach, the first solution was obtained from K-pole or poles and/or K-line or lines which were closest to the transmitted spot. It is assumed that this is the most accurate solution for the method employed if the true effective camera length is used. For a given L, all the solutions were compared with the most accurate solution, and the angular deviations were taken as the inherent errors associated with the solutions. The same calculations were repeated for different values of L. The effect of input L on the various methods of solution was thus determined. It should be mentioned that measurement of input parameters was done on a 5" x 10" print using an ordinary ruler. The calculations were carried out by using a FORTRAN computer program written in double precision statements. The results are presented in the following paragraphs.

In this study the true effective camera length was determined graphically from either 3-P or 3-N solution by calculating the S value for input L varying from 75 cm to 83 cm. The S value of the 3-P solution is plotted against input L in Figure 19(a). To prevent overcrowding, only five of the ten curves obtained are plotted. These are plotted as dashed lines in the figure. The solid line is the average of the ten S curves. The S curves of the 3-N solution all run parallel to each other and are all confined within the band indicated by the dashed lines shown in Figure 19(b). The solid line is the average of twelve S curves.

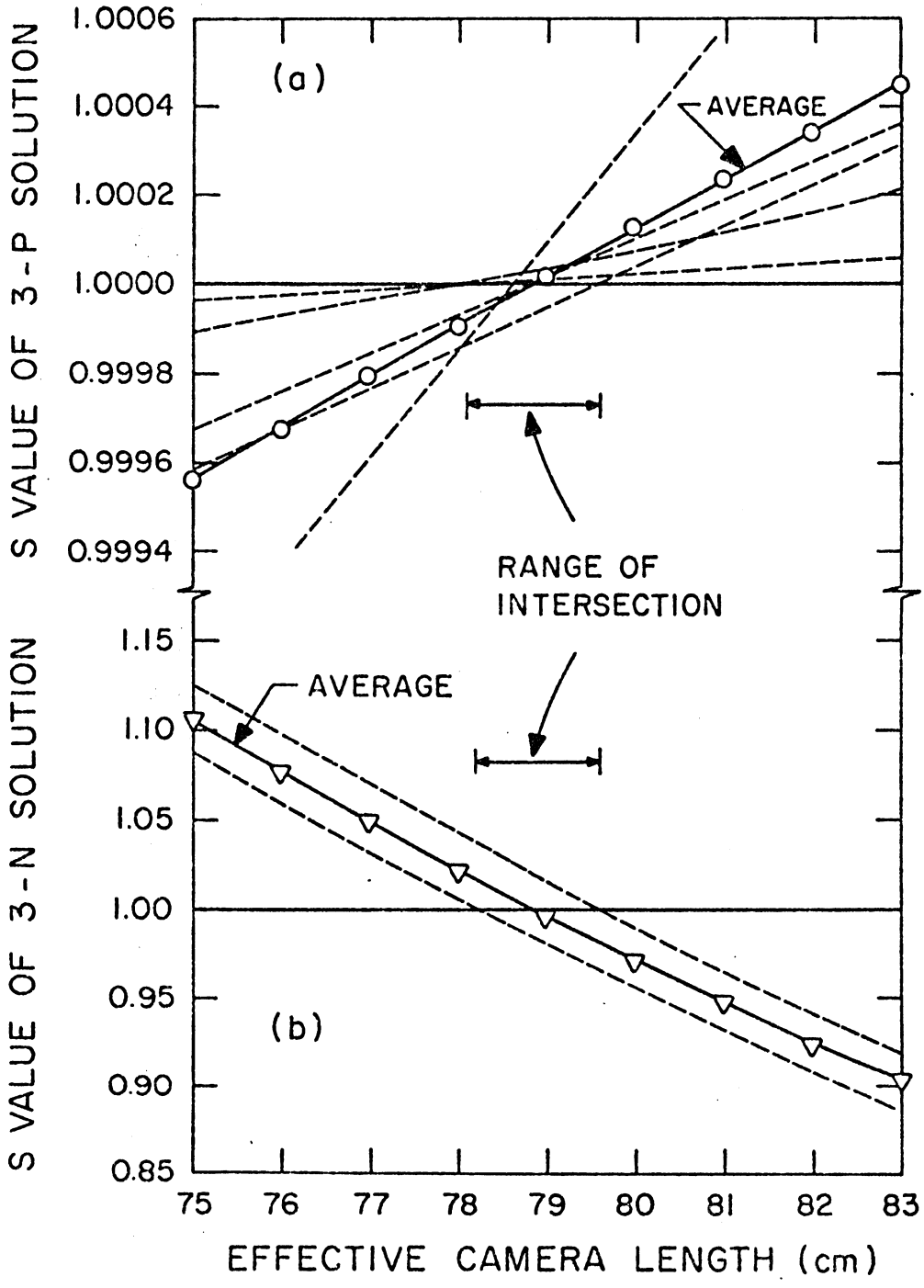

Fig. 19. Resultant S value, where $S = h^2 + k^2 + \ell^2$, as a function of assumed effective camera length.

In spite of the difference in the scale of ordinates, it is seen that the average S curves of both 3-P and 3-N solutions intersect the horizontal S = 1 line at the point where L = 78.85 cm., which is believed to be the true effective camera length. Theoretically, all the S curves for both 3-P and 3-N methods should intersect the S = 1 line at the point of true L. However, due to pattern distortion and the possible errors involved in input measurements, S curves are seen to intersect the unity line within a range of effective camera length. Therefore, for the example in Figure 18, the true effective camera length may be determined from this S curve intersection approach, and the breadth of the range of intersections shows that the camera length can be measured to $\pm$ 1% accuracy. The reasonably large scale of ordinate in Figure 19(b) indicates that this approach can be carried out manually when the 3-N method is employed.

The effective camera length for the pattern shown in Figure 18 was also calculated using distance of K-pair separation and distance of K-pole separation. Ten L values were determined from K-pair separation using the equation, $rd = \lambda L$. They were found to vary from 72.83 cm. to 75.90 cm., with an average of 74.85 cm. Another ten L values calculated from K-pole separation were found to range from 77.57 cm. to 79.31 cm., with an average of 78.48 cm. By taking 78.85 cm. as true L, it is seen that L can be determined to within 5-7% using the distance between a K-pair, and to within 1-2% from the distance between two arbitrary K-poles. Generally, L can be calculated to within 1% from the distance between two K-poles which are relatively close to the transmitted spot. The larger error associated with the use of K-pair separation is believed to be due to the uncertainty

of electron wave length λ, lattice parameter, and the potential parallax errors resulting from projection geometry.

For a given input L, the accuracy inherent to each of the four methods selected for beam axis analysis was determined by comparing all the solutions of the same method with the most accurate solution calculated using L = 78.85 cm. The maximum angular deviation was interpreted as the possible error associated with the particular method employed. The same calculations were carried out for different L values ranging from 75 cm to 83 cm. The results are tabulated in Table B-1 through Table B-4 in the Appendix. The maximum and average angular deviations are plotted vs. the input L in Figure 20. It is seen that the 3-N solution is the most accurate one and is nearly independent of input L within the range of camera length concerned. The inherent accuracy is within $\pm$ 0.08°. While for the other three solutions (as well as 2-P/1-N solutions), in which at least one pole equation is used, the maximum and average angular divergencies all become minimum at about the true L, and increase as the error in input L increases. Based on the fact that the effective camera length can be determined to within 5-7% accuracy from K-pair separation and to within 1% accuracy from K-pole separation, it is seen that for those solutions with at least one pole equation applied, the beam axis can be determined to an accuracy of $\pm$ 0.4° if distance between K-pair is used to calculate L, and to $\pm$ 0.15° if distance between K-poles is used in calculating L. In general, if the input measurements are obtained from Kikuchi pole or poles and/or Kikuchi line or lines which are relatively closer to the transmitted spot, the beam axis can be determined to $\pm$ 0.05° from the

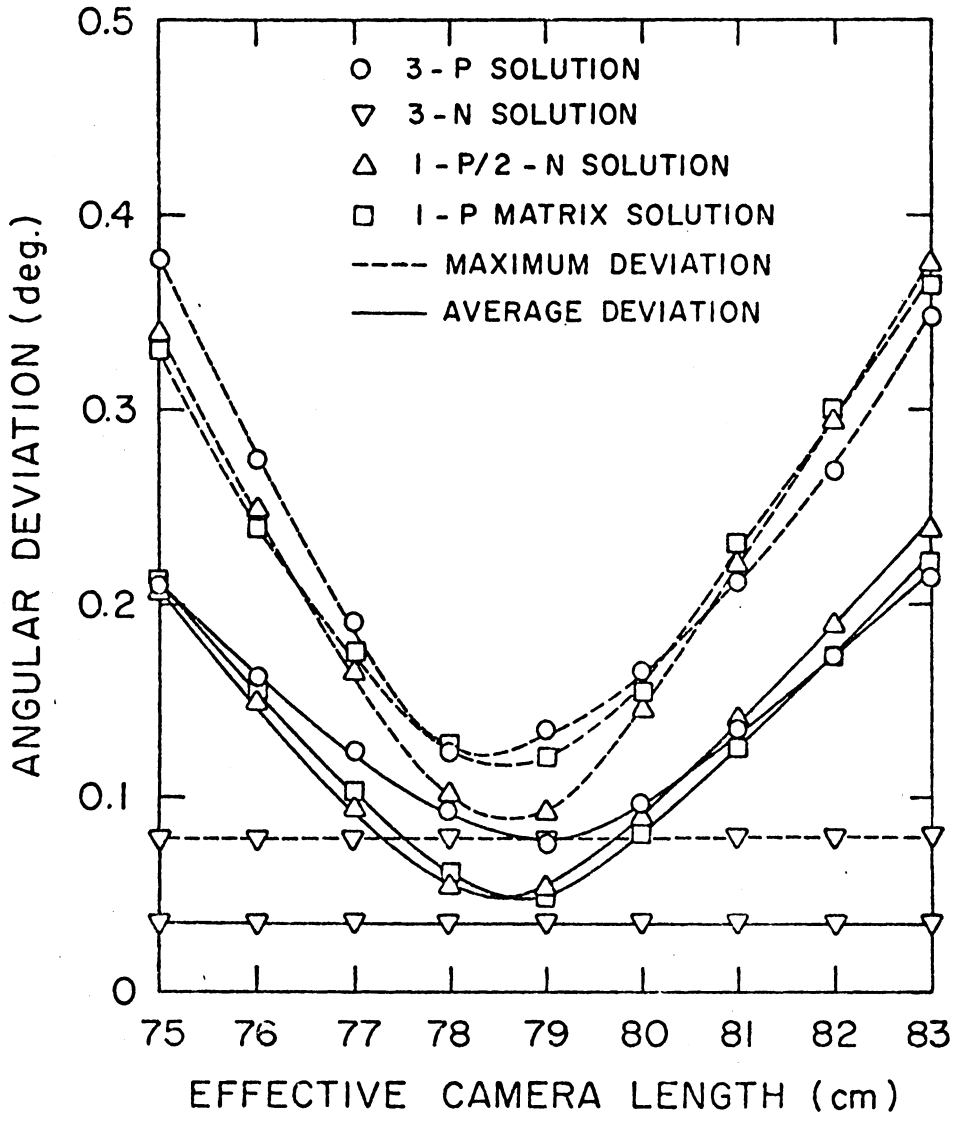

Fig. 20. Angular divergency of various beam axis solutions as compared with the most accurate solution calculated using L = 78.85 cm.

3-N solution, and to $\pm$ 0.1° from the other solutions when the effective camera length is obtained using the Kikuchi pole separation. Therefore, the 3-N solution is suggested whenever three independent K-pairs are recognizable on the pattern. This solution is strikingly insensitive to variations of effective camera length. In fact, the true camera length can be determined graphically or iteratively by calculating the resultant S and adjusting L to produce S = 1.

In Figure 21 the average angular deviations from 3-P, 1-P/2-N, and 3-N solutions are again plotted against a wide range of assumed L varying from 1 cm to 1000 cm. It is interesting to note the small angular divergency of the 3-N solution over an extremely wide range of input L. With this solution, the average angular deviation stays almost constant at about 0.04° for all the values of L greater than 20 cm. The divergency starts to increase when L becomes smaller than 20 cm, and finally reaches a value of 1.653° for L = 1 cm. On the other hand, the average angular divergency of the 3-P and 1-P/2-N solutions increase when input L deviates from its true value, especially when L is small. In Figure 22, the average S values for 3-N and 3-P solutions are again plotted against the same range of L. For 3-N solutions, S is approximately proportional to $1/L^2$ when $L \gg t_i$. Therefore the S value approaches zero at large L, and increases rapidly at small L. For 3-P solutions the S value approaches 1.00575 at large L and has an irregular shape at small L.

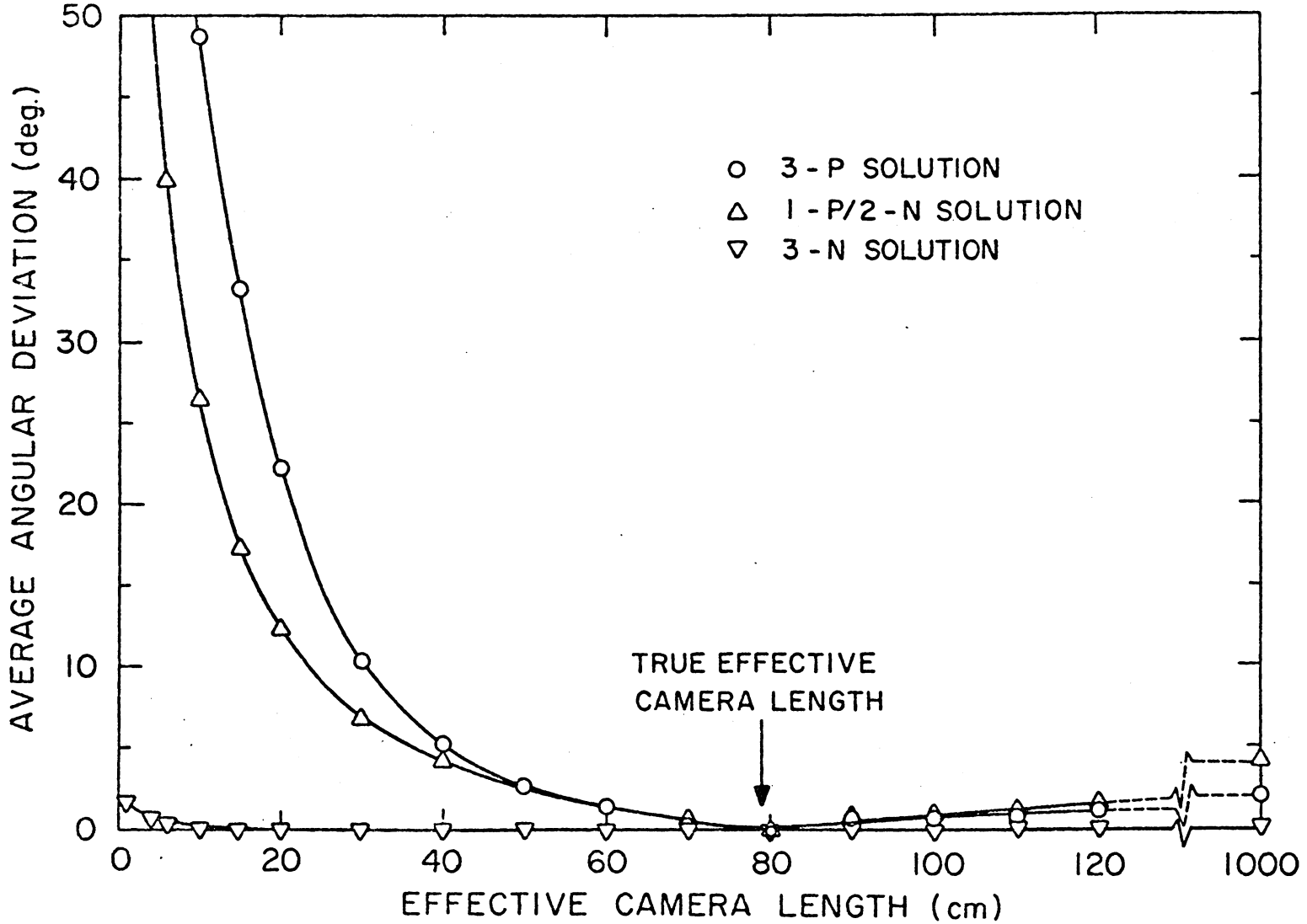

Fig. 21. Dependence of angular divergency of various beam axis solutions on the assumed effective camera length.

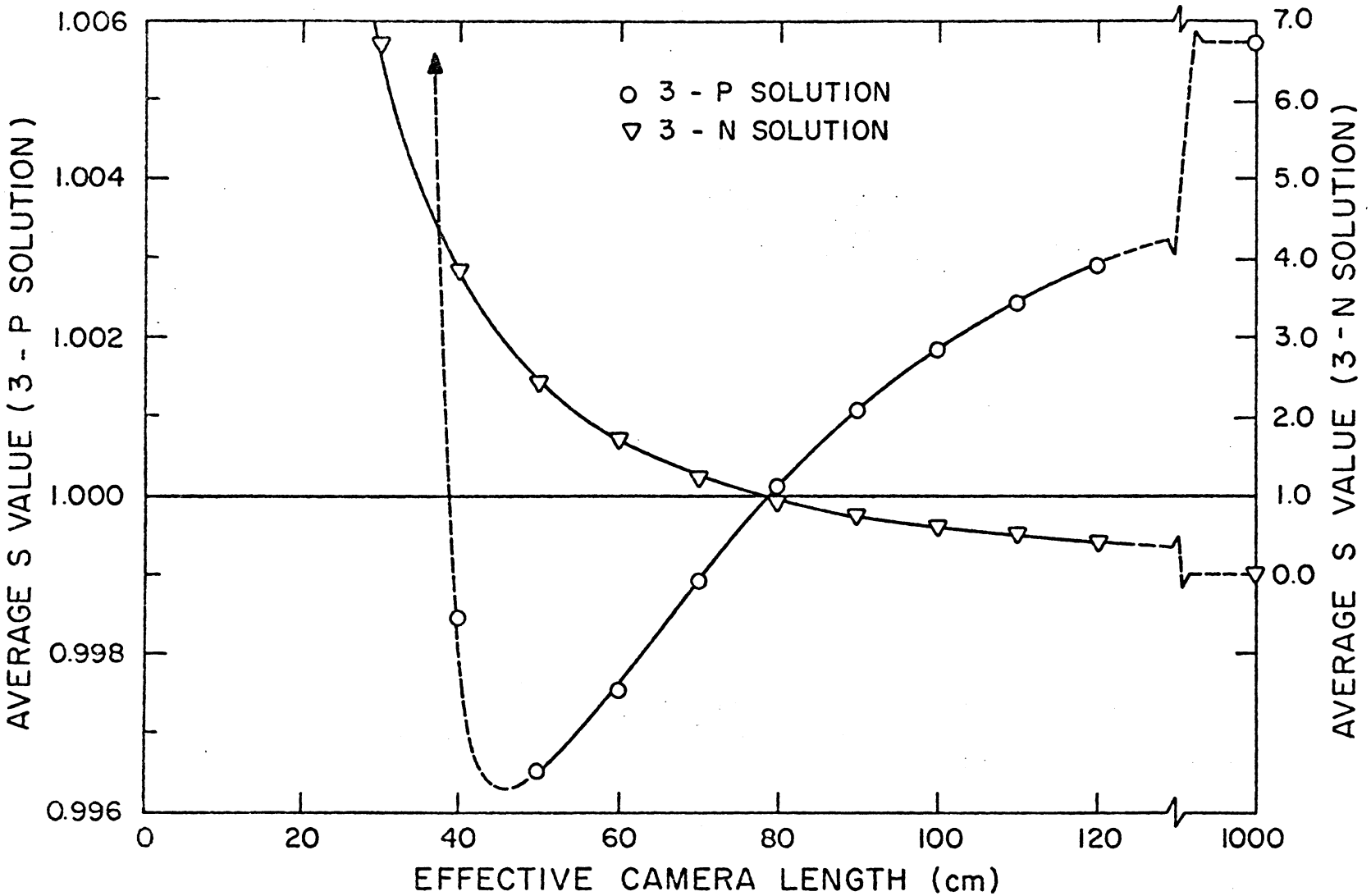

Fig. 22. Resultant S value as a function of the assumed effective camera length.

C. Bicrystal Characterization

1. High Angle Misorientation

Figure 23 shows two Kikuchi patterns, each taken from one of two neighboring grains. Two rotation matrices, [CR1] and [CR2], each associated with one of the two patterns can be formulated according to equation (27). A misorientation matrix specifying the orientation relationship between the two grains is obtained from equation (31). The axis and angle of misorientation can then be calculated from the misorientation matrices using equations (15) and (16).

One way to check the inherent accuracy of misorientation parameters is to formulate the matrix [CR1] from one pattern using the same input pole and axis, i.e., Zp and Xp of the pattern frame, and formulate the second matrix [CR2] from the other pattern by using different sets of input poles and axes. The angular deviations of various solutions as compared with the most accurate solution are interpreted to be related to the accuracy associated with the determination of misorientation parameters.

On two 8" x 10" prints corresponding to the two patterns shown in Figure 23, the camera length for pattern (a) was found to be 77.70 cm and that of pattern (b) was 77.67 cm, both representing the averages of three camera lengths calculated from pole separations. The matrix [CR1] associated with pattern (a) was formulated with camera length=77.7 cm and Zp and Xp equal to [123], and [$\bar{5}$11], respectively. On pattern (b), six poles were selected to formulate eleven [CR2] matrices for three different camera lengths, 76 cm, 78 cm, and 80 cm. For each camera length, eleven

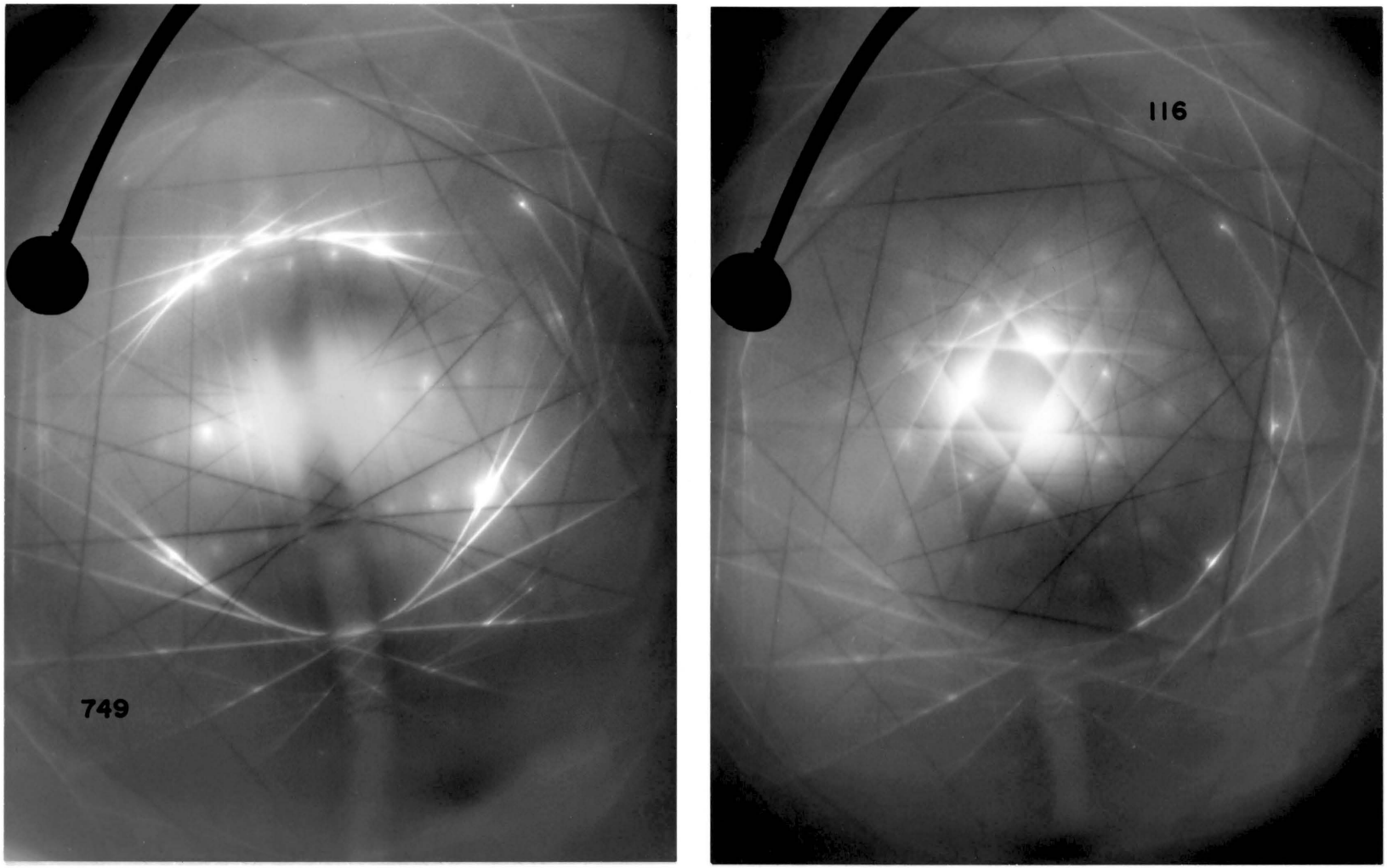

(a) (b)

Fig. 23. Two Kikuchi patterns from Al-0.5 at.% Ag, each taken from one of two neighboring crystals.

misorientation angle-axis pairs were obtained. Among them the first angle-axis pair is assumed to be the most accurate solution, since it is obtained from the K-pole closest to the transmitted beam. The misorientation angles and the angular deviations in misorientation axis as compared with the first solution were obtained and are listed in Table I.

As is seen from Table I, the angle-axis pairs vary slightly with the change of camera length. The possible error, as taken from maximum deviation, is within $\pm 0.5^{\circ}$ for angle of misorientation, and is within $\pm 0.2^{\circ}$ for axis of misorientation.

It is of interest to note that on each pattern the center region shows the Kikuchi pattern of the crystal from which the pattern was taken, and the outer region shows the Kikuchi pattern of the neighboring crystal. For example, the [116] pole of pattern (b) is observed on the outer area of pattern (a), and the [749] pole of pattern (a) can be observed on pattern (b). This halo effect has been observed for most of the patterns taken from an area near the crystal boundaries. It is believed that the Kikuchi pattern observed at the outer region of the pattern is the result of double diffraction from the neighboring grain. Therefore, any attempt to determine the misorientation parameters from a single pattern with this halo effect may not be proper, since the major electron beam giving rise to the Kikuchi pattern at the center region would not be parallel to that contributing to the pattern shown at the outer region. Such a calculation, however, was made using pattern (a) alone. The inputs for [CR1] were the same as those used previously, while those for [CR2] were the [116] pole and [15$\bar{1}$] axis measured on pattern (a). The results calculated for three different camera lengths are also listed on the last

Table I. Misorientation Angle and Angular Deviation in Misorientation Axis for High-Angle Bicrystal (Fig. 23)

Input Axis		Misorientation Angle (Degrees) Effective Camera Length			Deviation in Misorientation Axis (Degrees) Effective Camera Length			Misorientation Axis Effective Camera Length		
Z_p	X_p	76 cm	78 cm	80 cm	76 cm	78 cm	80 cm	76 cm	78 cm	80 cm
[114]	[$\bar{1}\bar{3}$1]	128.96	128.96	128.97				1.0000 1.2928 2.6930	1.0000 1.2917 2.6916	1.0000 1.2906 2.6904
[329]	[$\bar{1}\bar{3}$1]	128.95	128.98	129.00	0.028	0.052	0.110			
[127]	[$\bar{1}\bar{3}$1]	128.98	128.96	128.93	0.082	0.044	0.107			
[239]	[3$\bar{5}$1]	128.52	128.51	128.49	0.101	0.040	0.044			
[127]	[3$\bar{5}$1]	128.53	128.51	128.49	0.124	0.044	0.052			
[127]	[51$\bar{1}$]	129.23	129.20	129.16	0.082	0.071	0.136			
[116]	[51$\bar{1}$]	129.25	129.25	129.26	0.124	0.059	0.084			
[116]	[15$\bar{1}$]	128.79	128.78	128.77	0.190	0.141	0.144			
[217]	[15$\bar{1}$]	128.76	128.79	129.83	0.117	0.168	0.233			
[217]	[$\bar{5}$31]	129.31	129.32	129.34	0.044	0.099	0.174			
[329]	[$\bar{5}$31]	129.27	129.30	129.32	0.069	0.028	0.077			
[116]	[15$\bar{1}$]*	128.51	128.50	128.48	0.226	0.204	0.219			
Max. Deviation		0.44	0.45	0.48	0.190	0.168	0.233			

*Results obtained from the single pattern with halo effect shown in Figure 23(a).

row in Table I. It is seen that the misorientation angle and the deviation in misorientation axis thus obtained are different by about 0.5^{o} and 0.2^{o} respectively from the averages of the other solutions.

The misorientation angle and axis can be determined from ordinary stereographic procedures using a stereogram. On a stereogram of 30 cm in diameter, the process of locating each of the two beam axes solved from Kikuchi patterns may introduce an error of $\pm 0.5^{o}$ [14]. The inaccuracy in plotting poles and traces and in manipulating the stereogram, together with the uncertainty inherent to the beam axis solution will introduce additional errors in the final results. With all these sources of uncertainty, the possible errors in the misorientation angle and axis thus determined may be well over $\pm 1^{o}$. The matrix approach developed in the present study therefore provides misorientation angle and axis with considerably improved accuracy over stereographic techniques.

The misorientation angle-axis pairs which result in a high density of coincidence lattice sites have been calculated and tabulated [10,11]. Such tables have been frequently used as sources in finding the density of coincidence sites for the bicrystal under investigation, but these tables do not list all the degeneracy angle-axis pairs for a specific misorientation relationship. In the present study, however, once a misorientation matrix is determined, the other 23 degeneracy matrices and hence the degeneracy angle-axis pairs for cubic crystals are readily obtained from equations (32), (15), and (16), and all 24 pairs are listed in the computer output. Since all the 24 degeneracy angle-axis pairs are known, a comparison with the reference tables is easily accomplished.

2. Low Angle Misorientation

The misfit angle of low-angle bicrystal boundaries, usually called subboundaries, is usually less than one or two degrees. The determination of misorientation parameters in subboundaries thus requires more careful measurement. Fortunately, the main sources of error in measurement are eliminated since only one pattern is needed to formulate the misorientation matrix. Therefore the main sources of error come from the location of the true pole center and the measurement of twist angle γ from a pair of identical "split" Kikuchi lines.

The pattern taken from an area across a subgrain boundary of pure aluminum, as is seen in Figure 7, was used to evaluate the inherent accuracy of misorientation parameters. On an enlarged print, a camera length of 155.0 cm was obtained from distance of pole separation. The twist angle γ was measured to be 0.46°. This angle can be measured to within $\pm 0.05^{\circ}$ accuracy on the enlarged print. A circular area of uncertainty, about 1.5 mm in diameter, is usually involved in locating each pole center. Misorientation parameters were computed by introducing the possible combinations of the major sources of errors, namely, the uncertainty in locating the pole center and the measurement of twist angle γ. The results calculated for the [132] pole using three different camera lengths are interpreted as approximating the inherent accuracy associated with the misorientation parameters. It is seen from Table II that the inherent accuracy is within $\pm 0.07^{\circ}$ for angle of misorientation, and within $\pm 3.8^{\circ}$ for axis of misorientation. They are rather insensitive to the input camera length.

Koo has demonstrated a quantitative method for the study of orientation relationship between subgrains by dark-field transmission electron

Table II. Misorientation Angle and Angular Deviation in Misorientation Axis for Low-Angle Bicrystal (Fig. 7)

Input Axis		Misorientation Angle (Degree) Effective Camera Length			Deviation in Misorientation Axis (Degree) Effective Camera Length			Misorientation Axis Effective Camera Length		
Z_p	X_p	151 cm.	155 cm.	159 cm.	151 cm.	155 cm.	159 cm.	151 cm.	155 cm.	159 cm.
[132]	[$\bar{4}$02]	1.168	1.144	1.119				1.0000 0.8800 0.6938	1.0000 0.8887 0.6827	1.0000 0.8974 0.6716
"	"	1.151	1.126	1.101	2.330	2.374	2.417			
"	"	1.187	1.162	1.140	2.261	2.300	2.337			
"	"	1.119	1.096	1.073	1.528	1.540	1.548			
"	"	1.102	1.078	1.054	1.666	1.684	1.701			
"	"	1.140	1.116	1.094	3.610	3.663	3.713			
"	"	1.217	1.191	1.166	1.432	1.444	1.453			
"	"	1.201	1.174	1.148	3.429	3.487	3.543			
"	"	1.235	1.209	1.184	1.518	1.533	1.547			
"	"	1.151	1.126	1.102	2.667	2.657	2.647			
"	"	1.133	1.108	1.085	3.359	3.372	3.386			
"	"	1.168	1.145	1.123	3.704	3.729	3.753			
"	"	1.190	1.163	1.137	2.580	2.571	2.563			
"	"	1.172	1.145	1.120	3.694	3.726	3.758			
"	"	1.208	1.182	1.158	3.153	3.163	3.172			
Max. Deviation		0.067	0.066	0.065	3.704	3.729	3.758			

microscopy [15]. In his study, the twist angle about the electron beam axis, i.e., the angle γ, was assumed to be zero, since the error introduced by this assumption was only about 1% of the misorientation and was negligibly small for the case where the twist angle was $\leq 1^{o}$. It has been found that this assumption is not necessary true. In Figure 7, for example, the misorientation angle and axis were calculated using different values of γ ranging from 0^{o} to 1^{o}. When γ is equal to 0^{o}, 0.46^{o}, and 1^{o}, the corresponding misorientation angles are 1.056^{o}, 1.144^{o}, and 1.432^{o}. For the measured γ of 0.46^{o}, the assumption of $\gamma=0$ introduces an error of 0.088^{o} in misfit angle and an error of 23.76^{o} in axis of misfit. For $\gamma=1^{o}$, the assumption introduces an error of 0.367^{o} in angle of misfit and an error of 44.35^{o} in misfit axis. In addition to the possible high percentage error in misfit angle, a wide variation in misfit axis results by neglecting the twist angle γ . It is concluded that the dark-field tilting technique is of doubtful value in measurement of subboundary misorientation parameters.

3. Boundary Normals

When it is not possible to tilt the specimen to bring the boundary plane parallel to the electron beam, the analysis given in Section III-B-4 and 5 can be used to determine a boundary normal without knowledge of the foil thickness and foil inclination. Two vectors lying on the boundary plane are selected. Their coordinates are determined using a rotation matrix which represents the actual specimen tilt inside the microscope. The boundary normal is then obtained by taking the cross product of the two vectors.

To check the accuracy of boundary normals determined from the present analysis, a thin foil of Al-0.5 at.%Ag alloy was examined after an aging treatment in a silicone oil bath at 160° for 3000 hours. Large γ' platelets were observed. The habit planes for γ' precipitates are {111} planes. The normals of the platelets were calculated as described above, and the angular deviations from the corresponding {111} type planes are interpreted to be the inherent accuracy associated with the calculation of boundary normals.

For higher accuracy, a larger angle of specimen tilt is desired. The Swann biaxial tilting stage can provide a maximum tilt of about 40°. As mentioned previously, if the observed spot is close to the edge of the supporting copper grids, a possible variation of 20% in magnification could occur. The correction factor can be obtained from the calibration curve given in Figure 15(b), provided that position of objective controllers are recorded for each exposure.

Figure 24 shows two Kikuchi patterns taken before and after specimen tilt, with the beam stop fixed in each for reference. A rotation matrix specifying the true rotation can be formulated from these two patterns. Once pattern (a) is indexed, there is only one way to index pattern (b). With the help of computer-generated Kikuchi projections, one of which will be shown later in Figure 48, indexing of the second pattern is not difficult. The angle of specimen tilt was found to be 27.45° for this case.

In choosing boundary vectors, three types of vectors previously described in Section III-B-5 can be selected. Higher accuracy in boundary normals can be achieved if two vectors whose projected images are more sensitive to specimen tilt are used. A schematic drawing of the

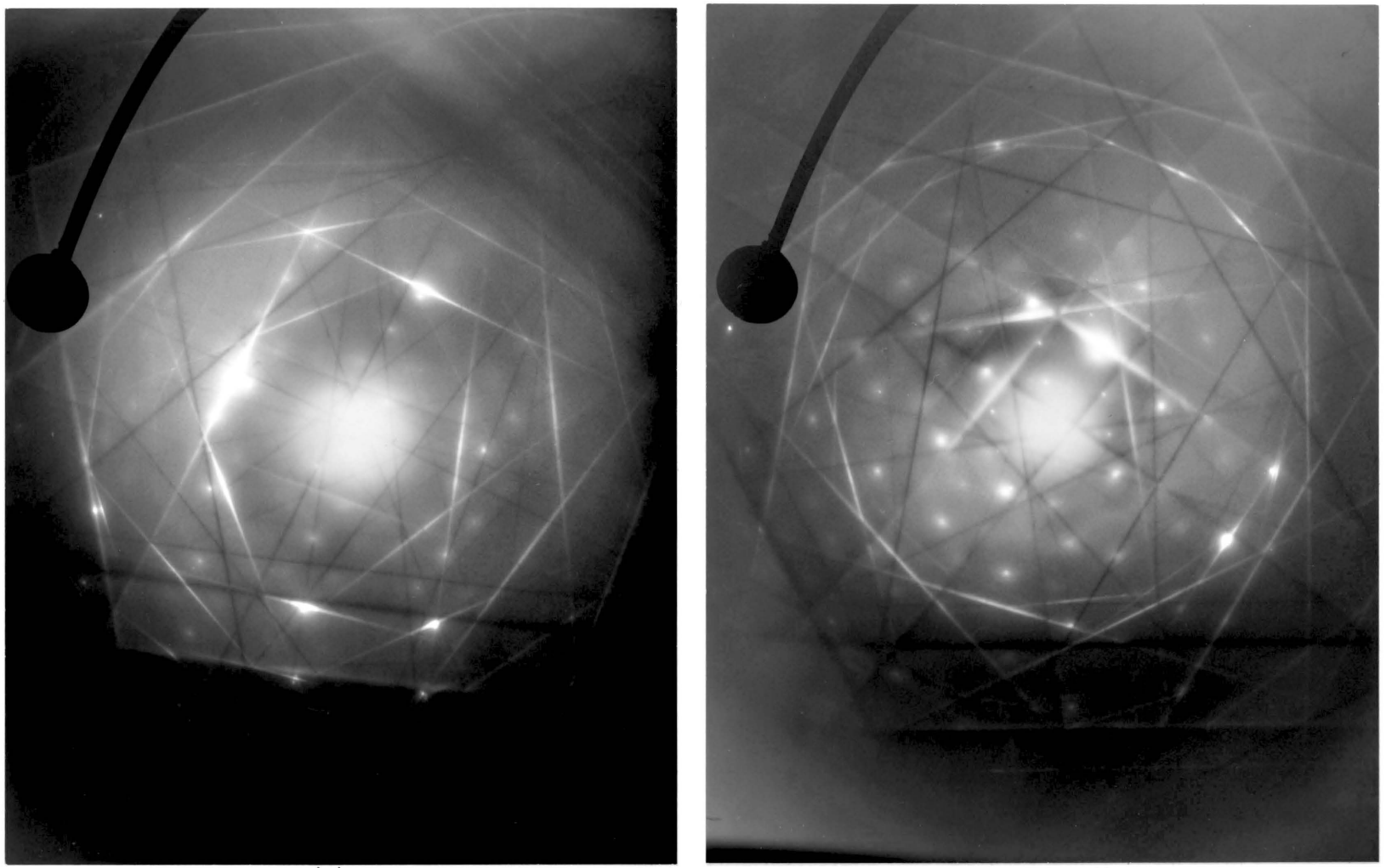

(a) (b)

Fig. 24. Two Kikuchi patterns from Al-0.5 at.% Ag crystal taken (a) before and (b) after specimen tilt.

projected images of two γ' platelet in an aged Al-0.5 at.%Ag thin foil is shown in Figure 25 to demonstrate the selection of boundary vectors. In general, the first choice (type 1) is a vector whose length is well defined, (e.g., vectors 1a and 1b in Figure 25 which extend from one platelet corner to another), preferably a vector with a relatively large angle of inclination to the projection plane (vector 1a). The second choice (type 2, see Figure 25) is a boundary width vector which is preferred when a relatively large change in boundary width is observed as a result of specimen tilt. The third choice (type 3, Figure 25) is the boundary trace direction. The last choice should be avoided unless no other types of boundary vector are available, since the trace direction is usually rather insensitive to specimen tilt, and a slight error in angular measurement may result in a large error in boundary normal. It should be used only for a boundary plane with rather large angle of intersection with the projection plane, and for a case where a relatively large tilting component about the projection of the trace direction occurs.

Figure 26 shows two bright field images of some γ' platelets before and after specimen tilt. The corresponding Kikuchi patterns were shown previously in Figure 24. Ten γ' platelets were selected and marked with numbers on micrograph (b). Their normals were calculated using the same, as well as different types of boundary vectors, if choices were available. The magnification of micrograph (b) is 5% less than that of micrograph (a) due to change of specimen position, and therefore all the lengths measured on micrograph (b) are multiplied by the correction factor of 1.05. The angular deviations of the calculated platelet normals as compared with the corresponding {111} family planes are listed in Table III. The column

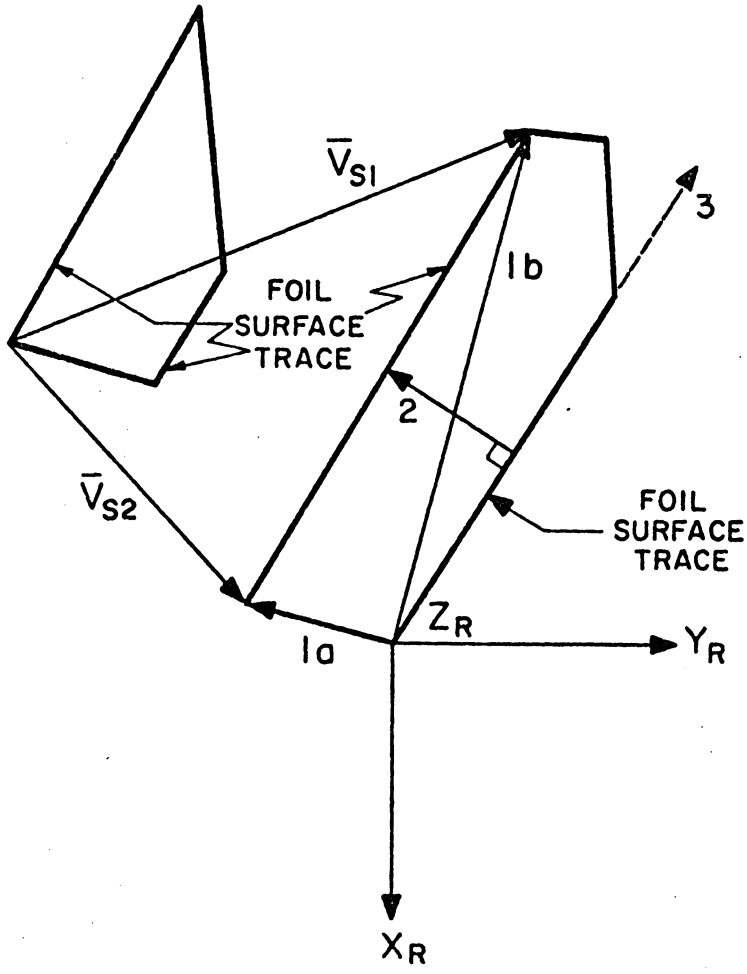

Fig. 25. A schematic diagram of the projected images of two γ' platelets in aged Al-0.5at.%Ag thin crystal, showing the possible selection of boundary vectors and surface vectors for the determination of platelet normal and surface normal.

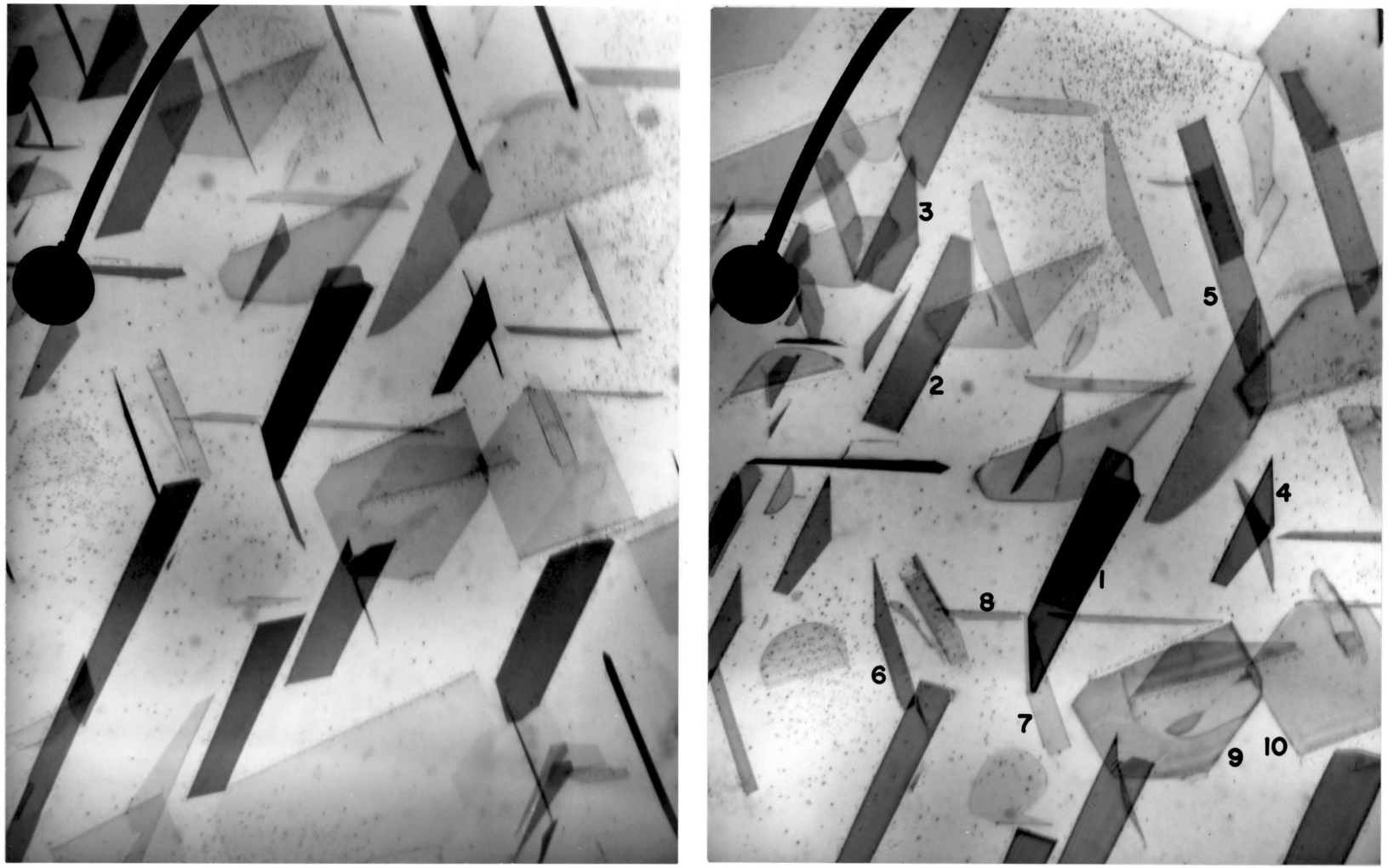

(a) (b)

Fig. 26. γ' platelets in Al-0.5 at.% Ag crystal aged at 160°C for 3000 hours, (a) before and (b) after specimen tilt. The corresponding Kikuchi patterns are shown in Figure 24.

Table III. Angular Deviation of Platelet Normals from {111}

Platelet No.	Angular Deviation from {111} (Degrees)					
	With Magnification Correction*			Without Magnification Correction		
	Vector type Combinations			Vector type Combinations		
	11	12	13	11	12	13
1. (111)	1.98			3.81		
2. (111)	1.08			5.27		
3. (111)	1.28			4.14		
4. (111)	2.15			5.53		
5. (11$\bar{1}$)	1.19	1.18	0.99	1.02	1.04	0.78
6. (11$\bar{1}$)	1.95	2.40	2.09	1.91	2.34	1.95
7. (11$\bar{1}$)	1.37	2.60	2.13	1.45	2.36	1.85
8. (1$\bar{1}$1)	1.63	1.08	0.48	1.65	0.82	0.42
9. (1$\bar{1}\bar{1}$)	4.78			7.76		
10. (1$\bar{1}\bar{1}$)	6.33			11.30		

* The magnification correction used here was based upon the fact that all ten platelets must rotate together and suffer the same magnification shift. Although this approach is accurate, it is a complex procedure which is not necessary if a curve such as that of Figure 15 is available.

headings indicate the types of vectors selected. For example, the heading 12 indicates that one of the boundary vectors is type 1 and the other is type 2, and the heading 23 means one vector is type 2 and the other is type 3. The results in Table III indicate that the boundary normal can be determined to within an average accuracy of $\pm 2^{o}$. When a boundary is inclined at a rather large angle to the projection plane, solutions from 12 and 23 are as accurate as solutions from 11. However, the last two platelets, platelets 9 and 10, have a small angle of intersection with the projection plane, and the angular deviations are about $5\text{-}6^{o}$. Therefore, the present analysis is highly accurate only for those boundaries with relatively large angle of inclination to the projection plane.

The angular deviations of the computed platelets normals for the ten platelets shown in Figure 25 were also calculated without correcting the error in magnification due to the change of specimen position as a result of specimen tilt. The results are also listed in Table III. It is seen that without the correction for magnification, 5% in the present case, the deviations are generally large.

The sensitivity of calculated boundary normals to a change of input angle of relative image-pattern rotation has also been checked. The results indicate that the boundary normals are not sensitive to the input angle of image-pattern rotation. A change of 1^{o} in image-pattern rotation always results in a variation of less than 1^{o} in boundary normal. The angle of image-pattern rotation, which is not effected by the change of specimen position, can be obtained from a carefully prepared calibration curve to within 1^{o} accuracy or better. Therefore, the possible error in calculated boundary normal due to the error of input angle of image-pattern rotation should be well within $\pm 1^{o}$.

Trace analysis employed in the determination of boundary normal requires the knowledge of either foil thickness, or foil inclination, or both in order to obtain a reliable result. Foil thickness can be determined either by extinction contour method or trace analysis of a known plane. However, it has been shown that the former consistently gives larger values of foil thickness by 10-50% [35]. Even after obtaining the foil thickness, there exists another possible serious source of error in trace analysis for unknown plane normals due to the uncertainty of foil inclination. With a tilting stage of $\pm$ 20° tilting range, the possible error could be as high as 60° depending on the boundary plane inclination, foil inclination, and trace direction[21].

The present analysis for boundary normal determination requires no knowledge of either foil thickness or surface orientation, and a reasonably accurate foil thickness can be obtained in some cases as the by-product of this analysis. When the foil surface is perpendicular to the beam axis, the Z component of a defined vector or a boundary width vector which joins the top and bottom surfaces of the foil is the foil thickness. If surface inclination is within $\pm$5° of being zero and the vector selected for foil thickness determination has an angle of inclination greater than 60°, the foil thickness so determined will generally be accurate to $\pm$5%, assuming no error is involved in the calculated Z component. If foil surface orientation is known, the dot product between the defined vector or the boundary width vector and the normalized surface normal is the foil thickness.

Theoretically, surface normal can also be obtained from the present analysis. If two non-parallel surface vectors, both lying on the same

foil surface, are selected and their coordinates are determined, the surface normal may be calculated by taking the cross product between the two vectors. In selecting the surface vectors, vectors are preferred with defined length, such as the two vectors $\bar{V}_{S1}$ and $\bar{V}_{S2}$ shown in Figure 25. Trace directions, such as the type 3 vector in Figure 25, may also be used. The change in either length or direction of the projected images of surface vectors or traces resulting from specimen tilt is usually small. Therefore, extremely careful measurement from sharp and well-defined images would be required.

D. Computer-Generated Stereographic Kikuchi Projections

In the present study, a number of the standard stereographic Kikuchi projections (K-projections) with systematic variations in orientation as well as variations in projection sphere radius (PSR) have been obtained for FCC (Al), BCC (Fe), diamond cubic (Si), and HCP (α-Ti) crystals. A zone axis projection (Z-projection) associated with each K-projection was also generated for automatic indexing of Kikuchi poles. For those K-projections with small PSR the pole indices were plotted on separate sheets to prevent overcrowding, and for those with larger PSR (30 cm or more) the pole indices were plotted directly on the K-projections. All the plots generated are approximately 6" x 6" in size, and can thus be placed in a binder for easy reference. A printed list associated with each K-projection was also programmed for automatic indexing of individual Kikuchi lines.

During the course of the investigation of characterization of general bicrystals, the collection of K-projections and their associated Z-projections was invaluable in providing proper indexing of Kikuchi patterns. With the help of Kikuchi projections, indexing of an observed pattern becomes a straight forward comparison between the pattern and the computer-plotted projections. The observed pattern is first compared with projections of smaller PSR which cover a wide angular range of Kikuchi space. On the observed patterns, Kikuchi pairs resulting from low-index crystallographic planes usually appear as bands. These Kikuchi bands can be conveniently used as clues in locating the beam axis on the projections. Once the approximate orientation is found, the pattern is then referred to an appropriate K-projection with larger PSR for detailed comparison.

Other line diffraction projections, such as the projections of Coates patterns and transmitted Kossel patterns, were also obtained in this study. Since Kikuchi patterns, Coates patterns, and transmitted Kossel patterns or pseudo-Kossel patterns are line diffraction patterns with the same diffraction mechanisms and projection geometries, the general programs written for Kikuchi projections can be used to generate these projections simply by changing the input wave lengths.

In the following, a series of examples are given. For cubic crystals, examples are given mostly using the projections from FCC (Al). The application of the projections are also briefly described.

Figure 27 is a full [001] zone axis projection associated with the [001] Kikuchi projection given in Figure 28, which is a projection of FCC (Al) at 100KV (wave length λ =0.0370A). On the Z-projection the "+" symbol under each group of directional indices indicates the projection of the pole bearing those indices. In Figure 27, only those poles which are shared by four or more of the first-order Kikuchi pairs plotted in Figure 28, i.e., MDZP=4, are indexed. Therefore, when the Z-projection is laid on top of the K-projection, the indices of those K-poles, each shared by four or more existing K-pairs and having no overlap with other neighboring printed poles can be read directly from the Z-projection. The arrow drawn at the bottom of each projection indicates the azimuth of the X1 reference axis of the standard basis for the desired projection. A rotation of each projection about the origin can be made simply by changing the specification of the X1 direction in the input program. For non-cubic crystals, it is sometimes difficult to calculate the desired X1 direction. In such a case, a direction X1' which lies on the X1-X3

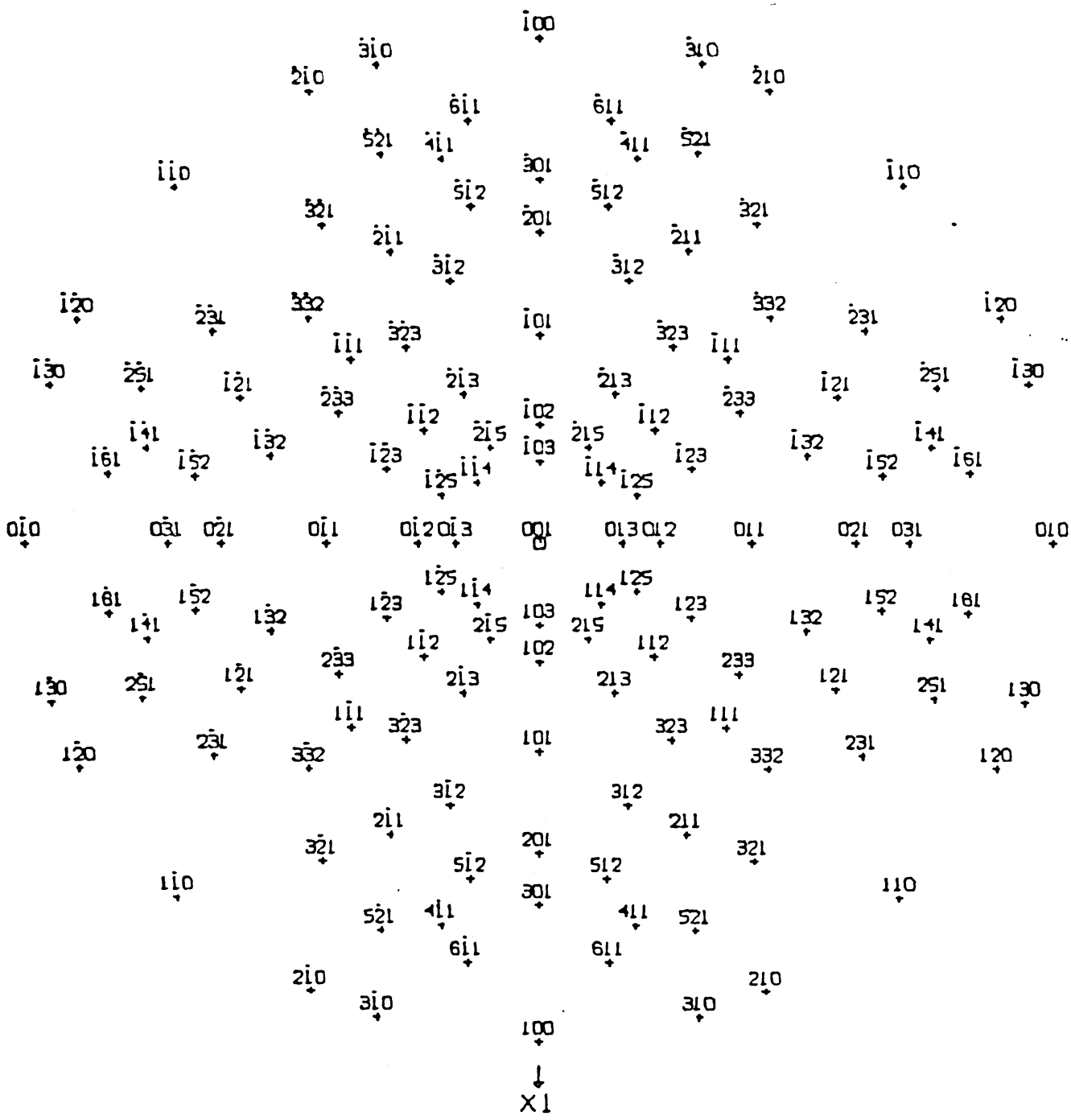

Fig. 27. [001] standard stereographic zone axis projection associated with the Kikuchi projection of FCC crystal given in Figure 28. PSR = 4.12 cm, MDZP = 4, X1 = [100].

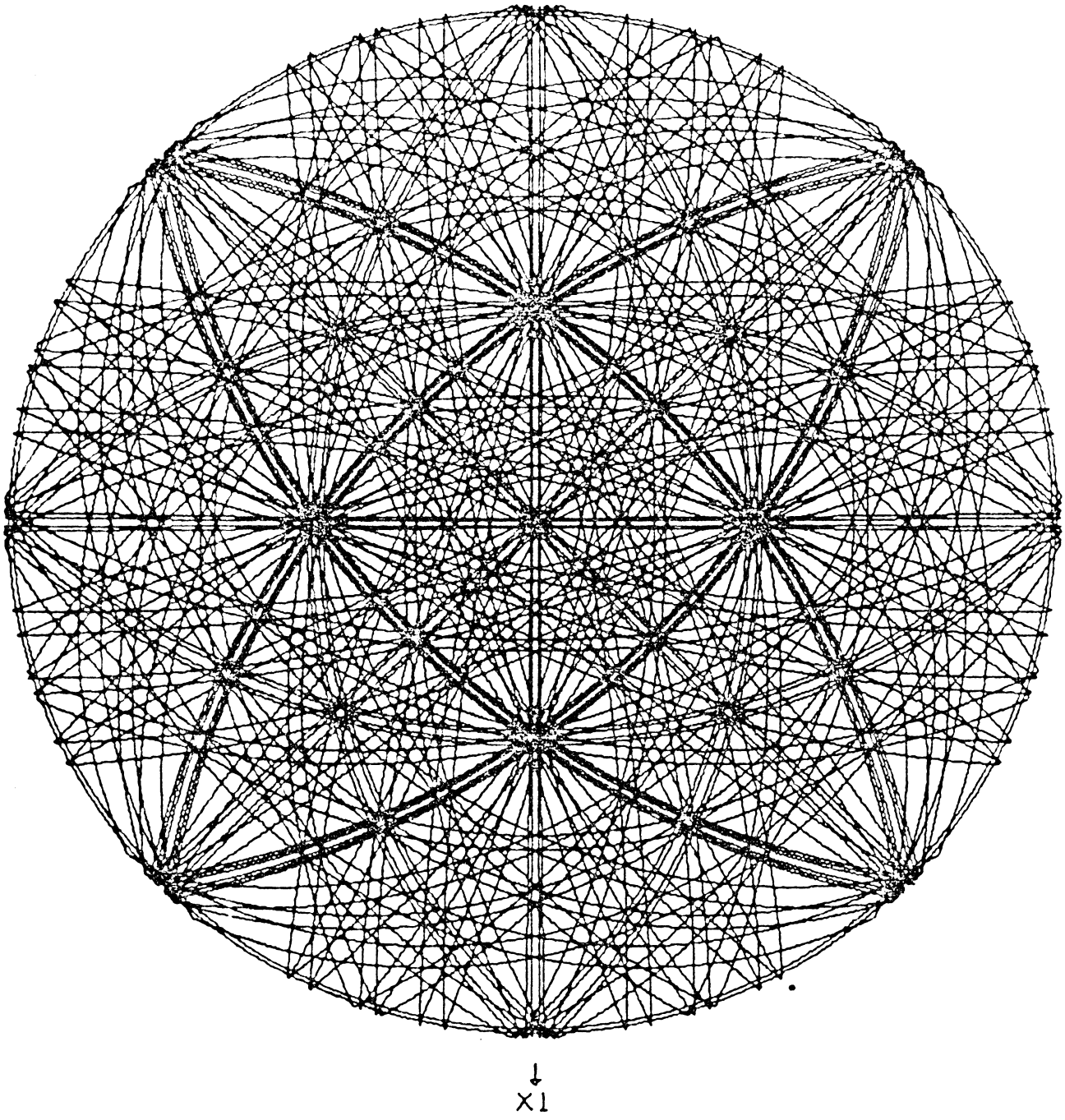

Fig. 28. [001] standard stereographic Kikuchi projection of FCC (Al) crystal at 100KV (λ = 0.0370A).
PSR = 4.12 cm, MS = 32, X1 = [100].

quadrant plane may be used as the input X1 direction, and a direction which is given by the cross product of $(\bar{X}3 \times \bar{X}1) \times \bar{X}3$ will be automatically taken as the X1 direction in the calculation. Therefore, the input directions of X1' and X3 axes need not be perpendicular to each other in this case. The projection sphere radii (PSR) for both Figure 27 and 28 are specified to be 4.12 cm (1.622 inches). Since the diameter of the full stereographic projection is four times the value of PSR, a plotting area greater than or equal to 6.5" x 6.5" must be specified in order to hold the full projection. The maximum S value (MS) is 32 in Figure 28. Consequently, Kikuchi lines resulting from those crystallographic planes with d-spacings smaller than those of {440} planes are not seen in the projection.

Figures 29 and 30 are the [001] full K-projections at 100KV for BCC (Fe), and DIC (Si) crystals, respectively. These projections, together with the projection shown in Figure 28, demonstrate the overall appearance of the Kikuchi projections of low PSR for the three cubic structures selected in the present study. For different crystals of the same structure, the K-pair separations will vary with lattice parameters and electron wave length, but the positions of K-poles will be the same.

Figure 31 and 32 are the [0001] Z-projection and K-projection for HCP (α-Ti) crystal. The K-projection also shows the whole picture of the projections of small PSR from HCP crystals. The K-pair separations will vary with lattice parameters and wave length. The pole positions will change with c/a ratio, but the basic projection symmetry will remain the same. As mentioned previously, the number of K-lines plotted on K-projections is limited by specifying a maximum squared value of reciprocal

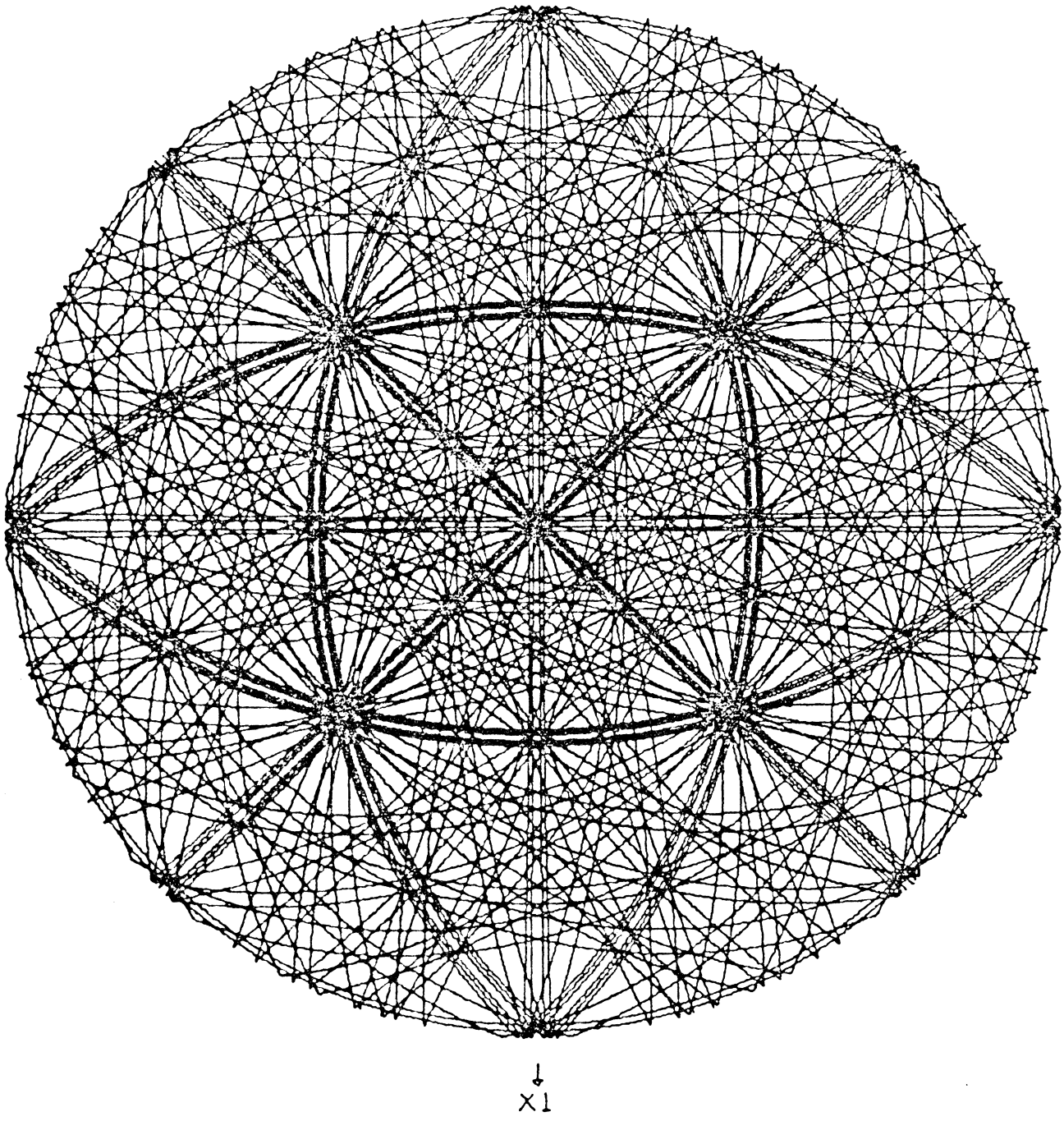

Fig. 29. [001] Kikuchi projection of BCC (Fe) crystal at 100KV. PSR = 4.12 cm, MS = 18, X1 = [100].

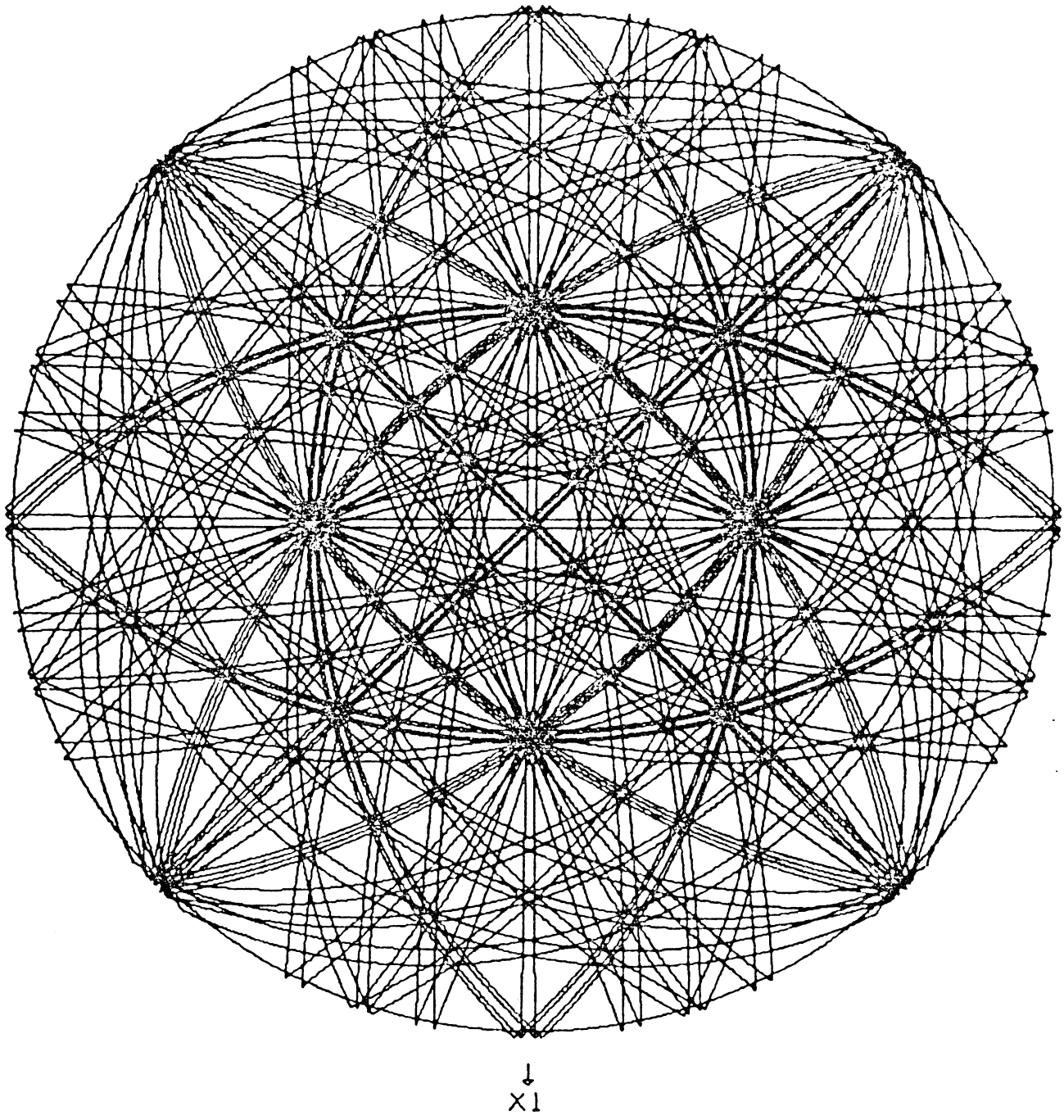

Fig. 30. [001] Kikuchi projection of DIC (diamond cubic, Si) crystal at 100KV.
PSR = 4.12 cm, MS = 32, X1 = [100].

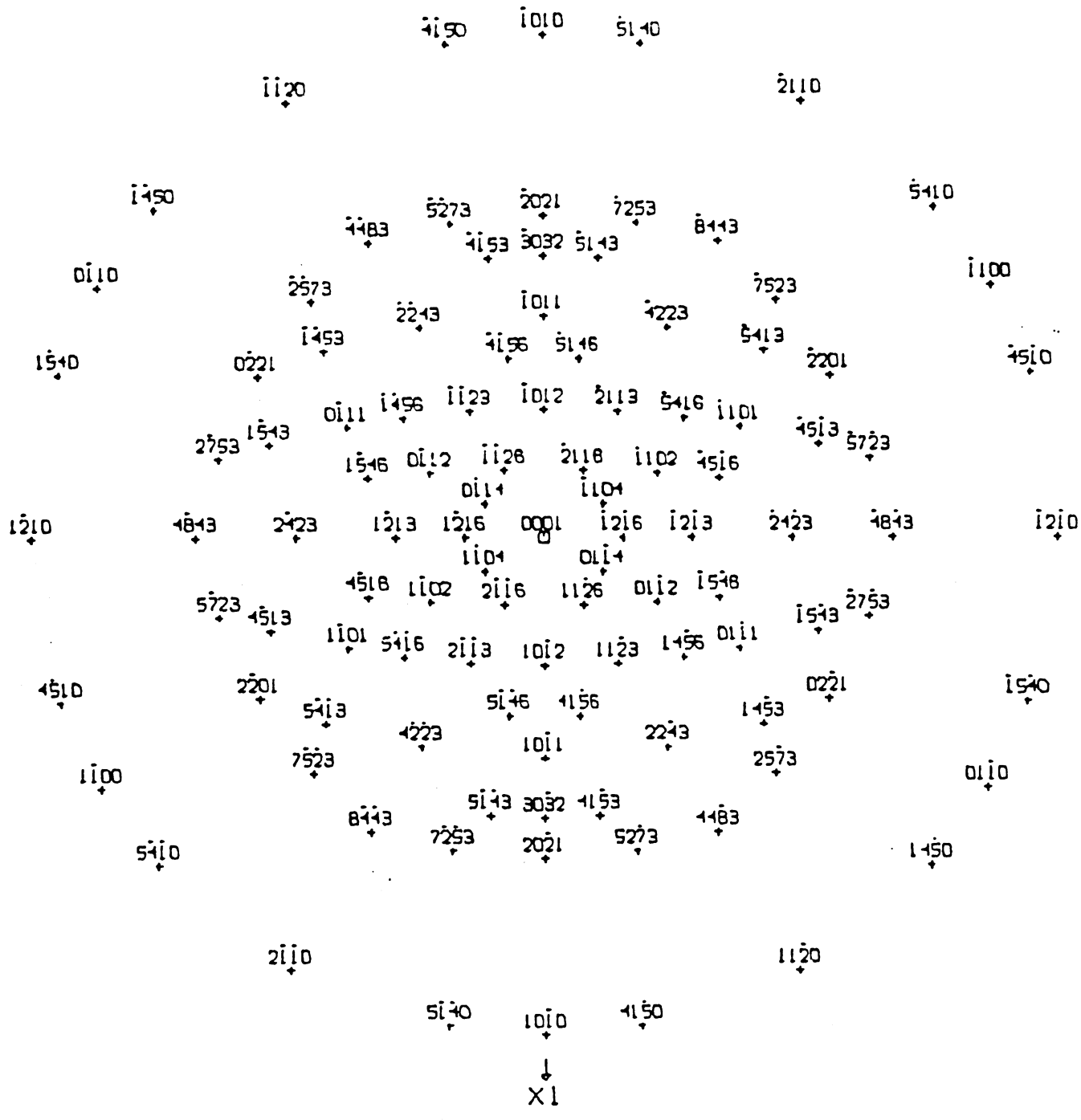

Fig. 31. [0001] zone projection associated with the Kikuchi projection of HCP crystal shown in Figure 32.
PSR = 4.12 cm, MDZP = 4, X1 = [10$\bar{1}$0].

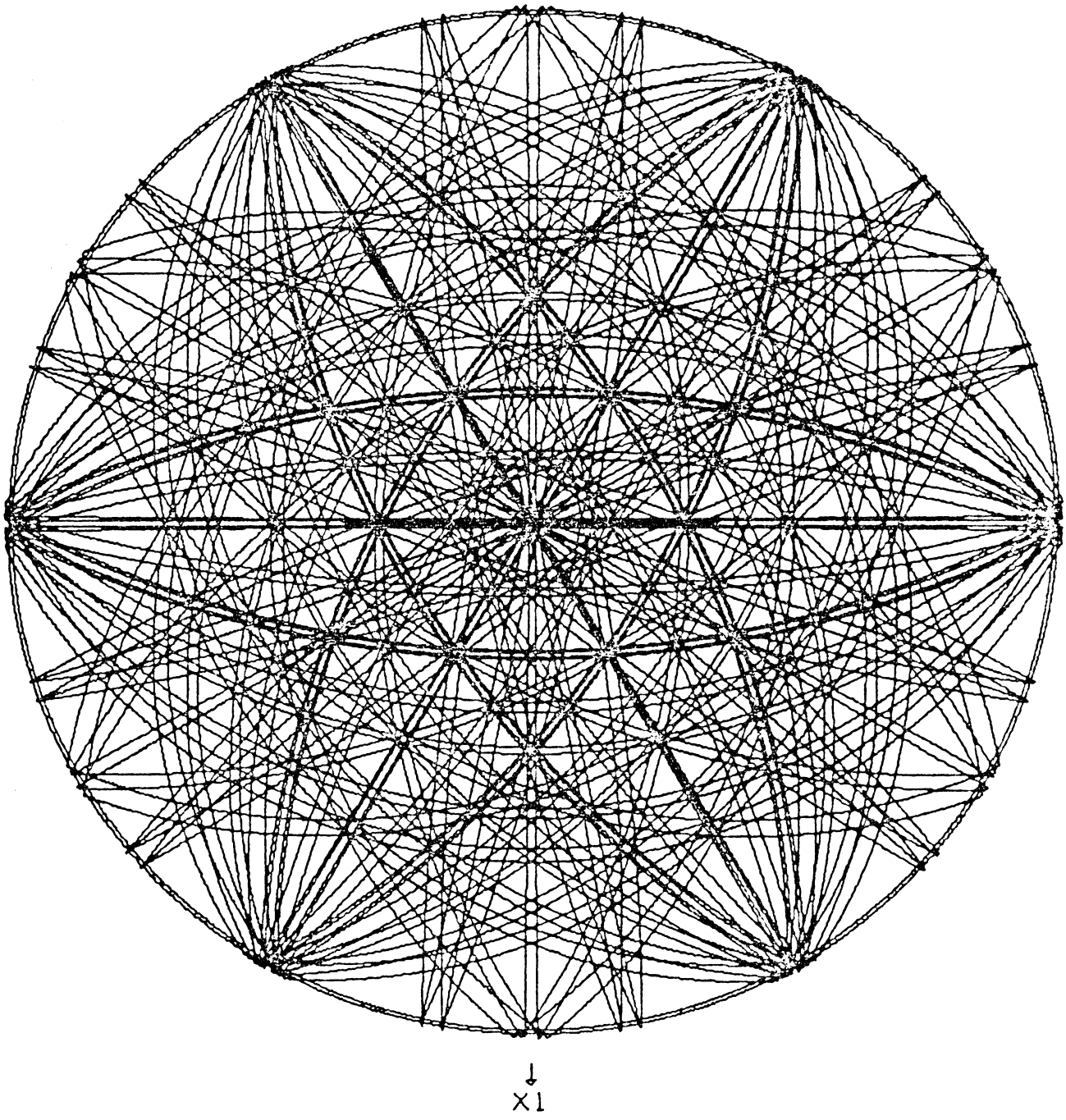

Fig. 32. [0001] Kikuchi projection of HCP (α-Ti) crystal at 100KV. PSR = 4.12 cm, RDL = 1.10, RDU = 1.20, X1 = [10$\bar{1}$0].

d-spacing, (RD). However, for the reason which will be given in the Appendix Section B, two parameters, (RDL) and (RDU), were used as limiting parameters in the present study.

Figure 33 is a complete [001] Coates projection of FCC (Al) crystal at 20KV (λ=0.0865A). In comparison with Figure 28, the line pair separations are seen to increase, since the wave length is larger. The pole configurations are still recognizable.

Figure 34 shows a complete [001] transmitted pseudo-Kossel projection of FCC (Al) using Co Kα radiation (λ=1.7902A). For x-ray diffraction, the semi-appex angles of diffraction conics are generally much smaller than 90^{o}, and the Kossel lines are seen to appear on the projection as segments of circles or full circles. The pole configurations observed on Kikuchi and Coates projections do not occur on the Kossel projection. Therefore, for Kossel projections, plane normals are plotted on the corresponding Z-projections.

Figure 35, 36, and 37 are the [001], [011], and [111] K-projections of FCC crystals, each covering an angular range more than 100^{o}. The projection at the outer areas of each projection are still rather distorted as expected in stereographic projections. Nevertheless, these projections are useful in the first comparison when an observed pattern is to be indexed.

For a cubic crystal, the product of the multiplicity factor of a zone axis (or plane normal) and the rotational symmetry about that axis should always be equal to 24. Since the multiplicity factor of [001], [011], and [111] are 6, 12, and 8, respectively, the corresponding rotational symmetry about these axes are 4, 2, and 3, respectively. This

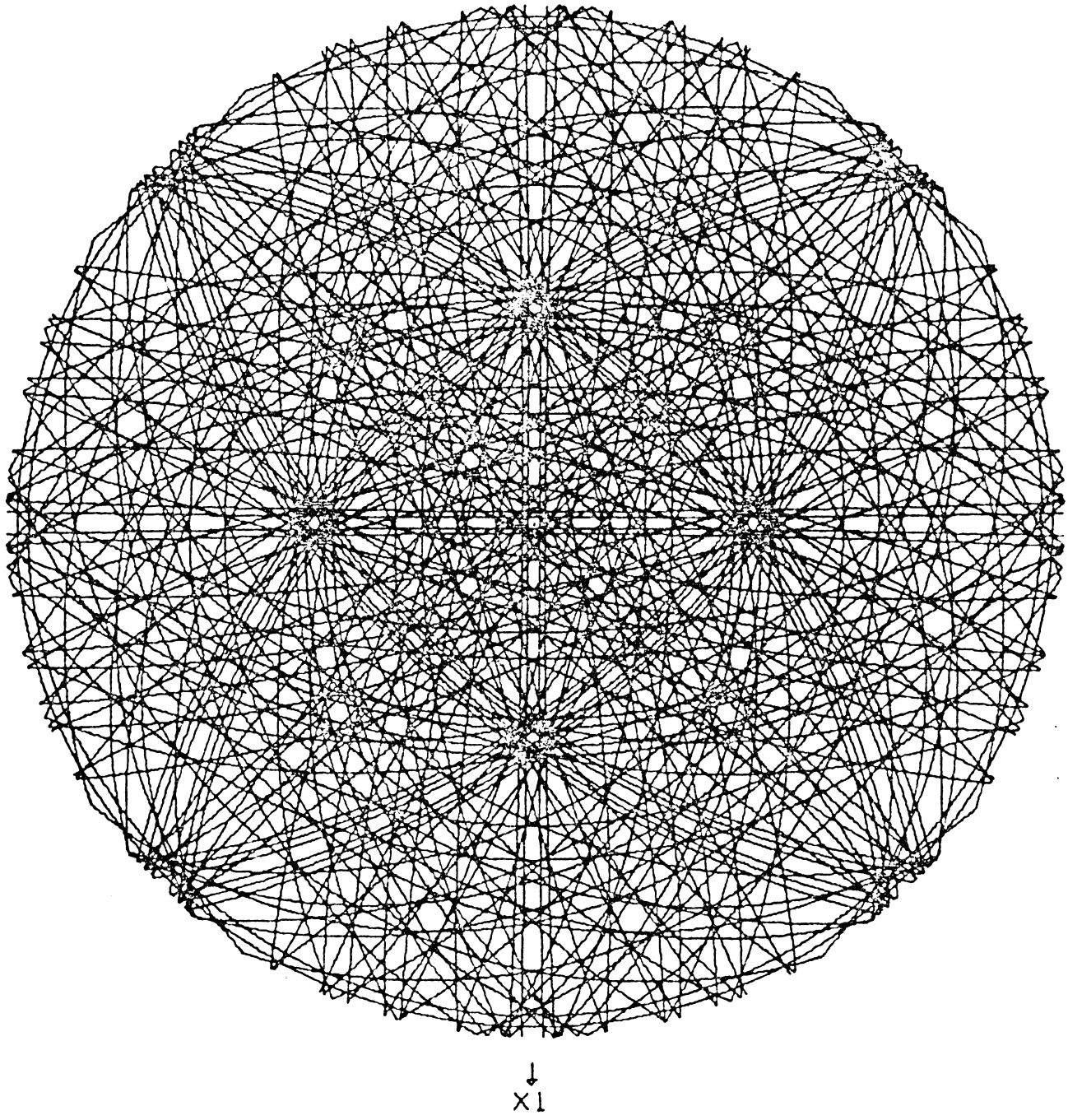

Fig. 33. [001] Coates projection of FCC (Al) crystal at 20KV (λ = 0.0865A).
PSR = 4.12 cm, MS = 32, X1 = [100].

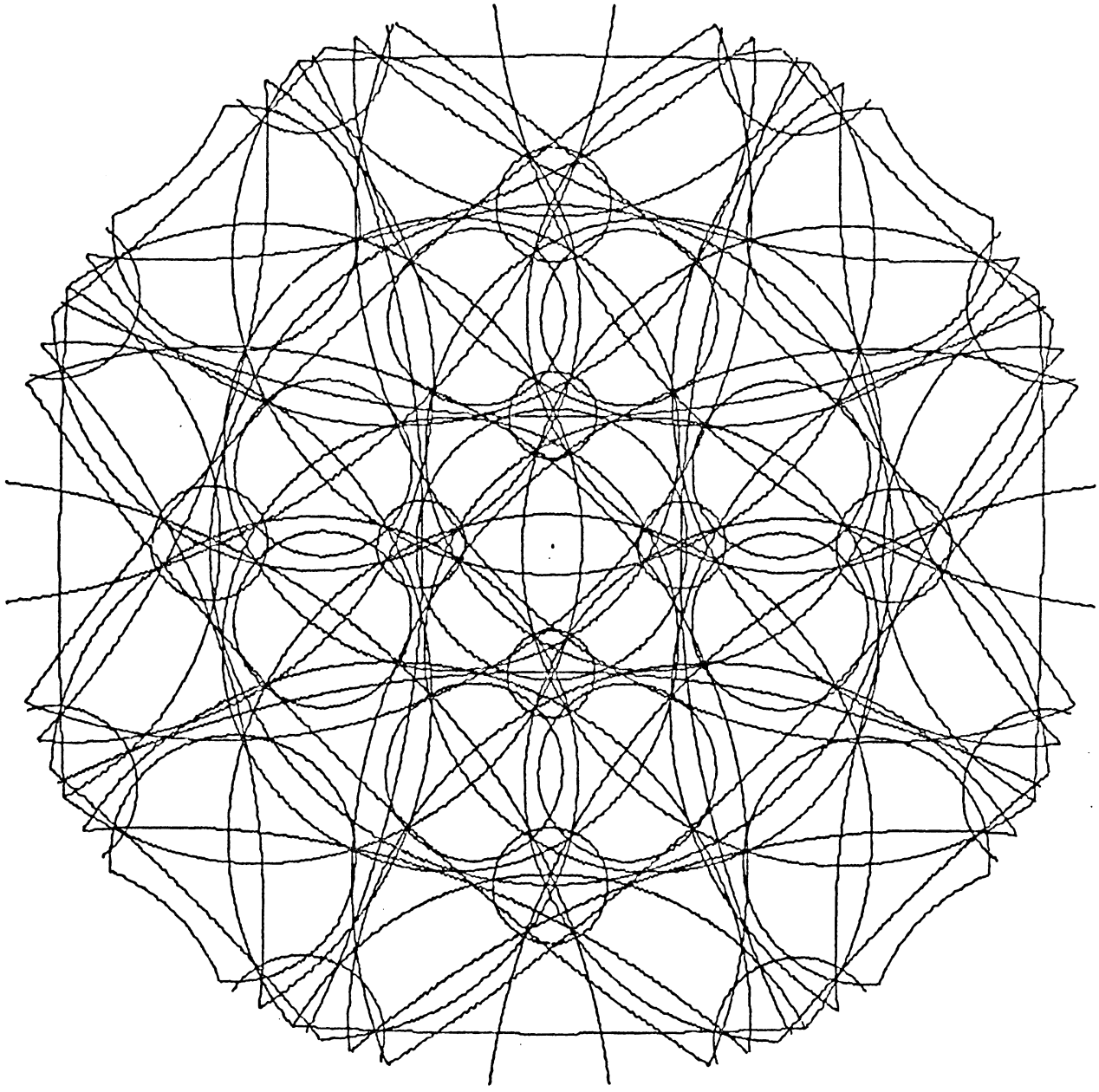

Fig. 34. [001] pseudo-Kossel projection of FCC (Al) crystal using CoK_α radiation (λ = 1.7902A).
PSR = 4.12 cm, MS = 16, X1 = [100].

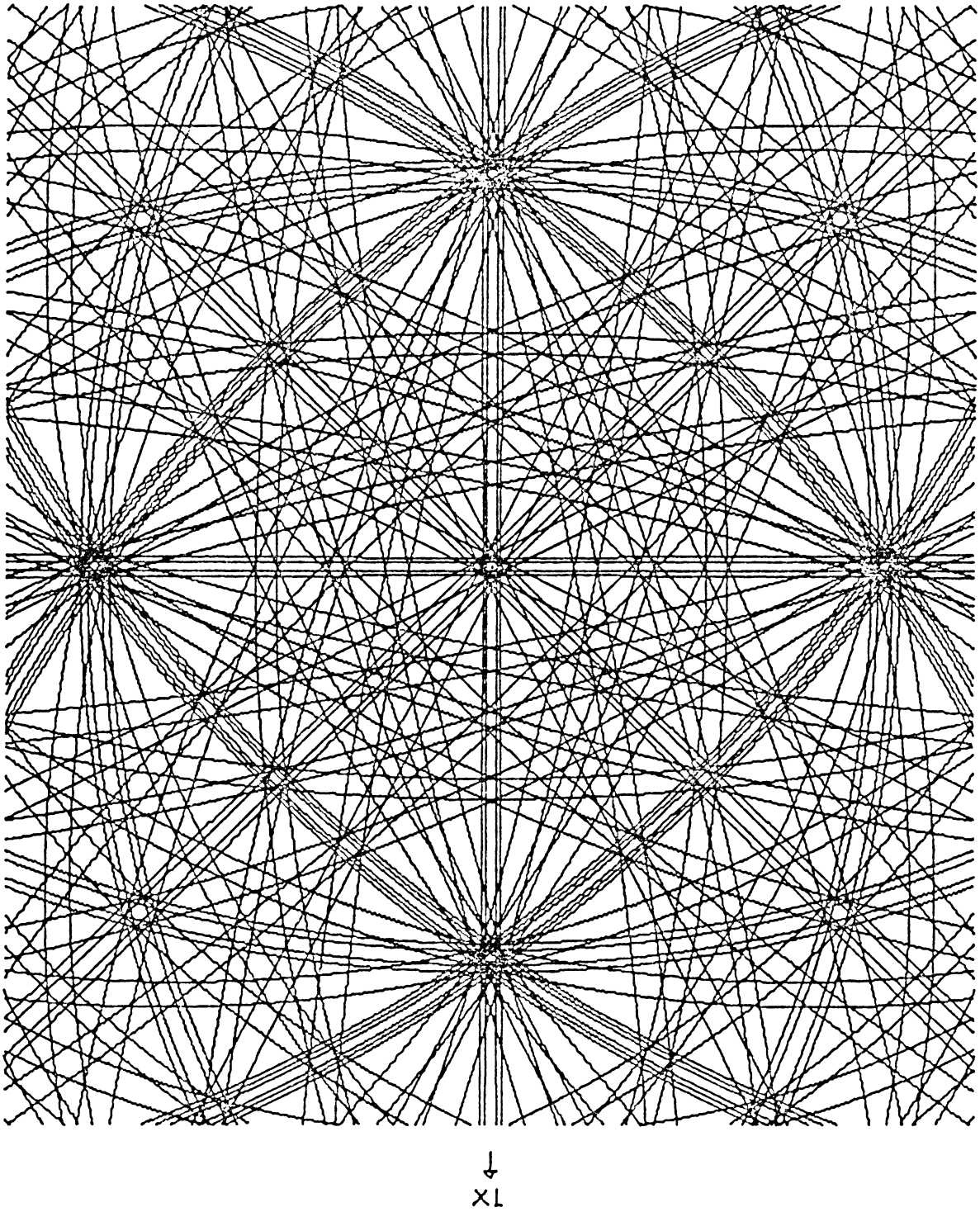

Fig. 35. [001] Kikuchi projection of FCC (Al) crystal at 100KV. PSR = 7.50 cm, MS = 32, X1 = [100].

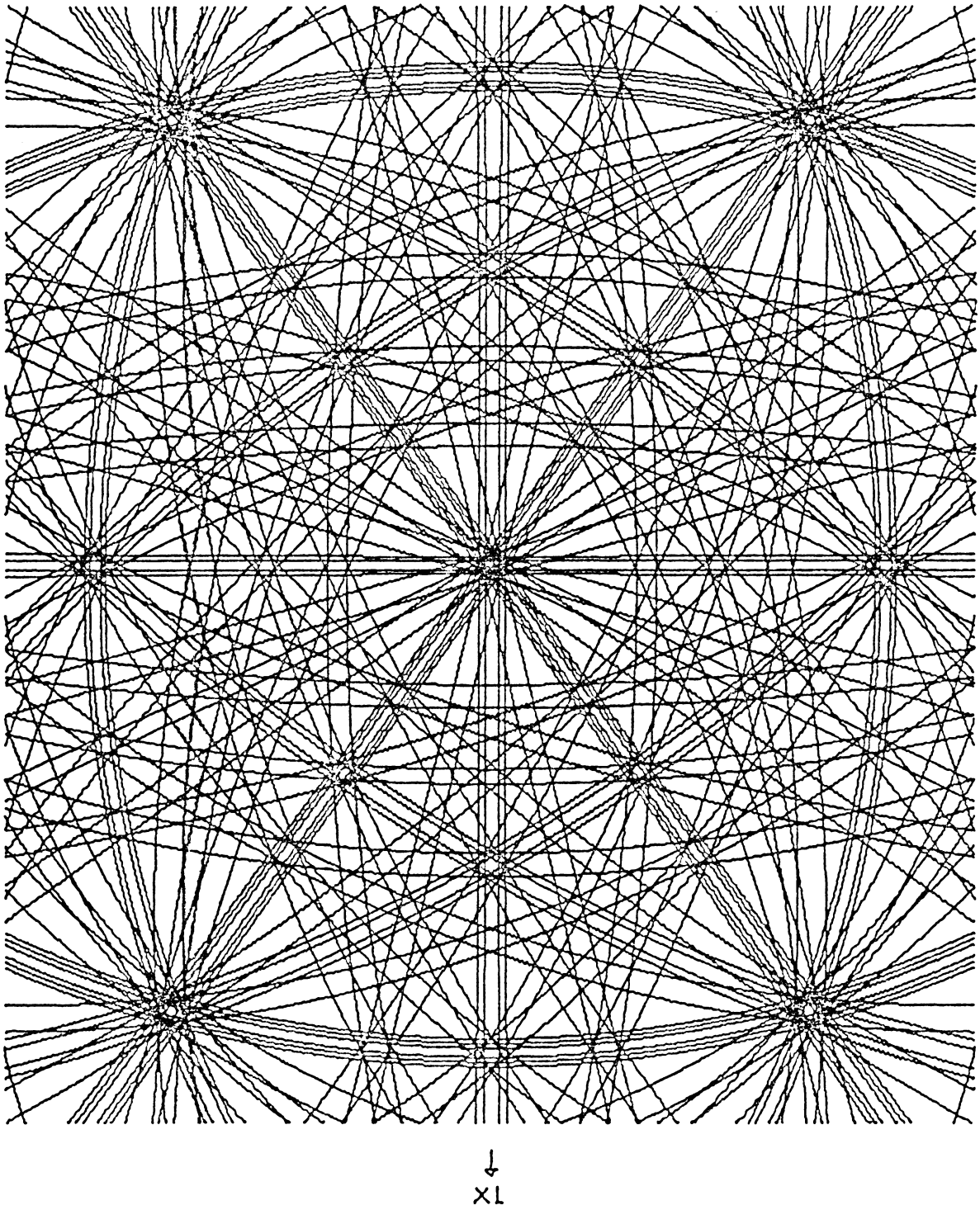

Fig. 36. [011] Kikuchi projection of FCC (Al) crystal at 100KV
PSR = 7.50 cm, MS = 32, X1 = [100].

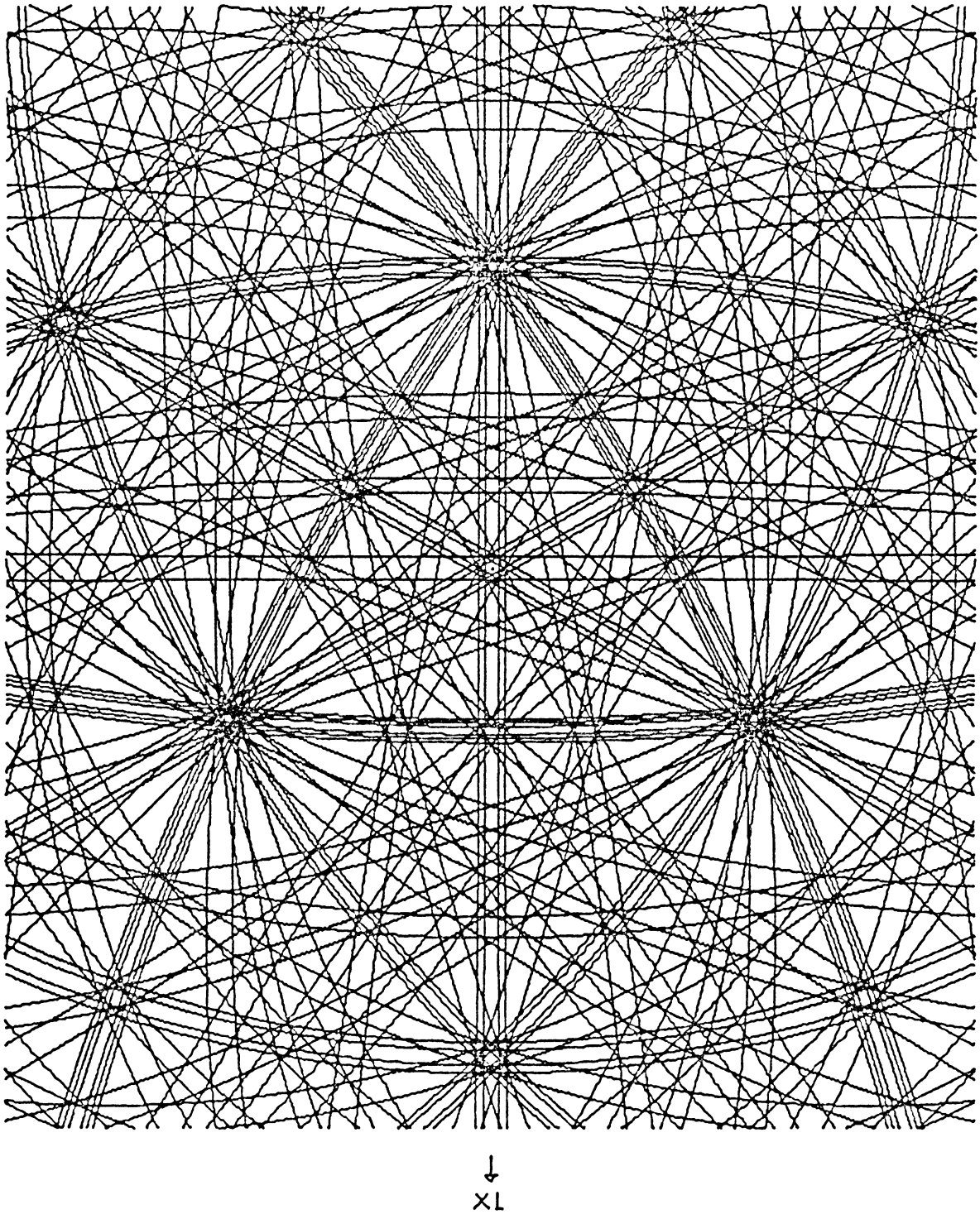

Fig. 37. [111] Kikuchi projection of FCC (Al) crystal at 100KV. PSR = 7.50 cm, MS = 32, X1 = [2$\bar{1}\bar{1}$].

can be seen from the K-projections shown in Figures 35, 36, and 37. For those $\langle hk\ell \rangle$ zone axes, where h, k, and ℓ are non-zero and are not equal to each other, the multiplicity factor is 48, and the whole family of axes must be divided into two groups by permuting the h, k, and ℓ indices. The permutation must account for both the change in order and the change in sign. Therefore, the [123] and [213] axes, for example, are not crystallographically equivalent. A [123] Kikuchi pole cannot be indexed as [213], $[\bar{1}23]$, or $[\bar{1}\bar{2}\bar{3}]$, etc..

Figures 38 and 39 are the [0001] Z-projection and K-projection of HCP (α-Ti) crystal. Figures 40 and 41 are the $[\bar{1}2\bar{1}0]$ Z-projection and K-projection of the same crystal. These two K-projections cover more than 360^{o} angular range of Kikuchi space, and have a common $[10\bar{1}0]$ X1 axis. Although the projection at the outer areas of each projection is rather distorted, these projections are useful in the preliminary comparison with the observed patterns. Since the basic symmetry of K-projections does not vary with c/a ratio, the projections for α-Ti crystals are applicable for a variety of HCP crystals.

Figure 42 through 47 are the [001] Z-projections and K-projections of FCC, BCC, and DIC crystals, each covering the [001]-[011]-[111]-[101] stereographic quadrant and having the origin located at the upper left corner. In the literature, the [001]-[011]-[111] stereographic triangle is usually used to present crystallographic information for cubic crystals. However, in some studies, including the plotting of line diffraction patterns, it requires a full stereographic quadrant to provide complete information. The projections shown in Figures 42 through 47 are believed to be the most convenient ones for use in indexing of a single Kikuchi pattern.

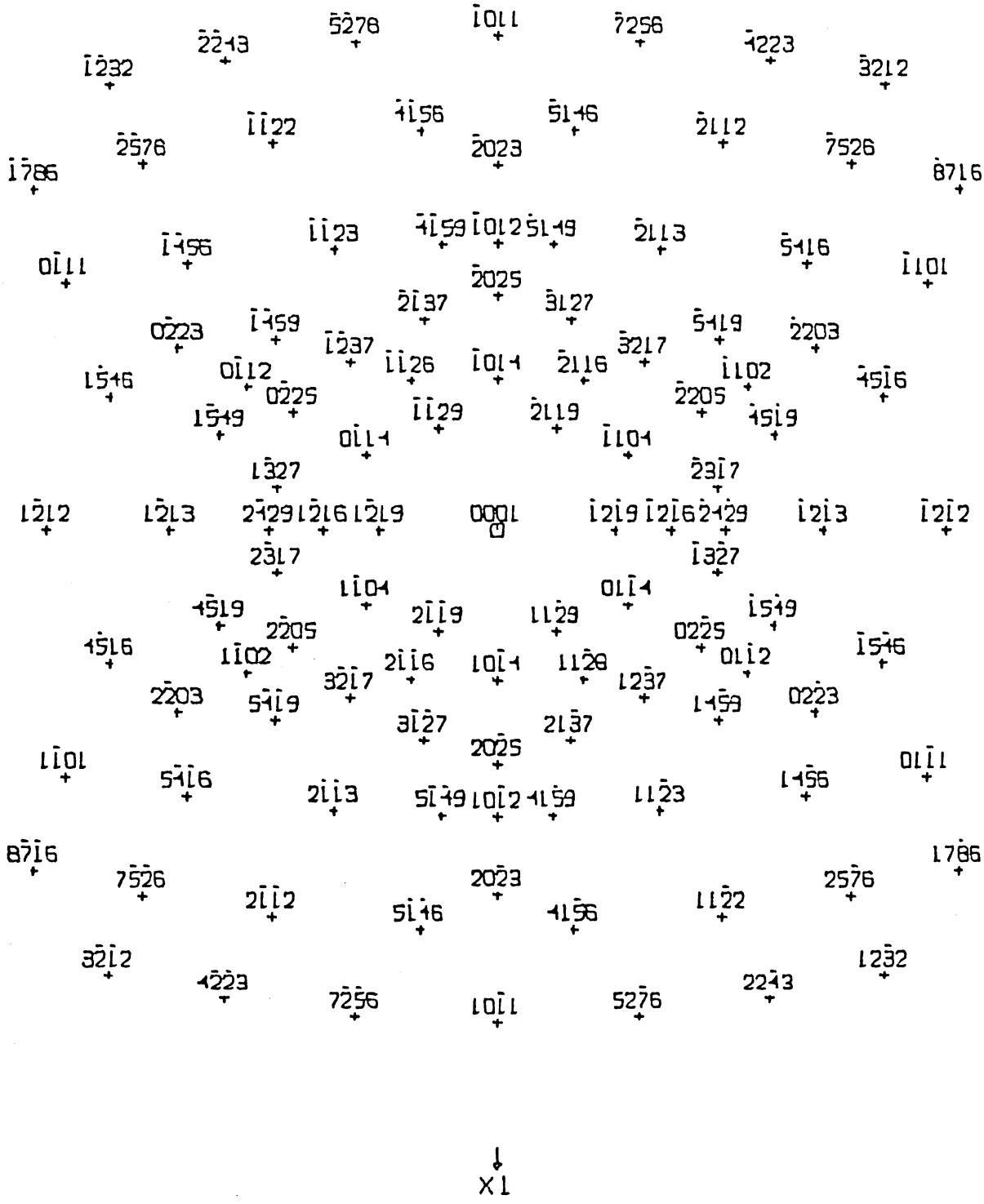

Fig. 38. [0001] zone projection associated with the Kikuchi projection given in Figure 39.
PSR = 9.00 cm, MDZP = 3, X1 = [10$\bar{1}$0].

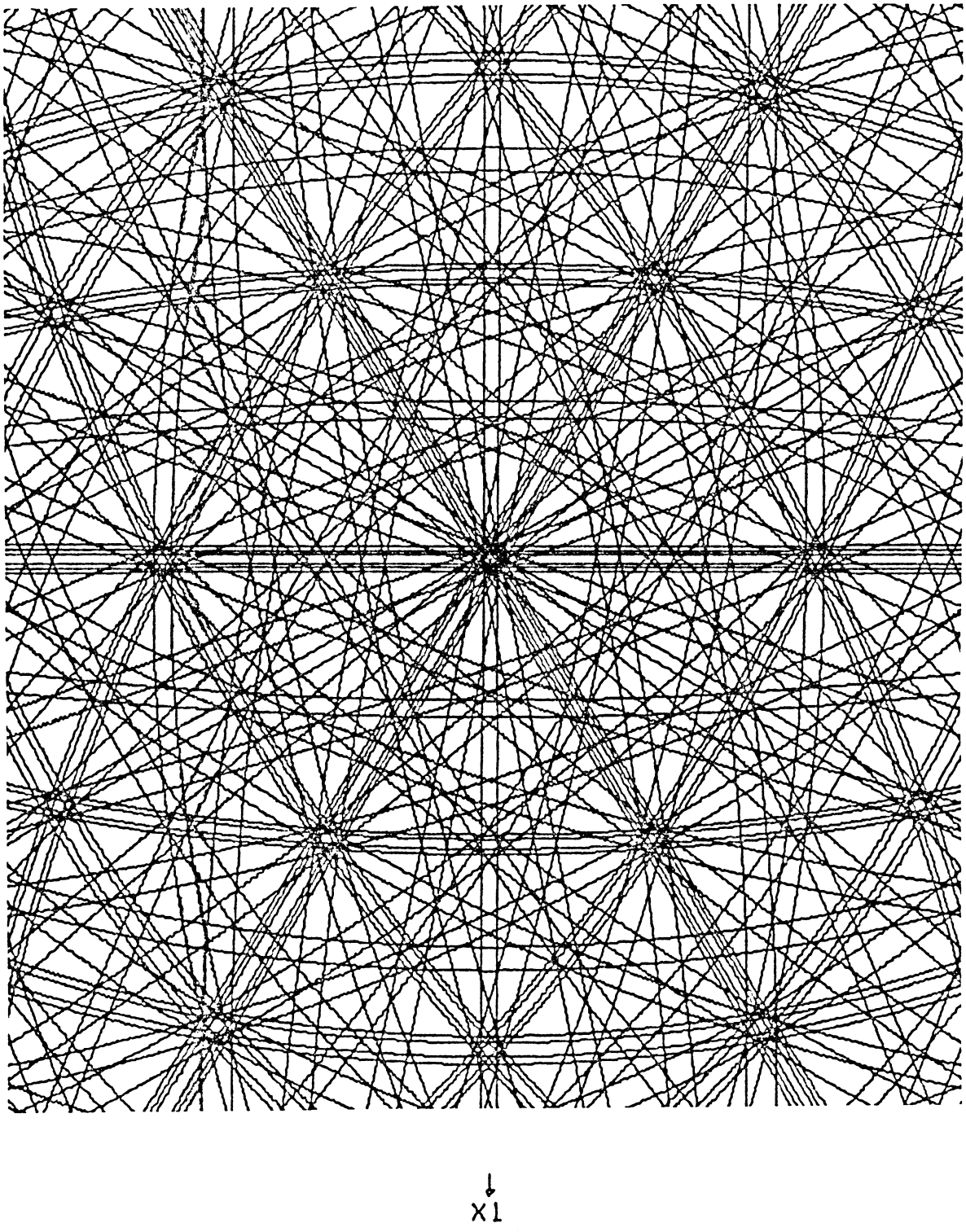

Fig. 39. [0001] Kikuchi projection of HCP (Ti) crystal at 100KV. PSR = 9.00 cm, RDL = 1.40, RDU = 1.40, X1 = $[10\bar{1}0]$.

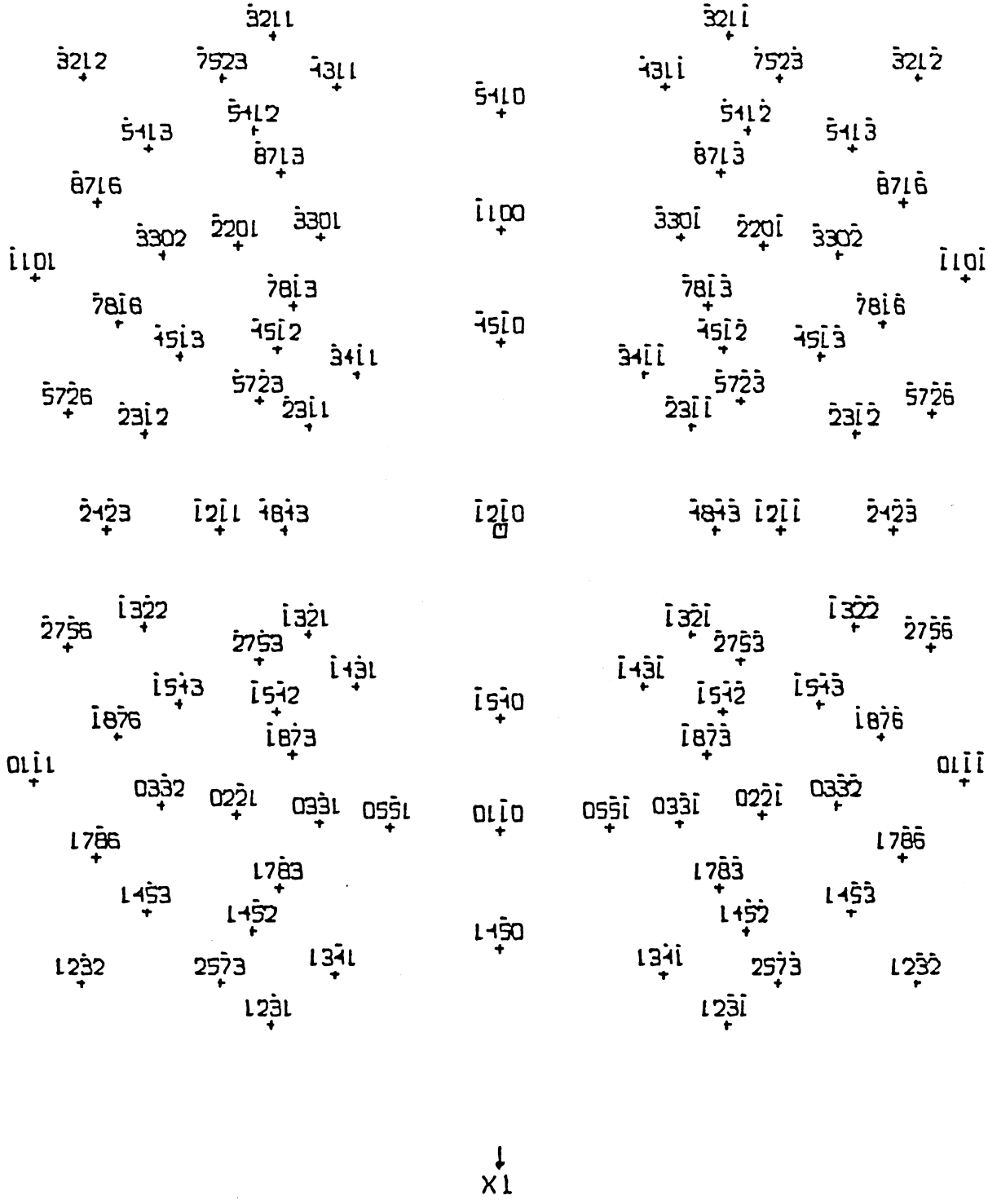

Fig. 40. [$\bar{1}2\bar{1}0$] zone projection associated with the Kikuchi projection given in Figure 41.
PSR = 9.00 cm, MDZP = 3, X1 = [$10\bar{1}0$].

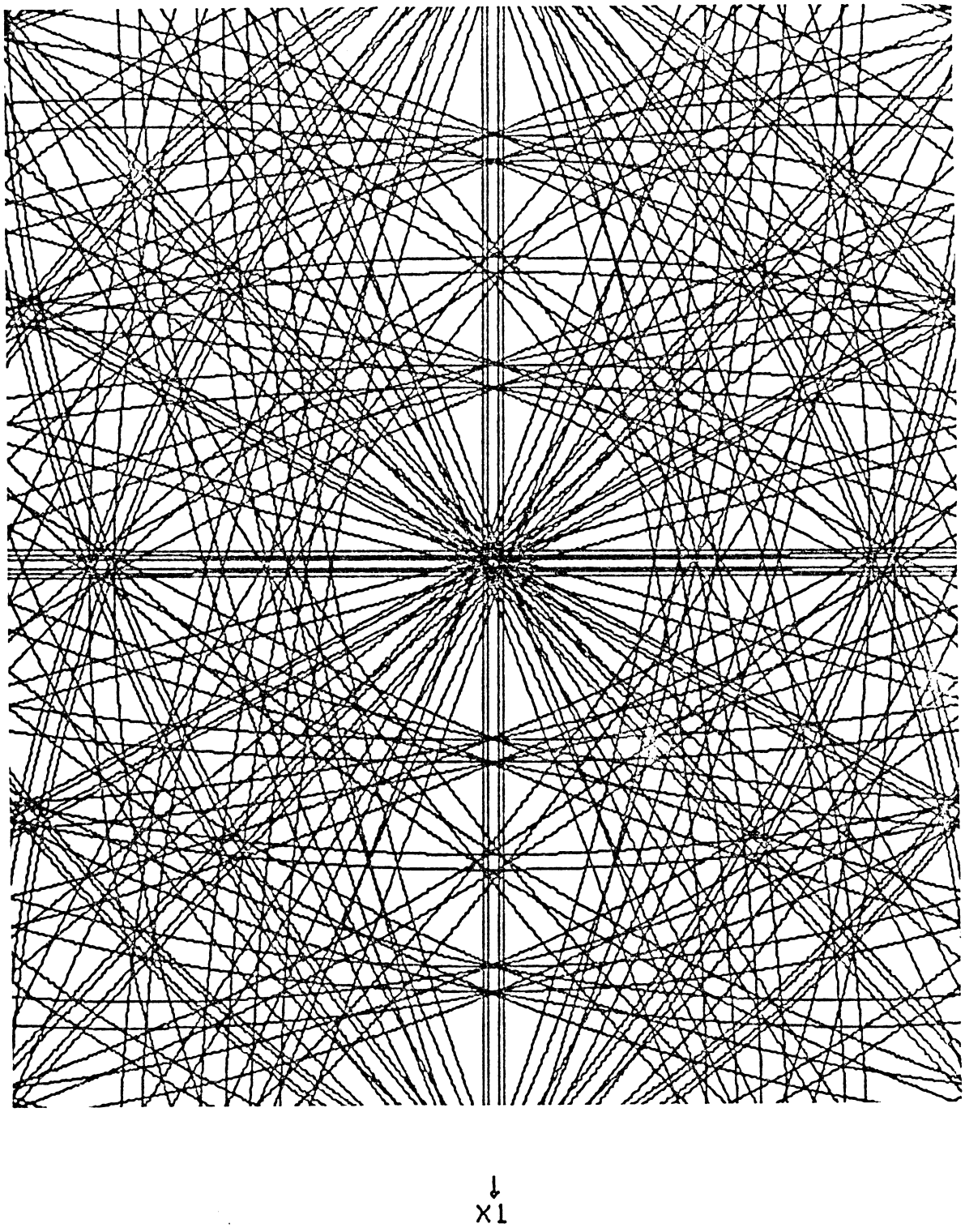

Fig. 41. $[\bar{1}2\bar{1}0]$ Kikuchi projection of HCP (Ti) crystal at 100KV. PSR = 9.00 cm, RDL = 1.40, RDU = 1.40, X1 = $[10\bar{1}0]$.

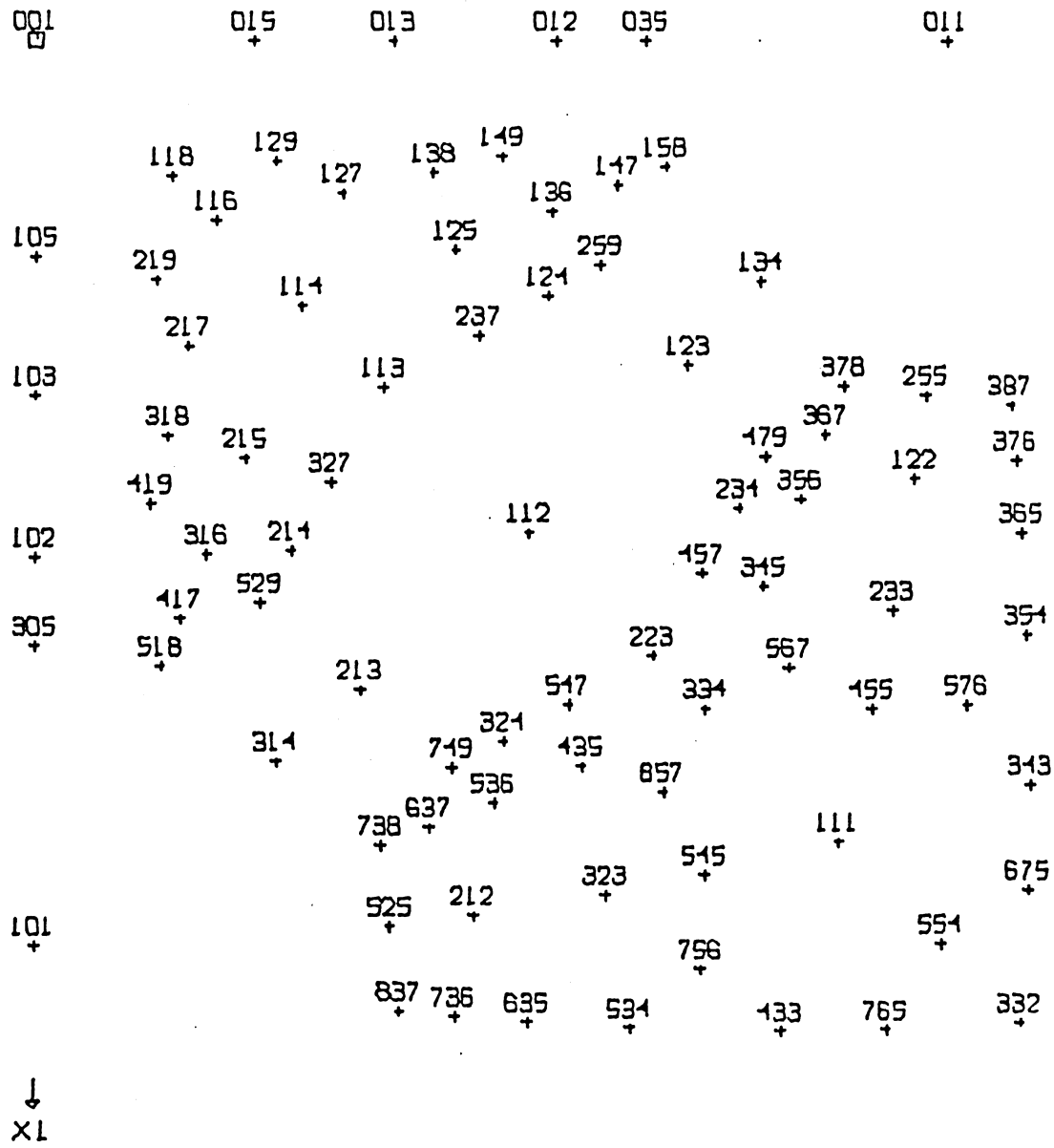

Fig. 42. [001] zone projection associated with the Kikuchi projection given in Figure 43.
PSR = 15.00 cm, MDZP = 3, X1 = [100].

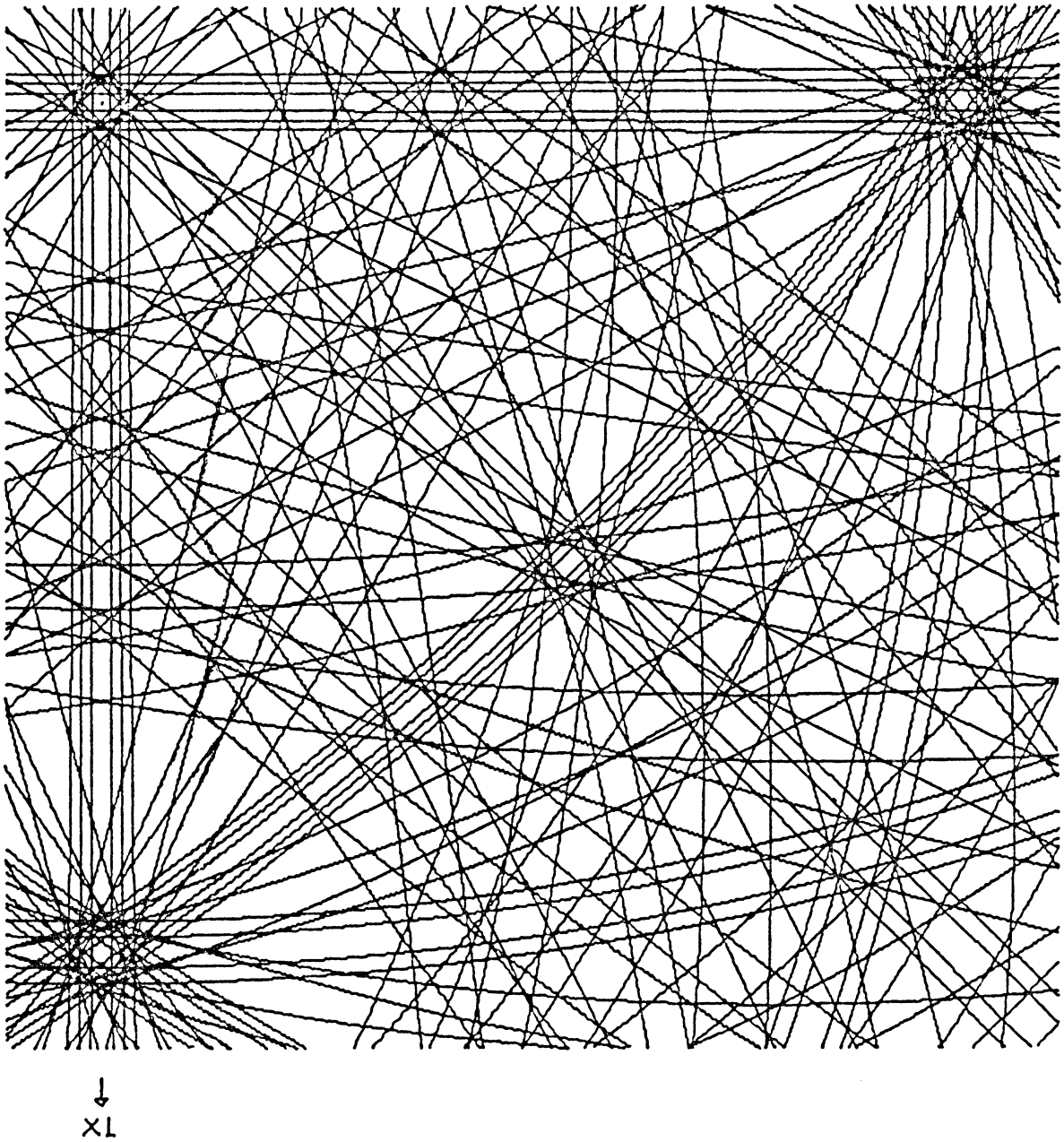

Fig. 43. [001] Kikuchi projection of FCC (Al) crystal at 100KV. PSR = 15.00 cm, MS = 36. X1 = [100].

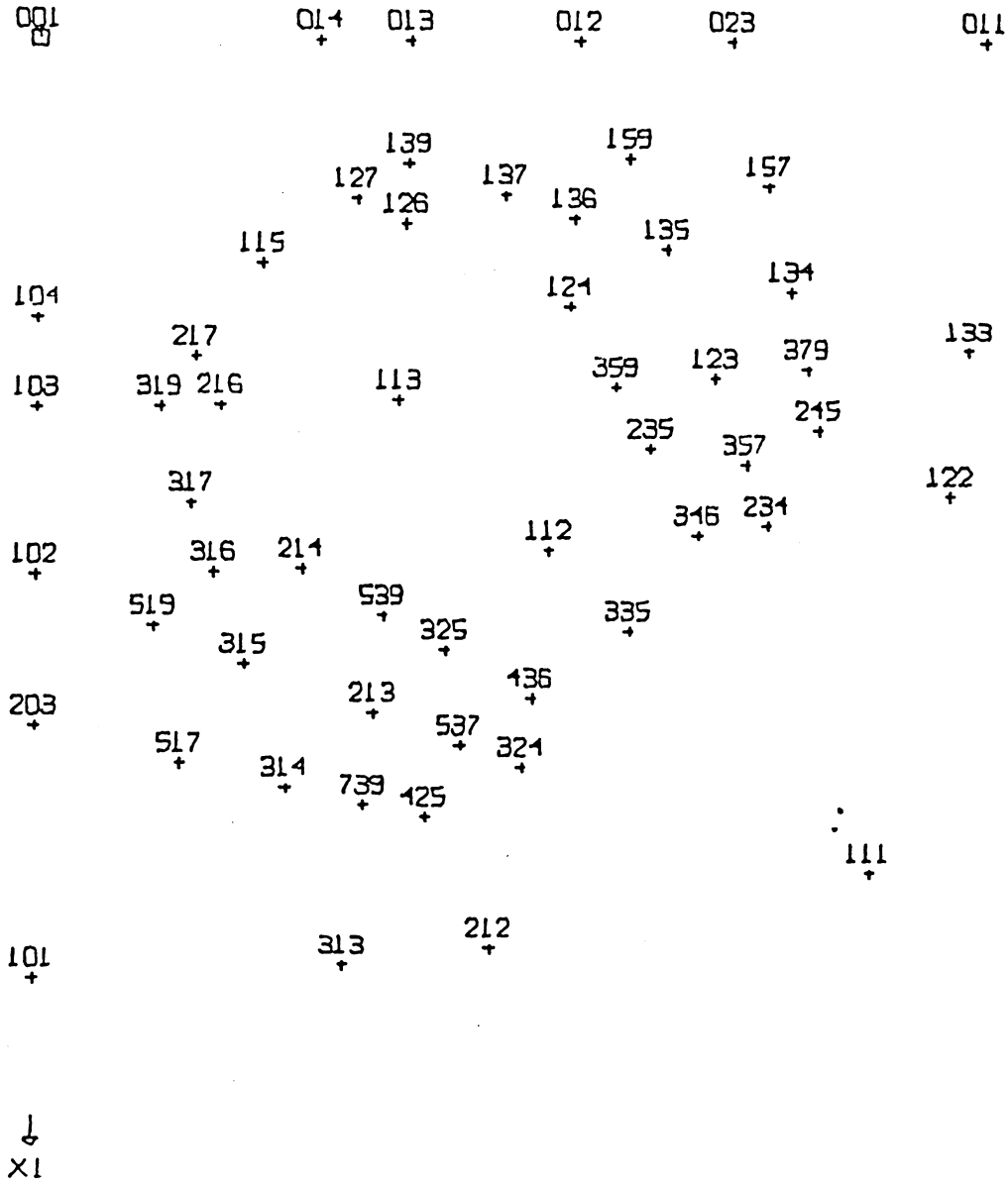

Fig. 44. [001] zone projection associated with the Kikuchi projection given in Figure 45.
PSR = 15.00 cm, MDZP = 3, X1 = [100].

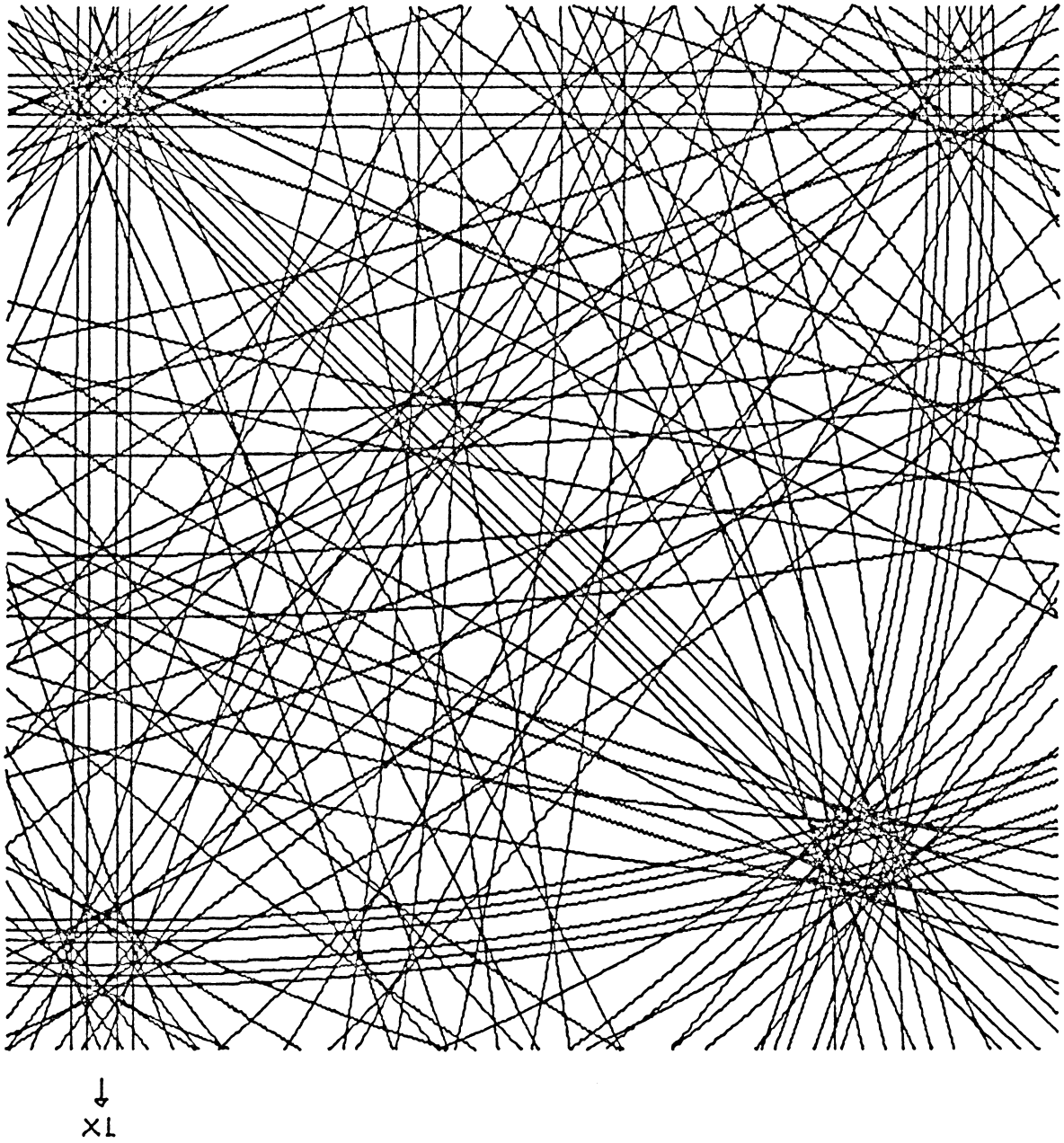

Fig. 45. [001] Kikuchi projection of BCC (Fe) crystal at 100KV. PSR = 15.00 cm, MS = 24, X1 = [100].

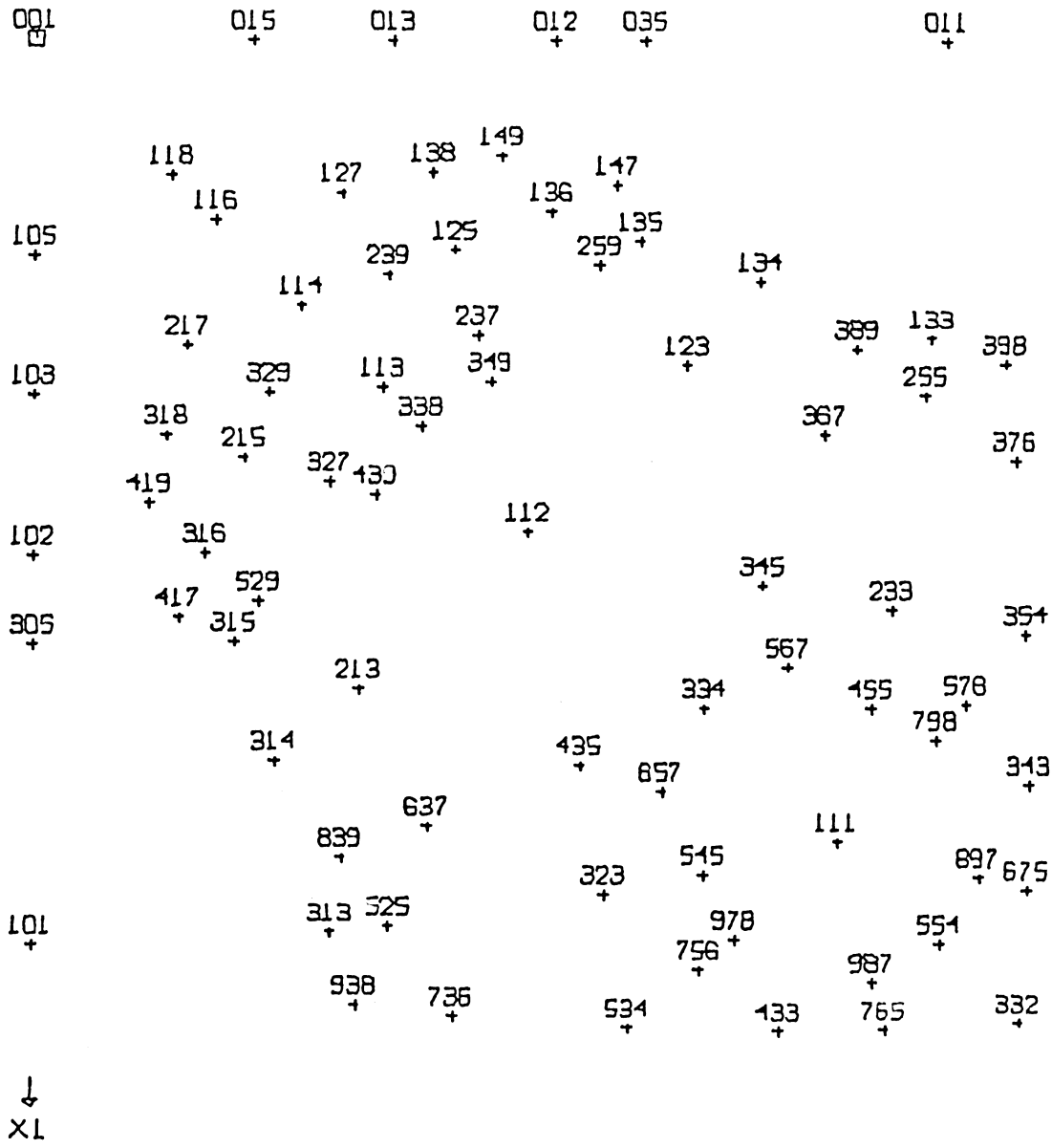

Fig. 46. [001] zone projection associated with the Kikuchi projection given in Figure 47.
PSR = 15.00 cm, MDZP = 3, X1 = [100].

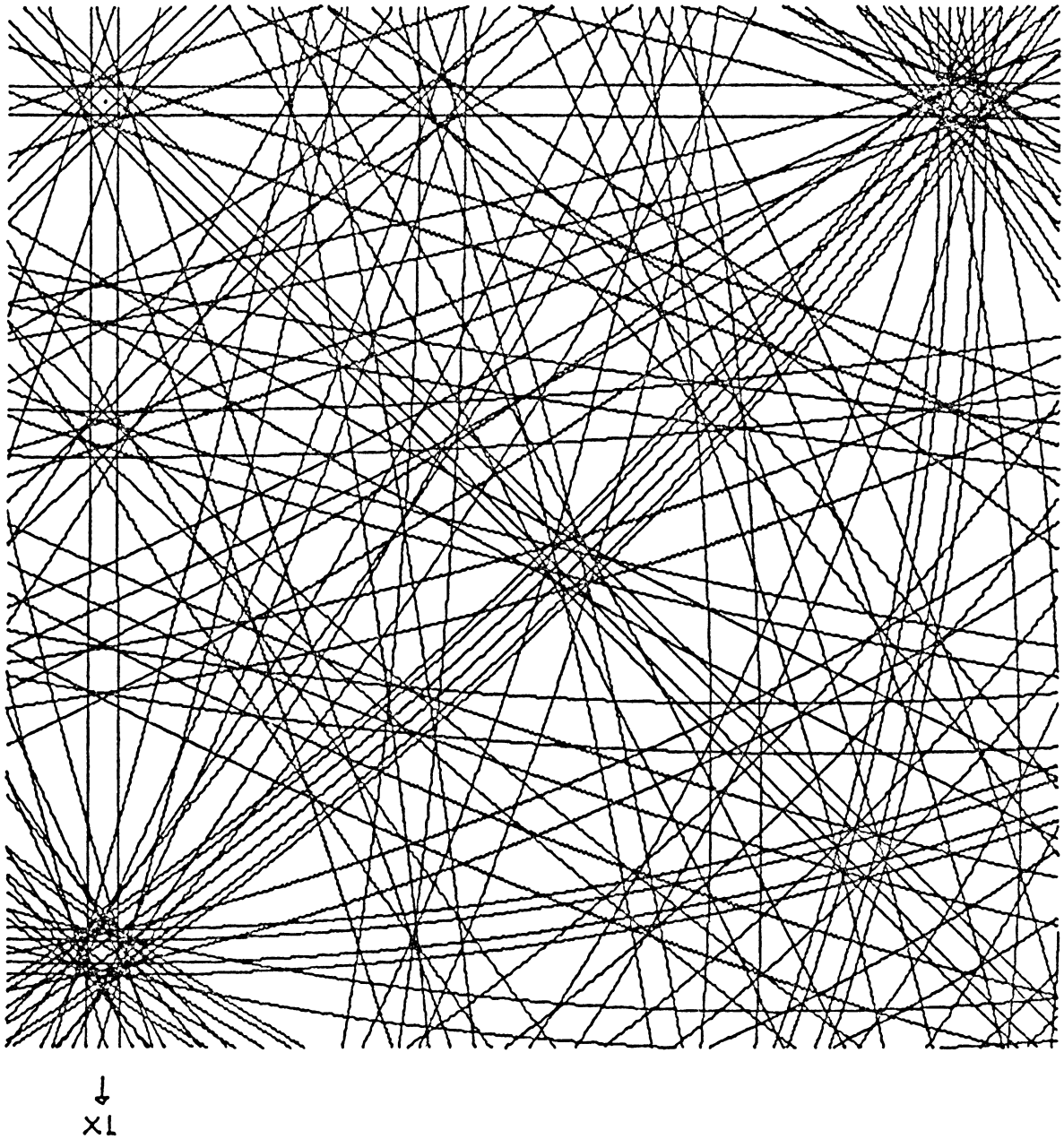

Fig. 47. [001] Kikuchi projection of DIC (Si) crystal at 100KV.
PSR = 15.00 cm, MS = 48, X1 = [100].

In the determination of the boundary normals of general bicrystals in which two Kikuchi patterns are used to formulate the rotation matrix representing the actual specimen tilt, the projection covering the stereographic quadrant is not always enough. The two patterns shown previously in Figure 24(a) and 24(b) are patterns taken before and after specimen tilt. According to Figure 16, there is a 6^{o} clockwise rotation of pattern (b) with respect to pattern (a). Once pattern (a) is indexed, there is only one way to index pattern (b). Here, the projections shown in Figure 35, 36, and 37 become very helpful. From these three projections, both pattern (a) and (b) in Figure 24, with pattern (b) being rotated 6^{o} clockwise with respect to pattern (a), are found to be close to [011]. The [011] K-projection, the same as that shown in Figure 36, and the associated Z-projection are given in Figure 48. Once pattern (a) is indexed and located on the projection, as is indicated by the rectangular block (a) in the Z-projection, there is only one orientation that can be fitted by pattern (b), that is the other rectangular block (b) shown in the Z-projection.

Once the orientation of an observed pattern is located by comparison with projections of smaller PSR, it is advisable to make a second comparison with a projection of larger PSR, e.g., 25 cm or more, in order to make a positive confirmation. In the present study, a set of nine K-projection and Z-projection pairs, each with PSR=25 cm, were produced for cubic crystals. The nine K-projections overlap extensively to cover the whole stereographic quadrant. The orientations, i.e., the directions of X3 axes, are [001], [025], [011], [205], [225], [122], [101], [525], and [111]. The X1 axes are obtained by ($\bar{X}3$ x [100]) x $\bar{X}3$, so that all the

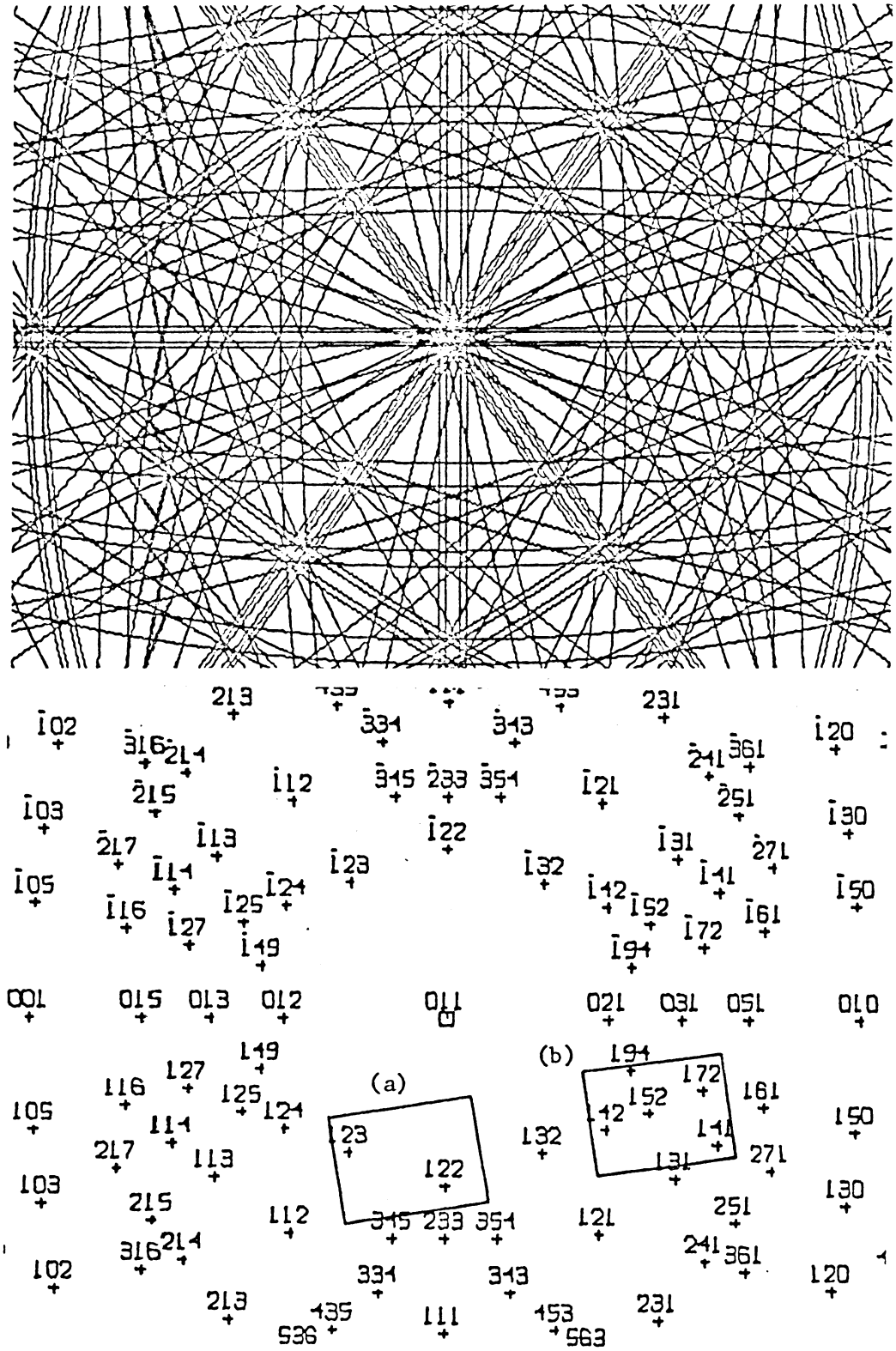

Fig. 48. [011] zone projection and Kikuchi projection of FCC (Al) crystal used to help indexing of Kikuchi patterns shown in Figure 24. PSR = 7.50cm.

nine projections can be matched up together, if desired, without making any relative rotation. The [001], [025], and [011] K-projections shown in Figures 49, 50, and 51 are three examples, each having the origin located at the center of projection.

For the K-projections of larger PSR, i.e., 30 cm or more, the pole indices may be plotted directly on the K-projections without overcrowding. An example for cubic crystals is given in Figure 52, in which each set of directional indices is plotted with the second index located at the center of the indexed pole. With pole indices printed on the K-projection, the K-projection is conveniently used to identify unknown patterns.

For HCP crystals, a set of fourteen K-projection and Z-projection pairs, each with PSR = 25 cm, were generated. The X3 axes for the first seven projections among the fourteen are [0001], $[\bar{1}2\bar{1}6]$, $[\bar{1}2\bar{1}3]$, $[\bar{3}6\bar{3}5]$, $[\bar{1}2\bar{1}1]$, $[\bar{2}4\bar{2}1]$, and $[\bar{1}2\bar{1}0]$. All these projections have a common X1 axis of $[\bar{1}0\bar{1}0]$, and have their origins located at the upper center position of each projection. The X3 and X1 axes of the second seven projection are exactly the same as those of the first seven, except that the origins are all located at the lower center position of each projection. These fourteen K-projections adequately cover an area one sixth of the full stereographic projection defined by [0001]-$[01\bar{1}0]$-$[\bar{1}100]$. With such a set of fourteen projections, detailed comparison with the observed patterns can be made. The $[\bar{1}2\bar{1}6]$ Z-projection and K-projection, each with the origin located at the lower center position indicated by a square symbol with an inner tick mark, are given as examples in Figures 53 and 54.

For cubic crystals, indexing of individual K-lines can be done by taking the cross product of two zone axes which share the K-pair in

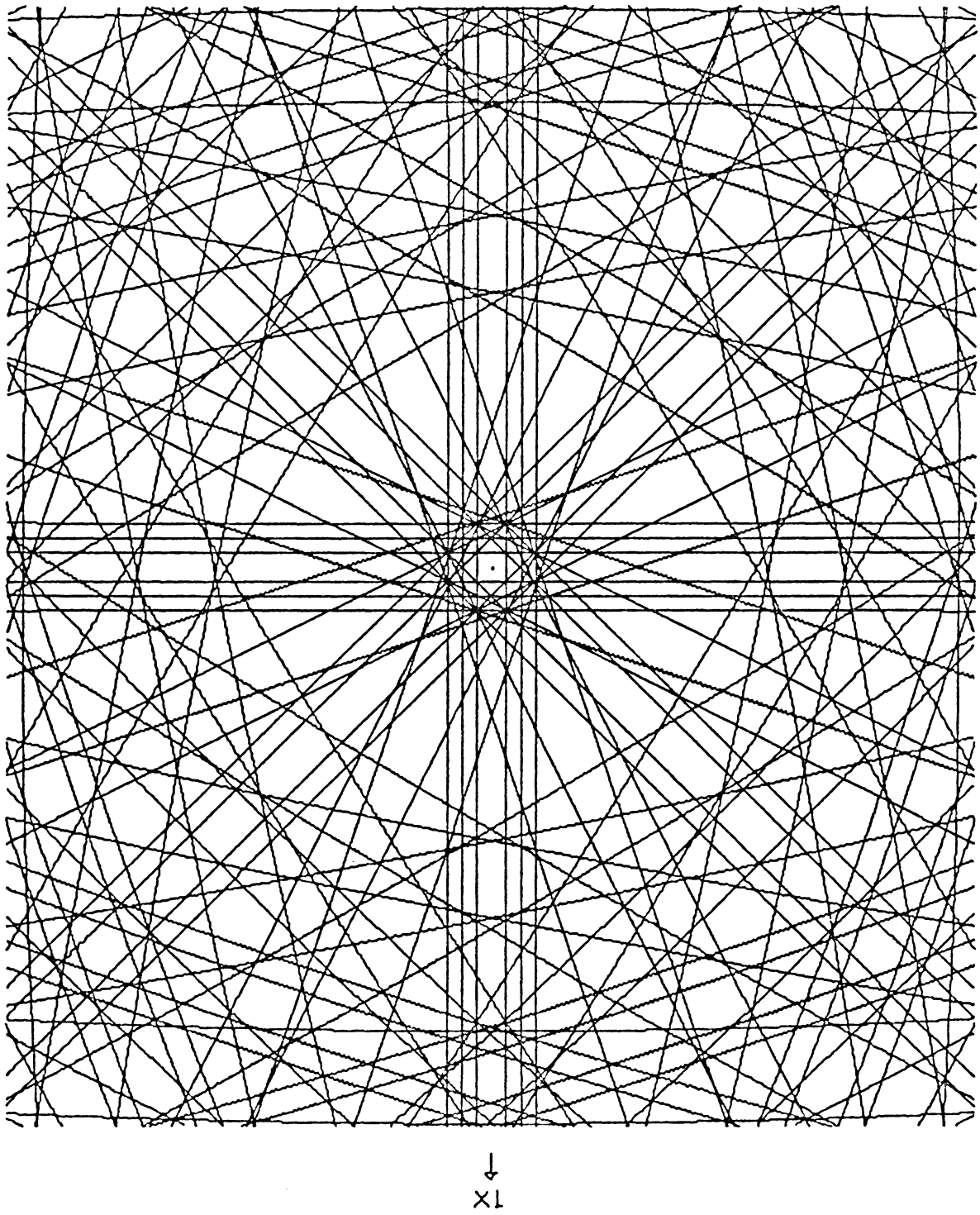

Fig. 49. [001] Kikuchi projection of FCC (Al) crystal at 100KV. PSR = 25.00 cm, MS = 36, X1 = [100].

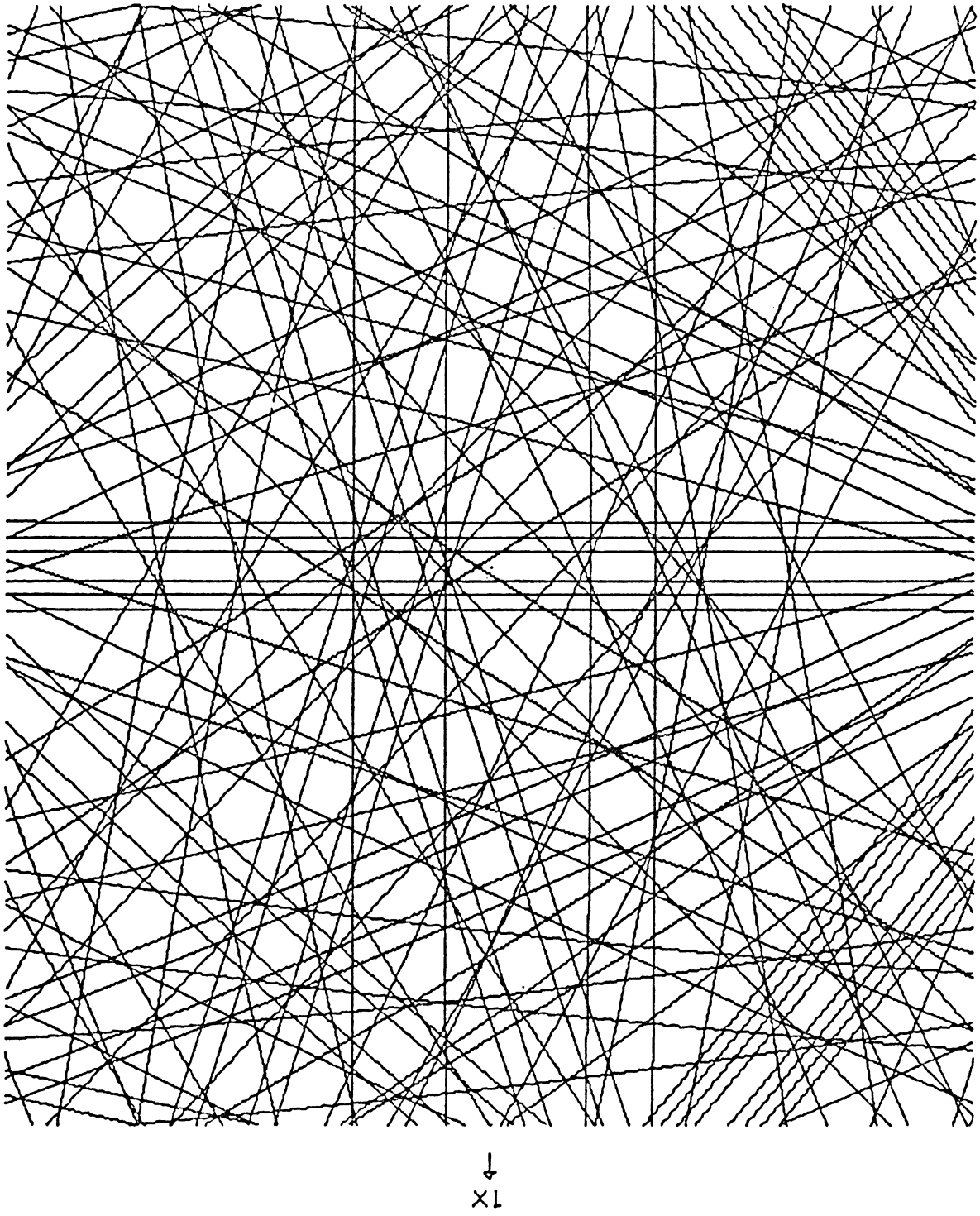

Fig. 50. [025] Kikuchi projection of FCC (A1) crystal at 100KV.
PSR = 25.00 cm, MS = 36, X1 = [100].

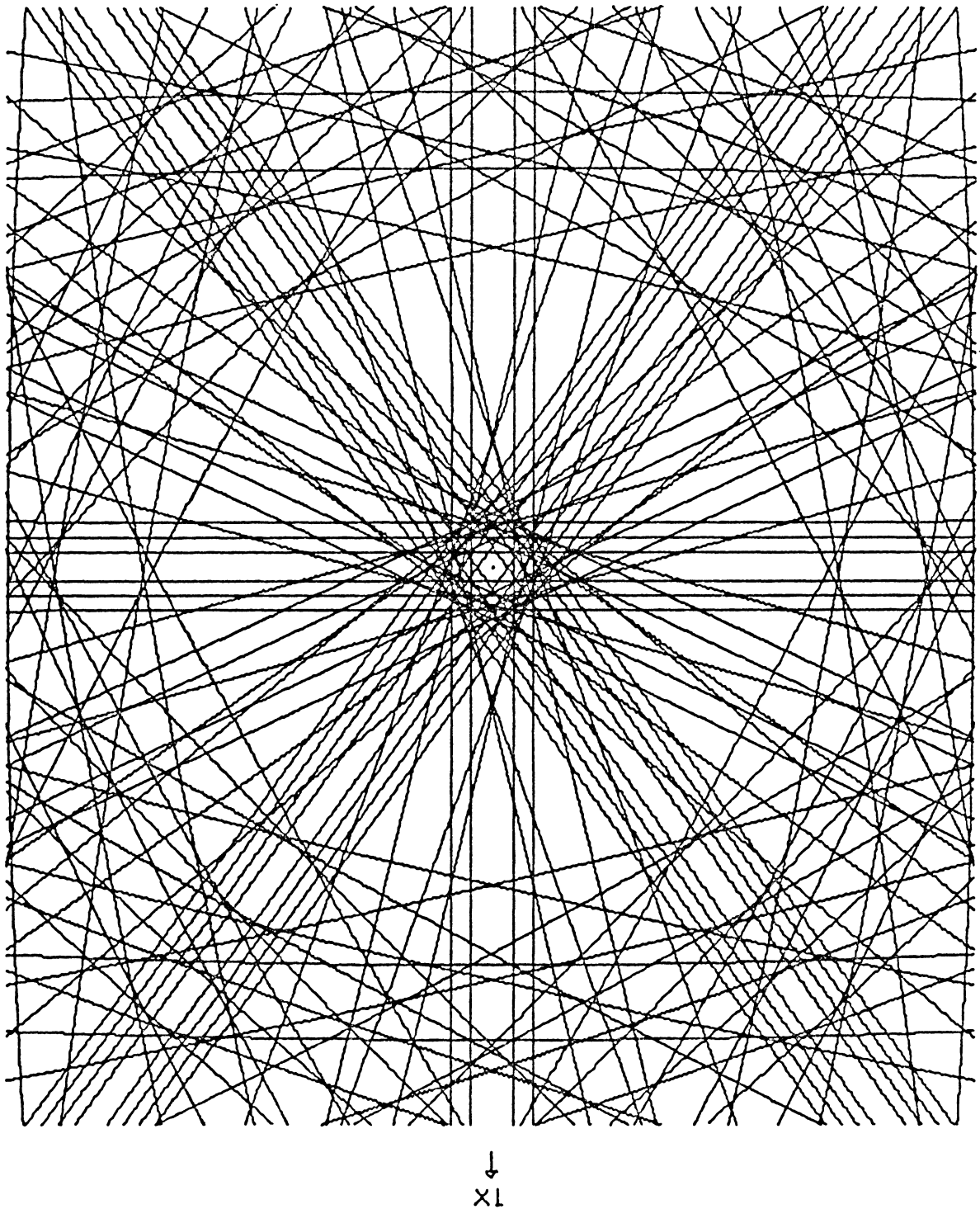

Fig. 51. [011] Kikuchi projection of FCC (Al) crystal at 100KV. PSR = 25.00 cm, MS = 36, X1 = [100].

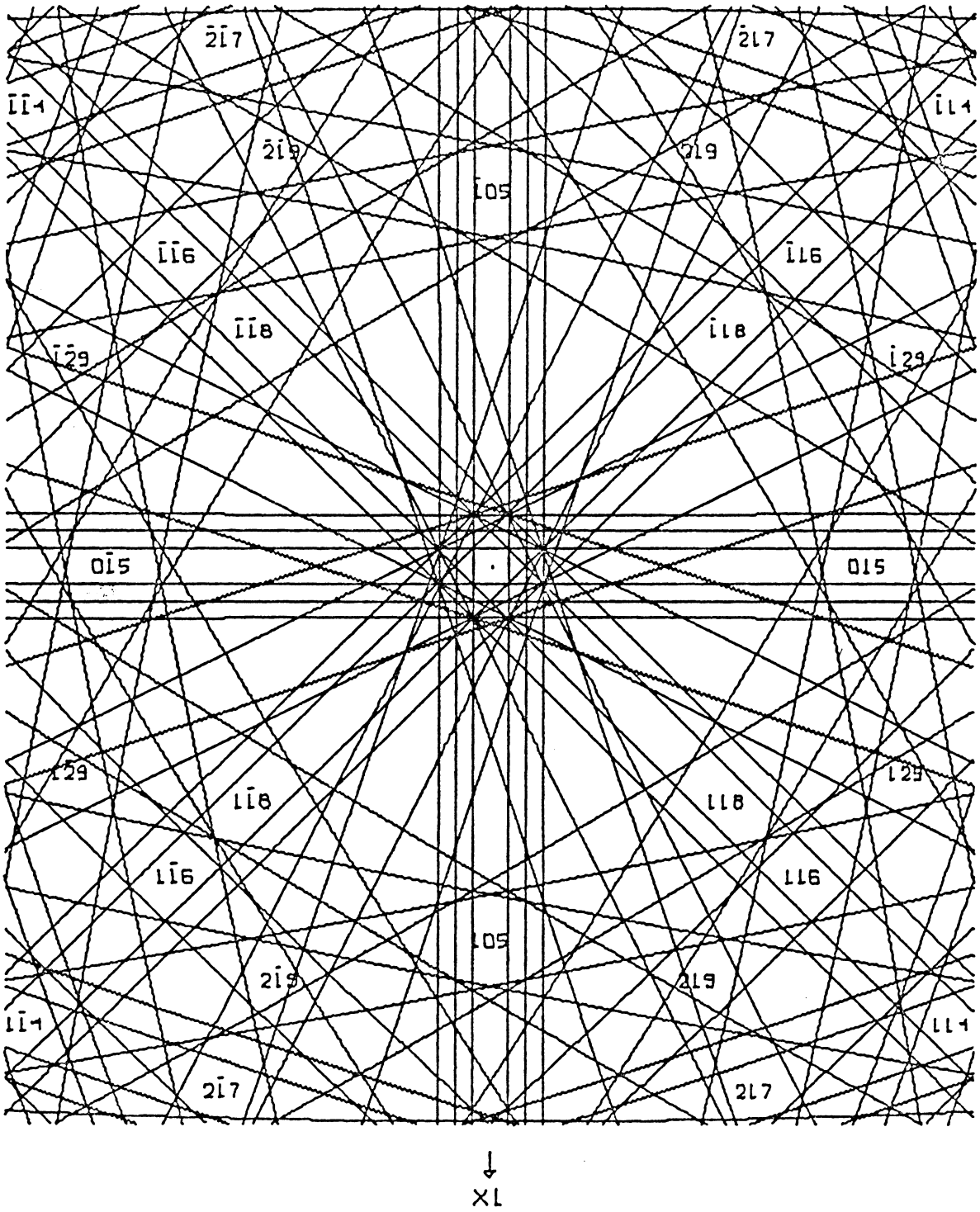

Fig. 52. [001] Kikuchi projection of FCC (Al) crystal at 100KV.
PSR = 30.00 cm, MS = 36, MDZP = 3, X1 = [100].

Fig. 53. [$\bar{1}2\bar{1}6$] zone projection associated with the Kikuchi projection shown in Figure 54.
PSR = 25.00 cm, MDZP = 3, X1 = [$10\bar{1}0$].

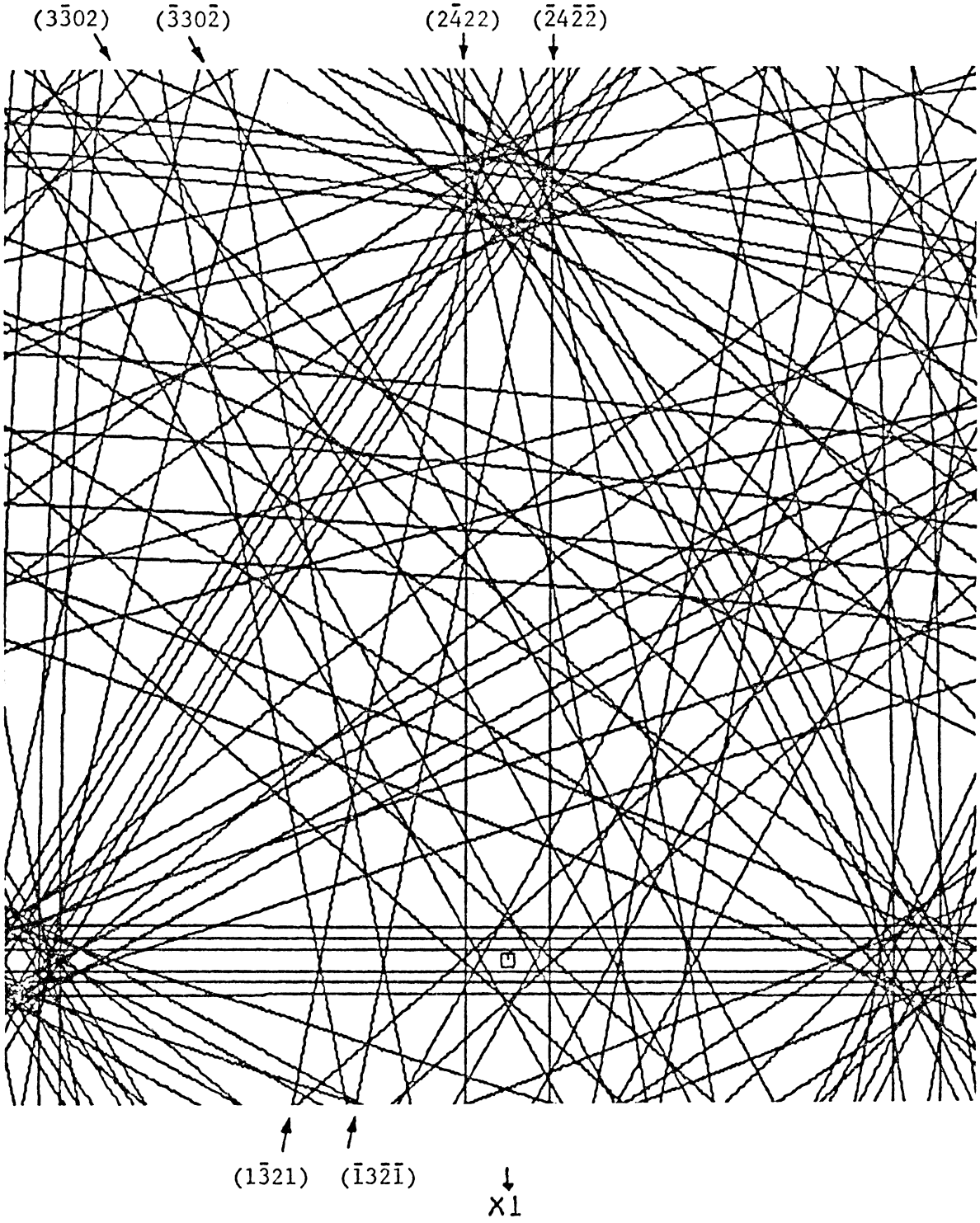

Fig. 54. [$\bar{1}2\bar{1}6$] Kikuchi projection of HCP (Ti) crystal at 100KV. PSR = 25.00 cm, RDL = 1.90, RDU = 2.03, X1 = [10$\bar{1}$0].

question. However, this easy determination is not applicable for non-cubic systems. A computer printout was thus programmed to help in identifying individual K-lines. In this printout, three parameters are listed. They are: (1) the perpendicular distance between the origin and the K-line, (2) the angle measured from the normal of the (hkℓ) K-line (drawn from the origin to the K-line, and designated as XHKL) to the X1 axis, and (3) the distance of K-pair separation. It should be noted that when the angle from XHKL to X1 is measured in the counter-clockwise direction, a negative sign is given to the angle. The printed list associated with the $[\bar{1}2\bar{1}6]$ K-projection shown in Figure 54 is given in Table IV as an example. To demonstrate the application of this table, the K-pair in Figure 54 running parallel to the X1 axis and passing through the origin is considered, and the K-line on the right to the origin is to be indexed. The three parameters associated with this K-line are measured. The distance from origin to this K-line is 0.66 cm, the angle measured from XHKL to X1 axis is 90^{o}, and the distance of K-pair separation is 1.32 cm. From the associated Z-projection, it is found that the K-pair passes through the $[\bar{2}113]$ zone axis. On the table it is seen that there are twelve first-order K-pairs sharing the $[\bar{2}113]$ axis. By comparing the measured and listed parameters, the K-line is readily indexed to be $(\bar{2}4\bar{2}\bar{2})$. The pairing K-line on the left is therefore indexed to be $(2\bar{4}22)$. Okamoto et al. [6] have indexed this K-pair as $\langle\bar{1}2\bar{1}\bar{1}\rangle$, which is an unallowable diffraction pair according to structure factor considerations, and these authors interpreted the appearance of these K-pairs to be a result of double diffraction. Apparently, this is a misinterpretation due to the miscalculation of the d-spacings of the crystallographic

Table IV. Parameters for Indexing of Kikuchi Lines

ZONE AXIS	INDICES OF DIFF. LINE	DISTANCE TO ORIGIN (CM)	ANGLE FROM XHKL TO X1 (DEG) (CW:+,CCW:-)	PAIR SEPARATION (CM)
-5 4 1 6				
	0 2 -2 -1	0.38	61.2	0.75
	1 -2 1 2	6.08	90.0	0.75
	1 0 -1 1	11.87	170.7	0.44
	1 2 -3 0	4.48	-140.4	0.97
	2 -2 0 3	10.03	115.0	0.98
	3 -2 -1 4	11.38	130.9	1.31
-4 2 2 9				
	0 1 -1 0	6.43	-121.2	0.37
	3 -3 0 2	1.46	118.1	1.16
	3 -2 -1 2	4.06	135.3	1.04
	3 -1 -2 2	6.42	155.2	1.06
	3 0 -3 2	7.79	173.8	1.19
-2 1 1 3				
	-2 4 -2 -2	0.66	90.0	1.32
	-1 3 -2 -1	1.92	-100.7	0.98
	0 1 -1 0	6.43	-121.2	0.37
	1 -1 0 1	5.58	116.8	0.42
	1 0 -1 1	11.87	170.7	0.44
	1 2 -3 1	9.51	-143.3	1.02
	2 -3 1 2	1.76	100.1	1.04
	2 -1 -1 2	9.52	142.4	0.77
	2 1 -3 2	11.47	-168.7	1.10
	2 2 -4 2	10.61	-156.2	1.38
	3 -2 -1 3	8.03	133.0	1.16
	3 -1 -2 3	10.37	152.2	1.18
-2 1 1 6				
	-2 2 0 -1	0.38	118.8	0.75
	-2 3 -1 -1	1.92	-79.3	0.98
	0 1 -1 0	6.43	-121.2	0.37
	2 0 -2 1	6.00	175.3	0.76
	2 1 -3 1	6.88	-165.2	1.00
	4 -2 -2 2	2.94	146.6	1.32
-2 2 0 3				
	0 -3 3 2	1.46	61.9	1.16
	1 -2 1 2	6.08	90.0	0.75
	1 1 -2 0	3.46	-151.2	0.63
	2 -1 -1 2	9.52	142.4	0.77
	3 0 -3 2	7.79	173.8	1.19
-2 4 -2 9				
	0 -3 3 2	1.46	61.9	1.16
	1 -3 2 2	1.76	79.9	1.04
	1 0 -1 0	0.18	0.0	0.36
	2 -3 1 2	1.76	100.1	1.04
	3 -3 0 2	1.46	118.1	1.16

Table IV. Parameters for Indexing of Kikuchi Lines (Cont.)

ZONE AXIS	INDICES OF DIFF. LINE	DISTANCE TO ORIGIN (CM)	ANGLE FROM XHKL TO X1 (DEG) (CW:+,CCW:-)	PAIR SEPARATION (CM)
-1 0 1 2				
	-2 2 0 -1	0.38	118.8	0.75
	-1 2 -1 0	7.37	-90.0	0.64
	0 2 -2 1	13.06	-123.9	0.80
	1 0 -1 1	11.87	170.7	0.44
	1 2 -3 2	14.28	-146.5	1.13
	3 -2 -1 2	4.06	135.3	1.04
-1 1 0 2				
	0 2 -2 -1	0.38	61.2	0.75
	1 -3 2 2	1.76	79.9	1.04
	1 -1 0 1	5.58	116.8	0.42
	1 1 -2 0	3.46	-151.2	0.63
	2 0 -2 1	6.00	175.3	0.76
	3 -1 -2 2	6.42	155.2	1.06
-1 2 -1 3				
	-2 -2 4 2	2.94	33.4	1.32
	-2 -1 3 1	1.92	21.6	0.98
	-1 -2 3 2	4.06	44.7	1.04
	0 -1 1 1	5.58	63.2	0.42
	1 -3 2 3	5.80	80.4	1.14
	1 -2 1 2	6.08	90.0	0.75
	1 -1 0 1	5.58	116.8	0.42
	1 0 -1 0	0.18	0.0	0.36
	2 -3 1 3	5.80	99.6	1.14
	3 -2 -1 2	4.06	135.3	1.04
	3 -1 -2 1	1.92	158.4	0.98
	4 -2 -2 2	2.94	146.6	1.32
-1 2 -1 6				
	-3 2 1 -1	0.49	137.8	0.98
	-2 2 0 -1	0.38	118.8	0.75
	-2 4 -2 -2	0.66	90.0	1.32
	0 2 -2 -1	0.38	61.2	0.75
	1 0 -1 0	0.18	0.0	0.36
	1 2 -3 -1	0.49	42.2	0.98
0 0 0 1				
	-3 1 2 0	1.98	-18.3	0.96
	-3 2 1 0	4.48	-39.6	0.97
	-2 1 1 0	3.46	-28.8	0.63
	-2 3 -1 0	7.05	-78.6	0.98
	-1 1 0 0	6.43	-58.8	0.37
	-1 2 -1 0	7.37	-90.0	0.64
	-1 3 -2 0	7.05	-101.4	0.98
	0 1 -1 0	6.43	-121.2	0.37
	1 0 -1 0	0.18	0.0	0.36
	1 1 -2 0	3.46	-151.2	0.63
	1 2 -3 0	4.48	-140.4	0.97
	2 1 -3 0	1.98	-161.7	0.96

planes which produced the K-pair. Other examples selected in Figure 54 are the $(3\bar{3}02)$ and $(\bar{1}32\bar{1})$ lines. With the location parameters measured to be 1.46 cm, 118.1°, and 1.16 cm for the $(3\bar{3}02)$, and 1.92 cm, -100.7°, and 1.16 cm for the $(\bar{1}32\bar{1})$, the indices of these two lines are quickly found in the table. From these examples, it is seen that identification of K-lines can become a routine matter, and tedius calculations are thus eliminated.

In Figures 55 and 56, a pattern taken from Al-0.5at.%Ag and a pattern obtained from α-Ti are compared with the simulated projections. Although on the observed patterns the K-lines appear as black and white pairs, and on the simulated patterns the K-lines can only be drawn as black lines, the correlation between the two can be easily recognized. In certain cases, some differences between the observed and simulated patterns are noticed. For example, on the simulated pattern shown in Figure 56, the $(\bar{3}033)$ K-line does not appear because of structure factor considerations. However, the $(\bar{3}033)$ K-line is clearly seen on the observed pattern. The other examples are the observation of strong {222} forbidden K-pairs from diamond cubic crystals, and the appearance of a narrow bright line along the center of {111} bands[36]. A possible explaination for the appearance of these forbidden Kikuchi lines in the double diffraction phenomena where inelastically scattered electrons are diffracted twice as they pass through the crystal, thus producing a diffracted intensity at a position corresponding to a forbidden Kikuchi line.

Finally, one important point needs to be emphasized. According to Figure 12, the stereographic projection is constructed with the observer viewing in the direction from O to S. Also, in the determination of

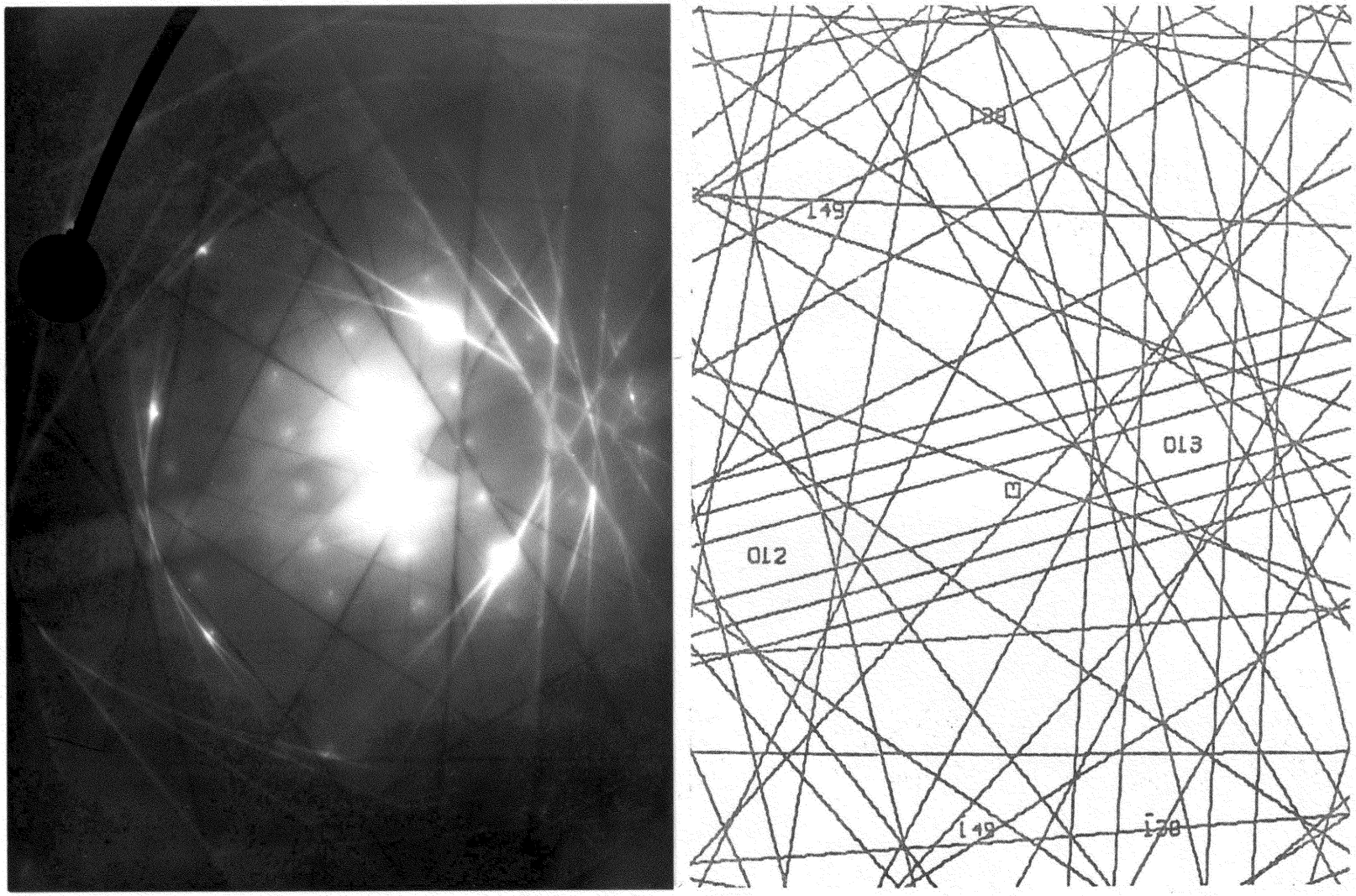

(a) (b)

Fig. 55. (a) Kikuchi pattern of Al-0.5 at .% Ag crystal at 100KV. Effective camera length is 47.0 cm.
(b) [025] simulated pattern of FCC (Al) crystal at 100KV. PSR = 47.00 cm, MS = 52.
MDZP = 3, X1 = [2̄0̄ 5 2̄].

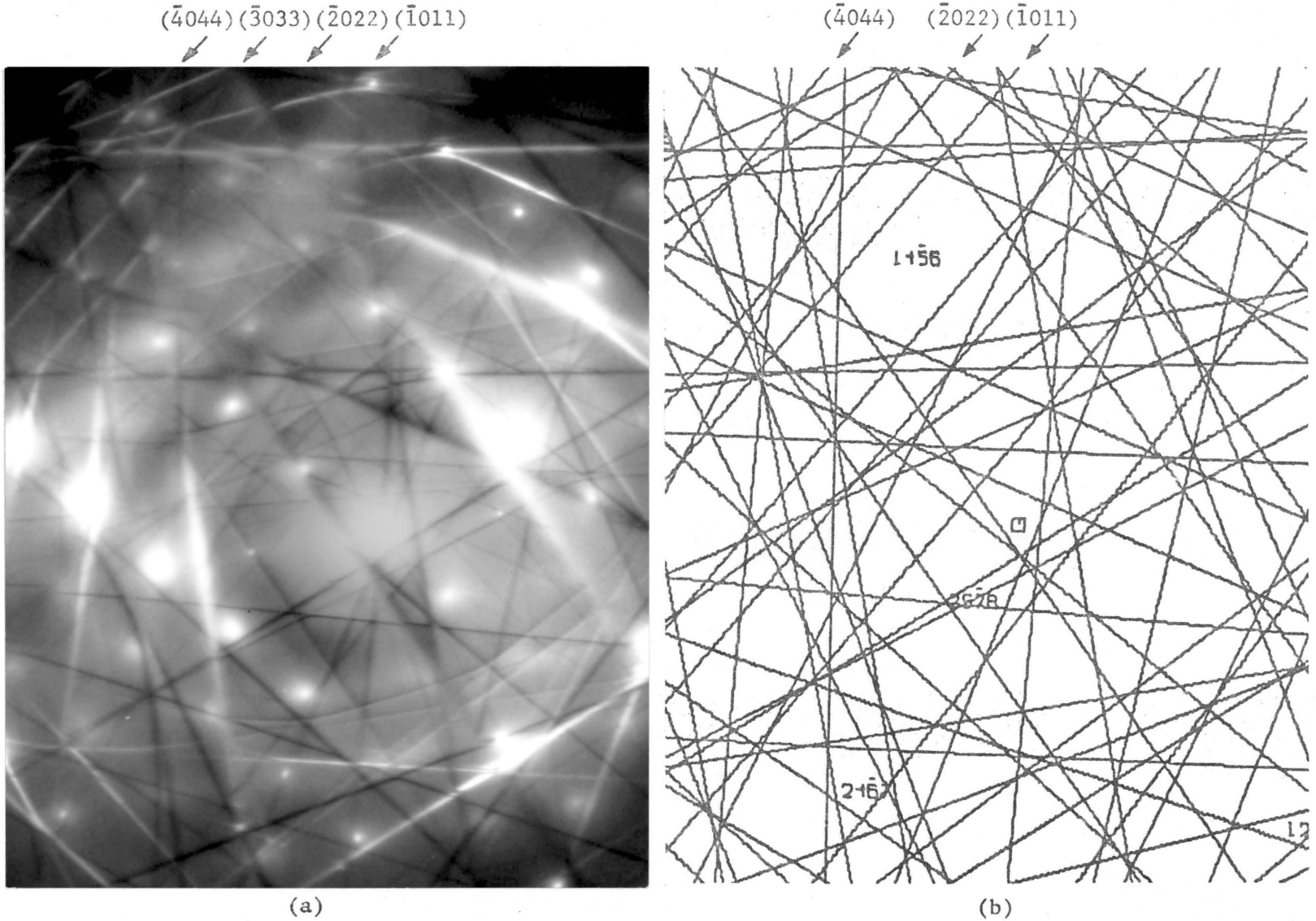

Fig. 56. (a) Kikuchi pattern of α-titanium crystal at 100KV. Effective camera length is 94.0 cm.
(b) [4 11 $\bar{1}\bar{5}$ 17] simulated pattern of HCP (Ti) crystal at 100KV. PSR = 94.00 cm, RDL = 3.36, RDU = 3.70, MDZP = 3, X1 = [7$\bar{5}$20].

bicrystal parameters, the reference frames are selected from the Kikuchi patterns with the Z_R axes pointed out of the papers. Because of these two conventions selected, it is essential, especially in the study of triclinic crystals, to imagine that the Kikuchi patterns were obtained with the specimen and the illuminating source located under the final fluorescent screen. If this is done, no confusion will arise in the physical connection between specimen orientation, Kikuchi patterns, and Kikuchi projections.

VI. CONCLUSIONS

The results of the present study lead to the following conclusions.

A. Using a digital computer program developed in this study, the three bicrystal parameters may be determined accurately from an analysis using matrix algebra and Kikuchi patterns.

   1. For high-angle bicrystals, the angle of misorientation can be obtained to within $\pm 0.5^{\circ}$, and the axis of misorientation to within $\pm 0.2^{\circ}$. Furthermore, the degeneracy misorientation angle-axis pairs can be determined without re-indexing of the Kikuchi patterns.
   2. For low-angle bicrystals, the misfit angle may be calculated to within $\pm 0.1^{\circ}$, and the axis of misfit to within $\pm 4^{\circ}$.
   3. The boundary normals for either high or low-angle bicrystals can be obtained from an analysis which requires a specimen tilt inside the microscope. For those boundaries with relatively large angles of inclination to the projection plane, the boundary normals so determined are generally accurate to $\pm 2^{\circ}$, if a suitable magnification correction is made.

B. For the Siemens Elmiskop 1A electron microscope, the shifting of specimen position along the electron-optical axis as a result of specimen tilt may lead to a variation of $\pm 10\%$ in both magnification and camera length. With the calibration curves obtained in the present study, these errors can be corrected if the positions of the objective controllers are recorded for each exposure.

C. The beam axis of a Kikuchi pattern can be determined from a variety of approaches: 3-pole, 3-normal, 2-pole/1-normal, 1-pole/2-normal, and 1-pole/matrix solutions.

   1. The 3-normal solution is the most accurate one. The inherent accuracy is generally within $\pm 0.05^{o}$, and is nearly independent of errors in the effective camera length L.
   2. For the other approaches in which at least one Kikuchi pole is used to formulate the equations, the accuracy depends on the assumed effective camera length. The beam axis may generally be obtained to within $\pm 0.1^{o}$ when L is calculated from Kikuchi pole separation , and to within $\pm 0.4^{o}$ when L is computed from Kikuchi pair separation.

D. The computer program developed in this study, which combines matrix algebra, digital computation, and the CALCOMP plotter, can be used to generate stereographic Kikuchi maps of any desired orientation and projection sphere radius for FCC, BCC, diamond cubic, and HCP crystals.

E. By computer generation of a set of Kikuchi projections with systematic variations in orientation and projection sphere radius, together with the associated zone projections and printout list for Kikuchi line identification, indexing of observed Kikuchi patterns becomes a matter of visual comparison between the patterns and the projections. Kikuchi pole indices are read from the zone projections. For cubic crystals, indices of individual Kikuchi lines are obtained by taking the cross product between Kikuchi poles. For non-cubic crystals, indices of Kikuchi lines are readily read from the printout list.

F. Through additional studies, the bicrystal analysis developed in the present study may be applied to the measurement of dihedral angles at triple grain junctions, as well as determination of orientation relationships between phases.

F. Future study might also provide an interpretation for the insensitivity of the 3-normal beam axis solution to large variations in the assumed effective camera length.

VII. BIBLIOGRAPHY

1. O. Johari and G. Thomas, The Stereographic Projection and Its Application, Technique of Metals Research, Vol. 11A, Interscience Publisher, 1969, pp. 96-99.

2. F. F. Lange, "Mathematical Charactarization of A General Bicrystal," Acta Met., Vol. 15, Feb. 1967, pp. 311-318.

3. M. von Heimendahl, W. Bell, and G. Thomas, "Application of Kikuchi Line Analyses in Electron Microscopy," J. Appl. Phys., Vol. 35, No. 12, Dec. 1964, pp. 3614-3616.

4. H. M. Otte, J. Dash, and H. F. Schaake, "Electron Microscopy and Diffraction of Thin Films: Interpretation and Correlation of Images and Diffraction Patterns," Phys. Status Solidi, 5, 1964,pp. 527-549.

5. E. Levine, W. L. Bell, and G. Thomas, "Further Application of Kikuchi Diffraction Patterns; Kikuchi Maps," J. Appl. Phys., Vol. 37, No. 5, April 1966, pp. 2141-2148.

6. P. R. Okamoto, E. Levine, and G. Thomas, "Kikuchi Maps for hcp and bcc Crystals," J. Appl. Phys., Vol. 38, No. 1, Jan. 1967, pp. 289-296.

7. J. L. Bomback and L. E. Thomas, "Generation and Applications of Computer-Drawn Kikuchi Maps," to be published in J. Appl. Cryst., (1970-71).

8. M. L. Kronberg and F. H. Wilson, "Secondary Recrystallization in Copper," Trans. Met. Soc. AIME, 185, 1949, pp. 501-514.

9. W. T. Read and W. Shockley, "Dislocation Models of Crystal Grain Boundary," Phys. Rev., 78, 1950, pp. 275-289.

10. D. G. Brandon, B. Ralph, S. Ranganathan, and M. S. Wald, "A Field Ion Microscope Study of Atomic Configuration at Grain Boundaries," Acta Met., Vol. 12, July 1964, pp. 813-821.

11. D. G. Brandon, "The Structure of High-Angle Grain Boundaries," Acta Met., Vol. 14, Nov. 1966, pp. 1479-1484.

12. R. Morgan and B. Ralph, "A Field-Ion Microscope Study of Grain Boundaries in Iron," Acta Met., Vol. 15, Feb. 1967, pp. 341-349.

13. T. Schober and R. W. Balluffi, "Quantitative Observation of Misfit Dislocation Arrays in Low and High Angle Twist Grain Boundaries," Phil. Mag., Vol. 21, No. 169, Jan. 1970, pp. 109-123.

14. P. N. T. Unwin and R. B. Nicholson, "The Nucleation and Initial Stages of Growth of Grain Boundary Precipitates in Al-Zn-Mg and Al-Mg alloys," Acta Met., Vol. 17, Nov. 1969, pp. 1379-1393.

15. R. C. Koo, "A Quantitative Method for the Study of Orientation Relationship between Subgrains by Dark-Field Transmission Electron Microscopy," J. Appl. Phys., Vol. 37, No. 7, June 1966, pp. 2764-2768.

16. S. Kikuchi, Japan J. Phys., 5, 1928, p. 83.

17. R. H. Geiss, "Transmission Electron Channeling Patterns in Silicon," Va. J. Sci., Vol. 21, No. 3, 1970, p. 139.

18. D. G. Coates, "Kikuchi-like Reflection Patterns obtained with the Scanning Electron Microscope," Phil. Mag., 1967, 16, pp. 1179-1184.

19. C. G. Van Essen, E. M. Schulson, and R. H. Donaghay, "Electron Channeling Patterns from Small (10μm) Selected Areas in the Scanning Electron Microscope," Nature, Vol. 225, Feb. 28, 1970, pp. 847-848.

20. J. M. Cowley, "High-Voltage Transmission Scanning Electron Microscopy," J. Appl. Cryst., 3, 1970, pp. 49-59.

21. P. B. Hirsh, A. Howie, R. B. Nicholson, D. W. Pashley, and M. J. Whelan, Electron Microscopy of Thin Crystals, Butterworths, 1965.

22. G. Thomas, "Kikuchi Electron-Diffraction and Dark-Field Technique in Electron-Microscopy Studies of Phase Transformations," Trans. Met. Soc. AIME, Vol. 233, 1965, pp. 1608-1619.

23. W. G. Morris, "Crystal Orientation and Lattice Parameters from Kossel Lines," J. Appl. Phys., Vol. 39, No. 3, Feb. 1968, pp. 1813-1823.

24. P. Gielen, H. Yakowitz, D. Ganow, and R. E. Ogilvie, "Evaluation of Kossel Microdiffraction Procedures: The Cubic Case," J. Appl. Phys., Vol. 36, No. 3, March 1965, pp. 773-782.

25. A. Lutts, "Determination of Lattice Parameters by the Kossel and Divergent X-Ray Beam Techniques," Advances in X-Ray Analysis, Vol. 11, 1967, pp. 345-358.

26. T. Ellis, L. F. Nanni, S. Weissmann, G. E. Padawer, and N. Hosokawa, "Strain and Precision Lattice Parameter Measurement by the X-Ray Divergent Beam Method I," J. Appl. Phys., Vol. 35, 1964, pp. 3364-3373.

27. M. Bevis and N. Swindells, "The Determination of the Orientation of Micro-Crystals Using a Back-Reflection Kossel Technique and an Electron Probe Microanalyzer," Phys. Status Solidi, 20, 1967, pp. 197-212.

28. M. Umeno, H. Kawabe, and Gunji Shinoda, "Lattice Defect Research by Kossel Technique and Deformation Analysis," Advances in X-Ray Analysis, Vol. 9, 1965, pp. 23-34.

29. K. Lonsdale, "Divergent-Beam X-Ray Photography of Crystals," Phil. Trans. Roy. Soc., London, 240, 1947, p. 219.

30. J. Frazer and G. Arrhenius, X-Ray Optics and Microanalysis, Orsay (Paris: Herman), 1966, p. 516.

31. G. H. Olsen and W. A. Jesser, "Computer-Simulated Electron Diffraction Patterns," Mater. Sci. Eng., 5, 1969-70, pp. 135-141.

32. S. Ranganathan, H. B. Lyon, and G. Thomas, "Computer Simulation of Field-Ion Images of Hexagonal Structures and Superlattices," J. Appl. Phys., Vol. 38, No. 13, Dec. 1967, pp. 4957-4965.

33. C. M. Wayman, Introduction to the Crystallography of Martensitic Transformations, Macmillan, New York, 1964.

34. C. T. Young, "The Effect of Prestrain on the Flow Stress Recovery and Related Dislocation Structure of Polycrystalline Aluminum," M.S. Thesis, Virginia Poly. Tech. Inst., 1967, p. 23.

35. M. Rogulic, Ph.D. Thesis, Cambridge Univ., 1964.

36. H. A. Fowler and L. Marton, "Width of Transmission Kikuchi Lines in Silicon and Diamond," J. Appl. Phys., Vol. 36, 1965, pp. 1986-1995.

VIII. APPENDICES

A. Selection Rules and Cutoff Parameters for Line Diffraction Projections

To generate line diffraction projections, the diffraction lines are selected following the selection rules derived from structure factor considerations. The selection rules and the square of the structure factor F^2 for those crystals considered in the present study are summarized in Table A-1. For those crystals with complicated structures for which no simple selection rules can be derived, a set of input data listing the Miller indices of all important allowable reflection planes may be used to substitute for the section of program which provides automatic selection of diffraction planes in the program.

The number of diffraction lines which appear on each projection is limited by a cutoff parameter. For cubic crystals, a maximum S value MS, where $S = h^2 + k^2 + \ell^2$, is used to limit the number of lines. The choice of MS depends on input projection sphere radius PSR. The suggested choice is listed in Table A-2. For HCP crystals, a maximum squared value of reciprocal d-spacing, $RD=1/d^2$, is used as limiting parameter. In fact, two limiting parameters, the upper limit RDU and the lower limit RDL, were used in the present study. For those planes with $h + 2k = 3n \pm 1$, and ℓ = odd, the diffracted intensity, which is proportional to F^2, is considerably less than those of the other two allowable conditions, as is seen in Table A-1. The lower parameter RDL was used to limit the number of diffraction lines of this category, while the upper parameter RDU was used for those lines of the other two conditions. The suggested choice of RDU and RDL are listed in Table A-3 as a function of PSR. If one limiting parameter is preferred, RDU is suggested. Some formulas useful in HCP crystallography are listed in Table A-4.

Table A-1. Summary of Conditions to Produce Various Diffracted Intensities

Bravais Lattice	Diffraction Conditions	F^2
FCC	h, k, and ℓ mixed	0
	h, k, and ℓ unmixed	$16\ f^2$
BCC	$(h + k + \ell)$ odd	0
	$(h + k + \ell)$ even	$16\ f^2$
Diamond Cubic	h, k, and ℓ mixed	0
	$(h + k + \ell)$ an odd multiple of 2	0
	$(h + k + \ell)$ an even multiple of 2	$64\ f^2$
	$(h + k + \ell)$ odd	$32\ f^2$
HCP	$h + 2k = 3n$, ℓ = odd	0
	$h + 2k = 3n$, ℓ = even	$4\ f^2$
	$h + 2k = 3n \pm 1$, ℓ = odd	$3\ f^2$
	$h + 2k = 3n \pm 1$, ℓ = even	$1\ f^2$

Table A-2. Suggested Choice of Maximum S Values For Cubic Crystals

	Projection Sphere Radius (cm)	Maximum S	Number of Pairs*
FCC	PSR < 15	32	182
	15 ≤ PSR < 25	36	260
	25 ≤ PSR < 45	48	340
	45 ≤ PSR < 70	52	412
	70 ≤ PSR	56	460
BCC	PSR < 15	18	176
	15 ≤ PSR < 25	24	248
	25 ≤ PSR < 45	26	320
	45 ≤ PSR < 70	34	428
	70 ≤ PSR	36	460
Diamond Cubic	PSR < 15	35	190
	15 ≤ PSR < 25	48	246
	25 ≤ PSR < 45	51	294
	45 ≤ PSR < 70	56	352
	70 ≤ PSR	59	424

*Total number of line pairs which would appear on a full stereographic projection.

Table A-3. Suggested Choice of RDL and RDU for HCP Crystals

Projection Sphere Radius (cm)	RDL	RDU
PSR < 5	1.10	1.20
5 ≤ PSR < 8	1.20	1.30
8 ≤ PSR < 15	1.30	1.40
15 ≤ PSR < 25	1.60	1.70
25 ≤ PSR < 45	1.90	2.03
45 ≤ PSR < 70	2.50	2.70
70 ≤ PSR < 90	3.00	3.30
90 ≤ PSR	3.30	3.70

Table A-4. Useful Formulas in HCP Crystallography

1. Plane spacing d between (hkiℓ) planes

$$\frac{1}{d^2} = \frac{4}{3}\left(\frac{h^2 + hk + k^2}{a^2}\right) + \frac{\ell^2}{c^2}$$

2. Conversion between three axis direction [UVW] and four axis direction [uvtw]

$$U = u - t, \qquad V = v - t, \qquad W = w$$

$$u = (1/3)\,(2U-V), \quad v = (1/3)\,(2V-U), \quad w = W, \quad t = -(u+v)$$

3. Indices of the direction [uvtw] normal to plane (hkiℓ)

$$[u,v,t,w] = [h,k,i,(3/2)(a/c)^2\ell]$$

4. Criteria for direction [uvtw] to lie in plane (hkiℓ)
Also can be used to solve for line or intersection of planes.

$$2uh + uk + 2vk + vh + w\ell = 0$$

5. Angle between direction $[u_1v_1\cdot w_1]$ and $[u_2v_2\cdot w_2]$

$$\text{Cos } \theta = \frac{u_1u_2 + v_1v_2 + \frac{1}{2}(u_1v_2 + u_2v_1) + \frac{1}{3}(w_1w_2)\,(\frac{c}{a})^2}{(u_1^2+v_1^2+u_1v_1+\frac{1}{3}w_1(\frac{c}{a})^2)^{\frac{1}{2}}\,(u_2^2+v_2^2+u_2v_2+\frac{1}{3}w_2^2(\frac{c}{a})^2)^{\frac{1}{2}}}$$

6. Angle between planes $(h_1k_1\cdot\ell_1)$ and $(h_2k_2\cdot\ell_2)$

$$\text{Cos } \theta = \frac{h_1h_2 + k_1k_2 + \frac{1}{2}(h_1k_2 + h_2k_1) + \frac{3}{4}\ell_1\ell_2\,(\frac{c}{a})^2}{(h_1^2+k_1^2+h_1k_1+\frac{3}{4}\ell_1^2\,(\frac{c}{a})^2)^{\frac{1}{2}}\,(h_2^2+k_2^2+h_2k_2+\frac{3}{4}\ell_2^2(\frac{c}{a})^2)^{\frac{1}{2}}}$$

7. Length of vector [uv·w]

$$|[uv\cdot w]| = [\,3a^2\,(u^2 + v^2 + uv) + c^2w^2\,]^{\frac{1}{2}}$$

B. Angular Divergency of Various Beam Axis Solutions

Results for the angular divergency of the various beam axis solutions described in Section V-B are listed in the following tables. The solution obtained from the input poles, axes, or normals listed in the first row in each table is assumed to be the most accurate solution for each given effective camera length L, and is also assumed to be the most accurate solution if an effective camera length of 78.85 cm is used. For each method of beam axis calculation, all the resulting solutions were compared with the most accurate solution using L=78.85 cm. The angular divergencies are listed in the following Tables B-1 through B-4, each table corresponding to a different method of solution.

Table B-1 Angular Divergency of Beam Axis Obtained From 3-Pole Solution (Fig. 18)

Solution Input	Angular Deviation (Degrees)								
	Assumed Effective Camera Length (cm)								
Poles	75	76	77	78	79	80	81	82	83
[214][529][316]	0.1743	0.1265	0.0805	0.0365	0.0063	0.0473	0.0868	0.1248	0.1615
[529][326][316]	0.3452	0.2662	0.1907	0.1192	0.0558	0.0436	0.0976	0.1583	0.2182
[326][316][315]	0.1097	0.0989	0.0895	0.0816	0.0756	0.0715	0.0694	0.0693	0.0711
[214][417][213]	0.3769	0.2746	0.1768	0.0848	0.0335	0.1054	0.1883	0.2694	0.3479
[327][417][213]	0.1557	0.1217	0.0891	0.0578	0.0282	0.0090	0.0317	0.0583	0.0843
[326][215][315]	0.1089	0.1050	0.1076	0.1162	0.1292	0.1449	0.1620	0.1800	0.1982
[214][315][213]	0.3469	0.2609	0.1798	0.1064	0.0593	0.0867	0.1485	0.2145	0.2799
[326][327][417]	0.0912	0.1018	0.1126	0.1234	0.1341	0.1446	0.1549	0.1650	0.1748
[529][326][215]	0.2313	0.1777	0.1365	0.1171	0.1263	0.1568	0.1972	0.2414	0.2866
[529][327][215]	0.1521	0.1022	0.0724	0.0820	0.1189	0.1638	0.2103	0.2566	0.3018
Average Deviation	0.2093	0.1636	0.1235	0.0925	0.0767	0.0974	0.1347	0.1738	0.2124

Table B-2 Angular Divergency of Beam Axes Obtained From 3-Normal Solution (Fig. 18)

Solution Input	Angular Deviation (Degrees)								
	Assumed Effective Camera Length (cm)								
Normals	75	76	77	78	79	80	81	82	83
$[\bar{3}31][40\bar{2}][24\bar{2}]$	0.0	0.0	0.0	0.0	0.0	0.0	0.0	0.0	0.0
$[13\bar{1}][40\bar{2}][2\bar{4}0]$	0.0078	0.0079	0.0079	0.0080	0.0080	0.0081	0.0081	0.0082	0.0082
$[0\bar{6}2][40\bar{2}][\bar{3}31]$	0.0212	0.0213	0.0215	0.0216	0.0217	0.0219	0.0220	0.0221	0.0222
$[24\bar{2}][\bar{2}60][40\bar{2}]$	0.0064	0.0063	0.0063	0.0063	0.0062	0.0062	0.0062	0.0062	0.0061
$[24\bar{2}][1\bar{5}1][\bar{4}22]$	0.0682	0.0682	0.0681	0.0680	0.0680	0.0679	0.0679	0.0678	0.0678
$[53\bar{3}][1\bar{5}1][\bar{3}31]$	0.0228	0.0229	0.0229	0.0229	0.0229	0.0229	0.0229	0.0230	0.0230
$[\bar{4}22][13\bar{1}][2\bar{4}0]$	0.0802	0.0802	0.0802	0.0801	0.0801	0.0801	0.0801	0.0801	0.0801
$[5\bar{1}3][13\bar{1}][2\bar{4}0]$	0.0089	0.0090	0.0090	0.0091	0.0091	0.0092	0.0092	0.0093	0.0093
$[3\bar{1}\bar{1}][53\bar{3}][13\bar{1}]$	0.0657	0.0656	0.0656	0.0656	0.0656	0.0655	0.0655	0.0655	0.0654
$[\bar{2}60][13\bar{1}][\bar{4}22]$	0.0807	0.0807	0.0807	0.0807	0.0807	0.0808	0.0808	0.0808	0.0808
$[5\bar{1}3][13\bar{1}][\bar{3}31]$	0.0143	0.0144	0.0145	0.0146	0.0146	0.0147	0.0148	0.0148	0.0149
$[1\bar{5}1][\bar{4}22][53\bar{3}]$	0.0617	0.0616	0.0615	0.0615	0.0614	0.0614	0.0614	0.0613	0.0613
Average Deviation	0.0365	0.0365	0.0365	0.0365	0.0365	0.0366	0.0366	0.0366	0.0366

Table B-3 Angular Divergency of Beam Axes Obtained From 1-Pole/2-Normal Solution (Fig. 18)

Solution Input		Angular Deviation (Degrees)								
		Assumed Effective Camera Length (cm)								
Poles	Normals	75	76	77	78	79	80	81	82	83
[214]	[40$\bar{2}$][2$\bar{4}$0]	0.0576	0.0421	0.0270	0.0122	0.0021	0.0161	0.0298	0.0431	0.0561
[529]	[$\bar{3}$31][24$\bar{2}$]	0.0955	0.0706	0.0462	0.0226	0.0	0.0230	0.0450	0.0664	0.0873
[529]	[5$\bar{1}$3][$\bar{1}$7$\bar{1}$]	0.1028	0.0778	0.0535	0.0302	0.0096	0.0182	0.0393	0.0606	0.0815
[316]	[13$\bar{1}$][$\bar{3}$31]	0.2216	0.1702	0.1201	0.0716	0.0261	0.0271	0.0704	0.1143	0.1573
[316]	[13$\bar{1}$][40$\bar{2}$]	0.2248	0.1732	0.1231	0.0743	0.0275	0.0225	0.0666	0.1107	0.1539
[315]	[$\bar{4}$22][24$\bar{2}$]	0.1200	0.0651	0.0118	0.0405	0.0913	0.1408	0.1891	0.2362	0.2822
[417]	[13$\bar{1}$][$\bar{4}$22]	0.2508	0.1817	0.1208	0.0820	0.0931	0.1404	0.1978	0.2576	0.3175
[417]	[$\bar{3}$51][5$\bar{1}$3]	0.2464	0.1723	0.1002	0.0305	0.0401	0.1065	0.1717	0.2354	0.2976
[215]	[$\bar{3}$1$\bar{1}$][13$\bar{1}$]	0.2786	0.2010	0.1288	0.0721	0.0729	0.1269	0.1917	0.2580	0.3238
[215]	[42$\bar{2}$][2$\bar{4}$0]	0.2344	0.1549	0.0776	0.0097	0.0730	0.1446	0.2146	0.2830	0.3497
[327]	[3$\bar{1}$1][15$\bar{1}$]	0.2231	0.1592	0.1028	0.0687	0.0846	0.1314	0.1857	0.2414	0.2970
[326]	[3$\bar{1}$1][0$\bar{6}$2]	0.3095	0.2311	0.1589	0.1012	0.0862	0.1262	0.1869	0.2523	0.3184
[213]	[$\bar{4}$22][0$\bar{6}$2]	0.3395	0.2489	0.1653	0.0996	0.0921	0.1478	0.2212	0.2979	0.3746
Average Deviation		0.2080	0.1499	0.0951	0.0550	0.0537	0.0901	0.1392	0.1890	0.2382

Table B-4 Angular Divergency of Beam Axes Obtained From 1-Pole/Matrix Solution (Fig. 18)

Solution Input		Angular Deviation (Degrees)								
		Assumed Effective Camera Length (cm)								
X_3-Pole	X_1-Pole	75	76	77	78	79	80	81	82	83
[214]	[40$\bar{2}$]	0.0532	0.0377	0.0227	0.0080	0.0064	0.0203	0.0339	0.0472	0.0602
[326]	[40$\bar{2}$]	0.2964	0.2337	0.1739	0.1188	0.0753	0.0657	0.0978	0.1447	0.1949
[316]	[40$\bar{2}$]	0.2254	0.1739	0.1238	0.0751	0.0287	0.0230	0.0665	0.1104	0.1535
[214]	[2$\bar{4}$0]	0.0688	0.0575	0.0487	0.0435	0.0430	0.0469	0.0540	0.0630	0.0731
[215]	[2$\bar{4}$0]	0.2278	0.1518	0.0841	0.0550	0.1002	0.1652	0.2324	0.2992	0.3650
[213]	[2$\bar{4}$0]	0.3332	0.2397	0.1488	0.0618	0.0353	0.1152	0.1971	0.2775	0.3560
[315]	[$\bar{4}$22]	0.1599	0.1083	0.0642	0.0479	0.0763	0.1196	0.1654	0.2113	0.2567
[417]	[$\bar{4}$22]	0.2920	0.2260	0.1686	0.1283	0.1199	0.1466	0.1926	0.2462	0.3024
[327]	[1$\bar{5}$1]	0.2262	0.1577	0.0910	0.0263	0.0380	0.0996	0.1599	0.2187	0.2762
[213]	[1$\bar{5}$1]	0.3300	0.2364	0.1453	0.0569	0.0327	0.1160	0.1984	0.2789	0.3576
[529]	[$\bar{3}$31]	0.0936	0.0696	0.0470	0.0280	0.0215	0.0343	0.0533	0.0734	0.0936
[316]	[$\bar{3}$31]	0.2248	0.1732	0.1230	0.0740	0.0265	0.0208	0.0659	0.1102	0.1534
Average Deviation		0.2110	0.1555	0.1034	0.0603	0.0503	0.0811	0.1264	0.1734	0.2202

The vita has been removed from the scanned document

COMPUTER GENERATION OF KIKUCHI PROJECTIONS AND CHARACTERIZATION OF GENERAL BICRYSTALS

by

Ching Tsiun Young

ABSTRACT

Three parameters, i.e., misorientation angle, misorientation axis, and boundary normal, have been used to describe a general bicrystal, such as two adjacent grains, subgrains, twins, or two neighboring phases. A computer program has been developed to determine these three parameters. The angle and axis of misorientation are calculated from a misorientation matrix which is obtained by using two Kikuchi patterns, one taken from each of the two crystals. To obtain the boundary normal, a specimen tilt inside the microscope is required. A rotation matrix specifying the actual specimen tilt is formulated from two Kikuchi patterns taken from the same crystal before and after tilt. With this rotation matrix and the change of projected boundary images before and after tilt, the boundary normal can be calculated. It has been demonstrated that for high-angle bicrystal the misorientation may be determined to within $\pm 0.5^{\circ}$, and misorientation axis to within $\pm 0.2^{\circ}$. For low-angle bicrystals, the misfit angle can be obtained to within $\pm 0.1^{\circ}$, and the axis of misfit to within $\pm 4^{\circ}$. The boundary normals so determined are generally accurate to $\pm 2^{\circ}$ if suitable correction is made for magnification changes during crystal tilt.

Variations in magnification and camera length due to the shifting of specimen position along the electron-optical axis were investigated. It was found that a variation of 20% in both magnification and camera length may result when a tilting stage is used. A calibration curve was

obtained which allows for correction of these errors in the Siemens Elmiskop 1A.

The inherent accuracy of various beam axis solutions from a Kikuchi pattern, i.e., 3-pole, 3-normal, 2-pole/1-normal, 1-pole/2-normal, and 1-pole/matrix solutions, was also analyzed. The results indicated that the 3-normal solution is the most accurate one. The beam axis thus determined is accurate to $\pm 0.05^{o}$, and is nearly independent of the effective camera length. For solutions in which at least one Kikuchi pole is used to formulate the equations, the beam axis may be obtained to $\pm 0.1^{o}$, if the effective camera length is calculated from the Kikuchi pole separation.

In order to eliminate the tedius calculations required to index Kikuchi patterns, computer programs were developed to provide for computer plotting of standard stereographic Kikuchi projections of any desired orientation and projection sphere radius for FCC, BCC, diamond cubic, and HCP crystals. The programs also provide for identification of Kikuchi poles as well as identification of individual Kikuchi lines. Indexing of observed patterns becomes a matter of comparison between the patterns and the projections. Coates projections for scanning electron microscopy and transmitted Kossel or pseudo-Kossel projections for x-ray diffraction studies can also be generated simply by changing the input wave length.